NOTE TO USERS

UNIVERSITY OF CALIFORNIA

Los Angeles

FEEDBACK CONTROL OF INCOMPRESSIBLE FLUID FLOWS

A dissertation submitted in partial satisfaction of the requirements for the degree Doctor of Philosophy in Chemical Engineering

by

Prasenjit Ray

2004

The dissertation of Prasenjit Ray is approved.

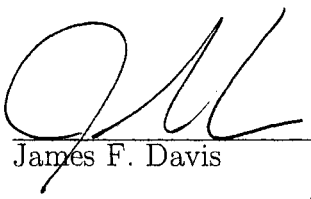

James F. Davis

Gerassimos Orkoulas

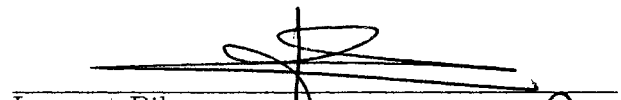

Laurent Pilon

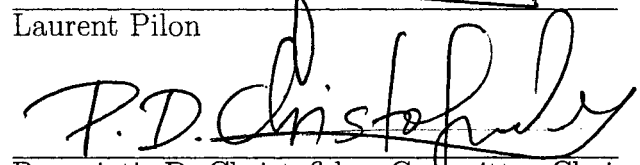

Panagiotis D. Christofides, Committee Chair

University of California, Los Angeles

2004

Contents

List of Figures

List of Tables

Acknowledgements

I am grateful to my advisor, Professor Panagiotis Christofides, for his support and guidance during the course of this work.

I would like to thank Professor James Davis, Professor Gerassimos Orkoulas, and Professor Laurent Pilon for agreeing to participate in my examination committee.

I would also like to thank Dr. James Myatt, Dr. R. Chris Camphouse, and Dr. Siva Banda for their support and guidance on this study.

I am grateful for the continual love, encouragement, and support of my family and Julie Glaser.

I would also like to thank Reginald, Clementine, Fiona, Beatrice, Raffle, Ernest, and Billy.

Vita

1995	Bachelor of Science, Chemical Engineering
	The Ohio State University, Columbus, OH
1995 - 2000	Researcher
	Aerosol Science and Technology Assessment
	Battelle Memorial Institute, Columbus, OH
2000 - pres.	Ph.D student, Chemical Engineering
	University of California, Los Angeles, CA
2003	Master of Science, Chemical Engineering
	University of California, Los Angeles, CA

Publications and Presentations

1. Ray, P. and P. D. Christofides, "Control of Flow Over a Cylinder Using Rotational Oscillations," Computers & Chemical Engineering, accepted.

2. Ray, P. and P. D. Christofides, "Control of Flow Over a Circular Cylinder Using Rotational Oscillations," *American Institute of Chemical Engineering Annual Meeting, paper 442e*, San Francisco, California, 2003.

ABSTRACT OF THE DISSERTATION

Feedback Control of Incompressible Fluid Flows

by

Prasenjit Ray
Doctor of Philosophy in Chemical Engineering
University of California, Los Angeles, 2004

Professor Panagiotis D. Christofides, Chair

The problem of trying to influence a flow field to behave in a desirable way has received significant attention in the past. This problem has been motivated by many practical engineering applications including reduction of the drag which is generated by a turbulent flow passing on a surface by preventing the transition from laminar to turbulent flow inside the boundary layer through active feedback control. According to some estimates, keeping the flow over the surface of a vehicle laminar could yield up to 30% reduction in fuel consumption. Flow control is studied for flow of vital fluids in a pipeline, nanoflows inside the human body, and for better understanding of mineral deposition. Nanoflows are present in pulsatile devices, which have been used as a bridge to heart transplantation. On a larger scale, hydraulic manipulators are a candidate for fusion reactor maintenance. Other applications of flow control include suppression of fluid mechanical instabilities in coating processes and suppression of waves exhibited by falling liquid films. In general, fluid flow control can be classified in two categories: passive and active. Passive control typically involves some kind

of design modification of the surface (e.g., wall-mounted, stream-wise ribs or riblets) and requires no auxiliary power while active control involves continuous adjustment of a variable that affects the flow based on measurements of quantities of the flow field (feedback). Active methods for fluid flow control have included injection of polymers, mass transport through porous walls (e.g., blowing/suction), application of electro-magnetic forcing, and active rotational oscillation of bluff bodies.

Flow past a circular cylinder is a classic fluid dynamics problem. Control of flow past a circular cylinder is studied for a number of practical reasons. Wake modification, reduction of flow-induced vibrations, design of heat exchangers, and improvement of chemical mixing are among the diverse applications involving flow past a circular cylinder. This problem is also studied for stall control and lift enhancement as well as for design of aerodynamic vehicles. The drag force on the cylinder may be reduced by active control in the form of rotational oscillation.

In this dissertation, we focus on two-dimensional, incompressible viscous channel flow over an infinitely long cylinder and examine the effect of controlled rotational cylinder oscillation in reducing the drag exerted on the cylinder. Drag reduction on this system is of particular interest to the United States Air Force, which seeks to reduce fuel consumption of missiles. The system of flow past a circular cylinder emulates a missile falling at a high angle of attack. Initially, a description of the flow field and of the governing equations is given together with a precise specification of the drag exerted on the cylinder. Then, the solution of the flow field for the stationary cylinder is given and the drag on the cylinder is validated against available numerical studies. The effect of controlled cylinder oscillation in reducing the drag exerted on the cylinder is subsequently examined. Based on the study of the open-loop dynamics of this fluid dynamic system and an analysis of the open-loop simulations, a control

system is designed that automatically determines the frequency of cylinder oscillation, based on the Reynolds number, to consistently reduce the drag exerted on the cylinder for Reynolds numbers in the range 100-500.

Flow over a flat plate is another well-studied problem, particularly from the standpoint of boundary layer control. This problem emulates, among other systems, flow over a wing. Reduction of drag on a wing is of particular interest to the United States Air Force, which is interested in reducing fuel consumption for aircraft. This dissertation examines the reduction of frictional drag exerted on a flat plate using active feedback control. Several alternative control configurations, including both pointwise and spatially uniform control actuation and sensing, are developed and tested through computer simulations. All control configurations use control actuation in the form of blowing/suction on the plate and measurements of shear stresses along the plate. The simulation results indicate that the use of active feedback control, which employs reasonable control effort, can significantly reduce the frictional drag exerted on the plate compared to the open-loop values.

A better insight into the system of flow past the circular cylinder is gained as a result of the stationary cylinder simulations. This is insight is furthered by open-loop simulation and the design of an effective closed-loop, active controller. Finally, the reduced-order model of the flow past the circular cylinder sets up a tool for developing model-based feedback control of this system. A methodology for open-loop and closed-loop control with this reduced-order model is suggested. The open-loop dynamics of flow past the flat plate are studied, and an effective active feedback controller is designed, implemented, and evaluated.

Funding from the Air Force Office of Scientific Research and Wright-Patterson Air Force Base is gratefully acknowledged.

Chapter 1

Introduction

1.1 Overview

In this chapter, a general motivation for and background on flow control is given. Following this, a description of work done on flow past a circular system and applications of Proper Orthogonal Decomposition (POD) to flow control problems are given. Finally, the objectives and structure of this thesis are stated.

1.2 Background on flow control

The problem of trying to influence a flow field to behave in a desirable way has received significant attention in the past (see, for example, [22, 48–50] for results in this area and reference lists). This problem has been motivated by many practical engineering applications including reduction of the drag which is generated by a turbulent flow passing on a surface by preventing the transition from laminar to turbulent flow inside the boundary layer through active feedback control. In general, fluid flow control can be classified in two categories: passive and active. Passive control typically involves some kind of design modification of the surface (e.g., wall-mounted, stream-wise ribs

or riblets) and requires no auxiliary power (see, for example, [32, 111] for results on passive control), while active control involves continuous adjustment of a variable that affects the flow based on measurements of quantities of the flow field (feedback). Active methods for fluid flow control have included injection of polymers [80, 110], mass transport through porous walls (e.g., blowing/suction) [6,25,27,38], application of electro-magnetic forcing [5,36,103], and active rotational oscillation of bluff bodies [78,89,96,105,109].

The development of an efficient control system for a fluid flow should be based on the specific Navier-Stokes equations that describe the flow in order to exploit their ability to accurately predict the spatiotemporal behavior of the flow field. The main obstacle in following this approach for fluid flow control system design is the infinite-dimensional nature of the Navier-Stokes equations, which prohibits their direct use for the synthesis of practically implementable (low-order) feedback controllers. These controller synthesis and implementation problems, together with the need to develop computationally efficient numerical solution algorithms for the Navier-Stokes equations, have motivated significant research on the understanding of the dynamic behavior of various formulations of the Navier-Stokes equations and the derivation of low-order ODE systems that accurately reproduce their long term dynamics and solutions. The dissipative nature of the Navier-Stokes equations has motivated an extensive research activity on the dynamics where important contributions include the realization that turbulent flows involve coherent structures (e.g., [7,23,56,81,88]) and their computations [90, 100–102]. The existence of coherent structures implies that the dominant dynamic behavior of transitional and turbulent flows can be approximately described by finite-dimensional systems.

This realization has motivated significant research on the problem of deriving

low-order ODE systems that accurately reproduce the dynamics and solutions of fluid flows. An approach to address this problem involves the application of standard Galerkin's method with empirical eigenfunctions (e.g., [11,39,101,102]) to the Navier-Stokes equations to perform model reduction. Even though this approach has been shown to be very effective, it does require knowledge (which may not always be available) of the flow field for a wide range of initial conditions in order to compute the empirical eigenfunctions using Karhunen-Loève expansion. An alternative approach to low-dimensional modeling of fluid flows is based on the concept of inertial manifold (IM) [107]. If it exists, an IM is a positively invariant, exponentially attracting, finite-dimensional Lipschitz manifold. The IM is an appropriate tool for model reduction because if the trajectories of the Navier-Stokes are on the IM, then this system is exactly described by a low-order ODE system (called inertial form). Unfortunately, even for fluid flows for which an IM is known to exist, the computation of the closed-form expression of the IM (and therefore the derivation of the corresponding inertial form) is a formidable task. Motivated by this, various approaches have been proposed in the literature for the construction of approximations of the inertial manifold (called approximate inertial manifolds (AIMs)) (see, for example, [29,31,42,44]). The AIMs are subsequently used for the derivation of approximations of the inertial form that accurately reproduce the solutions and dynamics of the flow field. The combination of Galerkin's method with AIMs leads to nonlinear Galerkin's method (e.g., [11,39, 45,63,97,108]). Finally, another approach to low-dimensional modeling of fluid flows is based on the reduced basis methods (e.g., [63,64]).

Over the last decade, several efforts have been directed towards the design and implementation of feedback control systems on various fluid flows. The approach followed for controller design typically involves the derivation of low-order ODE

approximations of the Navier-Stokes equations which describe the flow field using advanced discretization schemes including linear and nonlinear Galerkin's methods (e.g., [4, 39, 108]) and reduced basis methods (e.g., [64, 72]). These ODE systems are subsequently used for the design of low-order output feedback controllers. This approach has led to the design of robust optimal controllers for flow in a driven cavity [19, 21, 71], linear optimal and robust controllers for channel flow using boundary (blowing and suction) control actuation [34, 35, 66], linear controllers for flow over flat plate using distributed (electromagnetic forcing) control actuation [103], and linear and nonlinear controllers for suppression of wavy behavior exhibited by fluid dynamic systems described by the Korteweg-de Vries-Burgers [3] and Kuramoto-Sivashinsky [2, 3, 30] equations. In addition to controller design, efforts have been made to understand the amplification of disturbances in three-dimensional channel flow using singular value decomposition of the linear spatial differential operator of the flow field [9, 10]. An alternative approach to controller design is based on the concept of designing a feedback controller so that the time-derivative of an appropriate Lyapunov functional along the trajectories of the closed-loop system is negative definite and has been used to design controllers for channel flow [8, 70], Korteweg-de Vries-Burgers [77] and Kuramoto-Sivashinsky [76] equations. Other results on flow control include the solution of the optimal control problem for the Navier-Stokes equations with distributed control [40, 61] and proportional-integral control [14, 27, 28, 67], finite dimensional optimal control of Poiseuille flow [68], control of long-wavelength Marangoni-Benard convection [85], robust control of Rayleigh-Benard convection [84], control of mixing in fluid flow [37], modeling and control of shear flows [82], and feedback control of thermal fluids using state estimation [20]. The reader is referred to the recent survey paper [16] for additional results on flow control.

The United States Air Force Research Laboratory/VACA (AFRL/VACA) Flow Control Theory and Optimization Branch focuses on several fluid dynamics problems that are significant to the United States Air Force. There are numerous methods that can be incorporated to analyze these fluid dynamics problems. A valid way to analyze fluid dynamics problems is through the use of the finite element method (FEM). Because of the high computational load inherent in the simulation of fluid flow, few results are available on closed-loop feedback control of fluids. However, current levels of computational power permit the solution of certain abridged fluid dynamics problems (lower Reynolds numbers, coarser mesh) with the finite element method. Imminent increases in computational power will provide the means to solve even more complicated fluid dynamics problems with the finite element method in the future.

AFRL/VACA is interested in the simulation of flow past a circular cylinder. There is particular interest in suppressing the vortex shedding in the wake behind the body by implementing control with rotary oscillations of the cylinder. AFRL/VACA has studied this pertinent fluid dynamics problem using the incompressible Navier - Stokes equation and the finite element method. The $MATLAB^{TM}$ (The Mathworks, Incorporated, Natick, Massachusetts) programming environment is used in conjunction with the third party $MATLAB^{TM}$ extension $FEMLAB^{TM}$ (Comsol, Incorporated, Stockholm, Sweden). The $FEMLAB^{TM}$ software is designed specifically for solving partial differential equations with the finite element method.

Control of flow past a circular cylinder is studied for a number of practical reasons. Wake modification, reduction of flow-induced vibrations, design of heat exchangers, and improvement of chemical mixing are among the diverse applications involving flow past a circular cylinder. This problem is also studied for stall control and lift

enhancement as well as for design of aerodynamic vehicles.

The formation of vortices behind the flow past a circular cylinder above a critical Reynolds number has been well-documented, both numerically and experimentally (e.g., [12, 105, 109, 114] as well as many others). Initially, at flows below Reynolds number 10, streamlines form around the cylinder. The fluid travels along the boundary of the cylinder as it moves by. Starting at Reynolds numbers above 10, the streamlines separate from the boundary behind the cylinder and vortices are formed. The vortices remain behind the cylinder. At Reynolds number above roughly 47, these vortices are successively formed and then shed from the top and bottom of the cylinder periodically. The regular pattern of shedding vortices is called the von Karman vortex street [12, 17]. Williamson [113, 114] has made numerous studies on cylinder wakes, especially determining the relationship between vortex shedding frequency and Reynolds number. The effective control of drag on the cylinder has been a challenge that has received particular attention. The drag force on the cylinder may be reduced by active control in the form of rotational oscillation. Taneda [105] made early visual observations and studied the effect of oscillation on bluff bodies. Tokumaru et al. [109] conducted experiments on flow past a cylinder at Reynolds number 15,000 for a variety of amplitudes and frequencies of oscillation, finding that significant drag reduction is possible with open-loop active control. Shiels et al. [96] extended Tokumaru's work numerically. Protas et al. [89] conducted numerical studies at Reynolds number 150 and multiple forcing conditions. Lu et al. [78] conducted a numerical parametric study of rotational cylinder oscillation at a few different Reynolds numbers. He et al. [57] reviewed a few different numerical methods for studying drag reduction on a circular cylinder, as did Li et al. [73]. L. Li et al. [74], Cheng et al. [26], Fujisawa et al. [46], and Shiels et al. [96] have studied the phenomenon of vortex lock-on, where

the natural vortex shedding frequency is controlled by the forced cylinder oscillation.

Studies have also been conducted on closed-loop control of the circular cylinder wake. Roussopoulos [93] conducted an experimental study where the wake of a circular cylinder in low Reynolds number flow is stabilized by feeding back velocity data from the flow field behind the cylinder using acoustic actuation. Singh et al. [99] used linear optimal control theory to control a reduced-order cylinder flow model that is constructed by applying proper orthogonal decomposition (POD) to flow field data (see also [2–5, 30] for further results on linear/nonlinear feedback control of fluid dynamic systems using reduced-order models and [1] for a recent review of results on feedback control of fluid flows). Gillies [53] used multiple sensors to control the one-dimensional Ginzburg-Landau equation, which is a PDE model that captures some of the stability features of the two-dimensional cylinder wake. Park et al. [87] used blowing/suction actuation on the one-dimensional Ginzburg-Landau equation and examined the effect of sensor location on the performance of the feedback controller.

Although much work has been done on the system of flow past the circular cylinder, much of the work focuses on the a general view of the system. Very little work has been done on closed-loop control, especially with rotational oscillation as a means of actuation. The small body of work that has been done on closed-loop control of flow over a circular cylinder with rotational oscillation has chiefly been experimental.

1.3 Proper Orthogonal Decomposition and the Galerkin Projection of the Navier - Stokes Equations

Proper Orthogonal Decomposition (POD) is a method for obtaining a low-dimensional, approximate description of a high-dimensional distributed parameter system. Proper Orthogonal Decomposition is also known as the Karhunen-Loéve decomposition and

Principal Component Analysis. POD was developed originally by Lumley [79]. Lumley used POD to identify the most energetic coherent structures in a turbulent flow field [106]. The benefit of obtaining a low-order model of a system is that control theories for finite-dimensional systems may be used for the design of flow controllers. Proper Orthogonal Decomposition results in a set of orthogonal basis functions (or empirical eigenfunctions) that are optimal with respect to capturing the energy of the data set [55]. Using these orthogonal basis functions, the dominant spatial features of the system are captured. The orthogonal eigenfunctions, also known as modes, are taken from a autocorrelation tensor of the flow variables [24]. Using the POD modes, a Galerkin Projection of the governing Navier-Stokes equations results in a set of ordinary differential equations that represent the system [55]. The Galerkin Projection provides a way of obtaining the evolution equations for the time-varying modal amplitudes [52]. The Proper Orthogonal Decomposition method is explained in detail in [59].

Holmes et al. [60] examined turbulence generation, using a POD to model inertial range transport and energy dissipation. Taylor and Glauser [106] used POD in conjunction with Linear Stochastic Estimation (LSE) based low-dimensional methods to model the flow over a backward-facing ramp with an adjustable flap above the ramp which allowed for dynamic variation of the pressure gradient. Cohen et al. [33] also used POD and LSE to evaluate the effectiveness of a sensor configuration for feedback flow control on the wake of a circular cylinder. Caraballo et al. [24] used numerical simulation data of subsonic flow over a shallow cavity to obtain POD modes and subsequently used Galerkin Projection to obtain a low-dimensional model. Rowley et al. [94] used a POD model and Galerkin Projection to study compressible flows using an energy-based inner product. Graham et al. [55] examined the use of POD

and Galerkin Projection in detail for flow past a rotating cylinder. Refer to [15] for a comprehensive review of applications of POD to different flows.

1.4 Thesis objectives and structure

This thesis examines the effect of active control on two-dimensional, incompressible viscous flow past a circular cylinder and control of flow past a flat plate using blowing/suction actuation. Specifically, using the finite element method, simulations are set up for two cases: flow past a cylinder in a specified, small channel (benchmark problem) and in an essentially infinite fluid. The effect of oscillatory rotation of the cylinder on the drag is evaluated.

Initially, a description of each of the simulations is provided. The governing equations for both the flow field and the drag measurement are explained. The geometry of each of the problems is provided. Then, for each problem, the solution of the flow field for the stationary cylinder is given. The drag on the cylinder in the benchmark problem is validated against available numerical studies and contrasted with the infinite fluid results. The drag on the cylinder in the infinite fluid is compared to both numerical and experimental studies at several different Reynolds numbers. After this, the methodology for implementing active control by rotary oscillations of the cylinder is described. The drag on the cylinder in both the benchmark and infinite fluids is examined at several different combinations of frequencies and amplitudes of rotation and is compared to other studies. Results are obtained over a wide range of parameters. For the benchmark case, the results of closed-loop control simulations are discussed. A proportional controller and a proportional-integral controller are implemented and evaluated. A novel active controller is also implemented and evaluated.

The Proper Orthogonal Decomposition (POD) technique is combined with a Galerkin Projection of the Navier-Stokes equations to produce a reduced-order, nonlinear, coupled set of ODEs that represent the flow past a circular cylinder. Using the finite element method, the Navier-Stokes equations are solved for flow past a circular cylinder. Initially, the POD method and Galerkin Projection are described. Then, the geometry and discretization structure of the problem are specified. Two different mesh structures are used. The two different definitions of inner product (vector and integral) are defined. Two different POD definitions are employed; one based on the total velocity, and the other based on velocity fluctuations only. The POD modes produced are illustrated. The reconstruction of the flow field is demonstrated. The modal amplitudes are calculated. A simple proportional derivative (PD) controller is applied to the POD model. A Galerkin Projection of the Navier-Stokes equations is used to produce a low order model of the system. The effect of the pressure term in this model is demonstrated. The reduced-order model is simulated at a few different Reynolds numbers. A way to implement open-loop control with such a reduced-order model is discussed.

Flow over a flat plate is another well-studied problem, particularly from the standpoint of boundary layer control. This problem emulates, among other systems, flow over a wing. This thesis examines the reduction of frictional drag exerted on a flat plate using active feedback control. Several alternative control configurations, including both pointwise and spatially uniform control actuation and sensing, are developed and tested through computer simulations. All control configurations use control actuation in the form of blowing/suction on the plate and measurements of shear stresses along the plate. The simulation results indicate that the use of active feedback control, which employs reasonable control effort, can significantly reduce the frictional

drag exerted on the plate compared to the open-loop values.

This thesis will further the state-of-the-art by providing additional insight into the system of flow past the circular cylinder with stationary cylinder simulations. Further insight will be gained by conducting several open-loop forcing simulations over a wide range of parameters. These insights will lead to a design for an active controller that will consistently reduce drag over a range of Reynolds numbers. A reduced-order model will provide additional insight by introducing a methodology for systematic model-based control laws. The state-of-the-art for the flow over the flat plate is furthered by the development of a novel active feedback controller that is effective at reducing drag.

Chapter 2

Flow Field: Description and Governing Equations

2.1 Introduction

In this chapter, the geometry of the two circular cylinder flow problems solved in this work is described. The two-dimensional, viscous, incompressible Navier-Stokes equations that govern this flow are then described along with boundary conditions used. An exact solution of the Navier-Stokes equations at low Reynolds numbers is subsequently provided. Finally, specific details required for setting up the problem, such as the method of rotation, the discretization mesh, verifying mesh independence, and the calculation of drag force, are given.

2.2 Geometry, equations, and boundary conditions

Two different geometries are considered for this study. The diameter of the cylinder in both cases is 0.1. First, a benchmark problem is considered. A schematic of this flow field and its relative dimensions are given in Figure 2.1. Initially, flow field data

from these simulations are compared against a study by Schäfer [95] that summarized results for drag measurements for the same geometry from several different sources. The second geometry simulated is shown schematically in Figure 2.2. This simulation

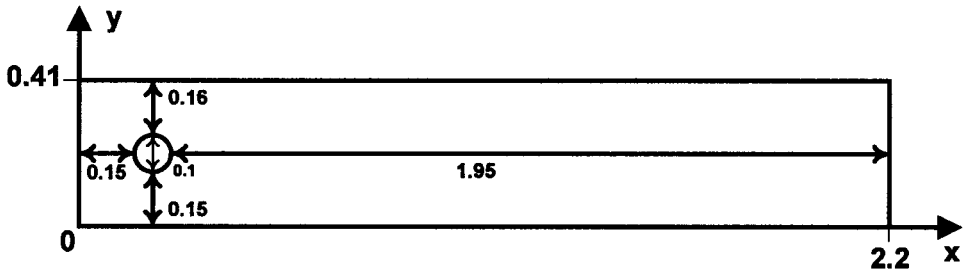

Figure 2.1: Schematic of the flow field for the benchmark problem.

approximates flow past a rotating cylinder in an unbounded or infinite fluid. If the effects of the boundaries of the channel can be ignored with respect to the forces acting on the cylinder, then the flow field approximates an infinite fluid. Li et al. [73] state that the lateral boundary effect can be neglected when the ratio of lateral boundary width to cylinder diameter is greater than five. As shown in Figure 2.2, the ratio of lateral channel boundary width to cylinder diameter in this study is 60, and the ratio of channel length to cylinder diameter is 70. We consider a two-dimensional incompressible, viscous flow past a cylinder through these channels. The incompressible Navier-Stokes equation is used to solve this fluid dynamic problem.

To present the various equations that describe the flow, we use the characteristic time, $t = \frac{d}{U_{mean}}$, where d is the diameter of the cylinder and U_{mean} is the mean velocity in the channel, as well as the Reynolds number, $Re = \frac{U_{mean}\, d}{\nu}$, where ν is the kinematic viscosity. For all simulations the kinematic viscosity ν is 0.001. In two dimensions, the Navier-Stokes equations take the following non-dimensionalized form:

$$\frac{\partial u}{\partial x} + \frac{\partial v}{\partial y} = 0 \tag{2.1}$$

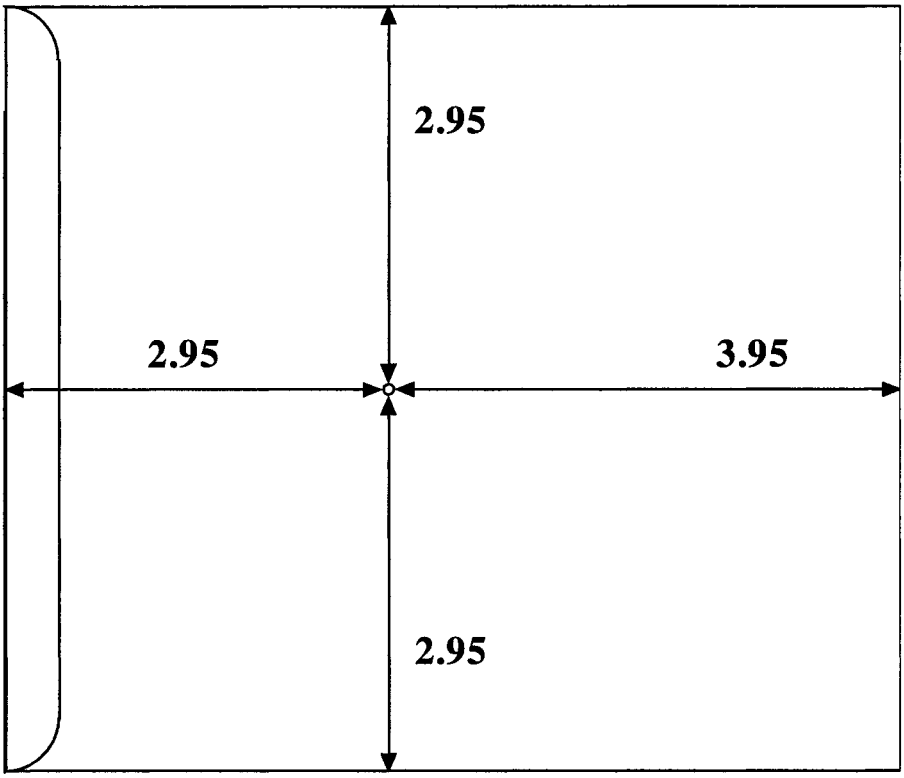

Figure 2.2: Schematic of the flow field for the infinite fluid problem.

$$\begin{aligned} \frac{\partial u}{\partial t} + u\frac{\partial u}{\partial x} + v\frac{\partial u}{\partial y} &= -\frac{\partial p}{\partial x} + \frac{1}{Re}(\frac{\partial^2 u}{\partial x^2} + \frac{\partial^2 u}{\partial y^2}) \\ \frac{\partial v}{\partial t} + u\frac{\partial v}{\partial x} + v\frac{\partial v}{\partial y} &= -\frac{\partial p}{\partial y} + \frac{1}{Re}(\frac{\partial^2 v}{\partial x^2} + \frac{\partial^2 v}{\partial y^2}) \end{aligned} \tag{2.2}$$

where u and v are the components of the velocity along the x (parallel to the channel wall) and y (normal to the channel wall) axes, respectively, and p is the pressure. Equation 2.1 is the continuity equation. Equation 2.2 is subject to the following no-slip, no-penetration boundary conditions at the top and bottom walls of the channel:

$$\begin{aligned} u(x, y = 0, t) &= u(x, y = max, t) = 0 \\ v(x, y = 0, t) &= v(x, y = max, t) = 0 \end{aligned} \tag{2.3}$$

Uncertainties about the nature of the velocity and pressure profiles at the outlet of the flow field prohibit the use of traditional boundary conditions, such as assuming zero total force or axial force, or assuming some fully developed profile [86]. The free boundary condition, as implemented by Baker et al. [6] and described by Papanastasiou et al. [86] and Renardy [92], is employed at the outlet boundary. Evaluating the solution of the flow field with the free boundary condition can be accomplished by determining the surface and volume integrals from the residuals of the Navier-Stokes equations formed during discretization. A boundary condition cannot be dropped at the partial differential equation level. However, after the equation is discretized, employing the free boundary condition can be compared to setting $\frac{\partial^3 u}{\partial x^3}$ equal to zero, which is an extrapolation condition [92]. The pressure is specified as a constant at the outlet boundary:

$$p(x = max, y, t) = 0 \tag{2.4}$$

According to Papanastasiou et al. [86], specifying the pressure at the outlet boundary improves convergence. For stationary cylinder simulations, the boundary of the cylinder is subject to the same no-slip, no-penetration boundary conditions in Equation

2.3. For the benchmark problem, the inlet boundary condition is the following:

$$\begin{aligned} u(x=0,y,t) &= 4U_{max}y(1-y) \\ v(x=0,y,t) &= 0 \end{aligned} \tag{2.5}$$

where U_{max} is the maximum incoming velocity in the center of the channel. In the case of the inlet boundary for the infinite fluid case, the inlet boundary condition is a 30^{th} order polynomial function for u, depicted by the curve shown on the left boundary in Figure 2.2, that has the value of U_{max} for the bulk of the flow field, and zero for v.

The use of the incompressible Navier-Stokes equations implies that both the density, ρ, and the viscosity, μ, are constant. Additionally, in order to use the Navier-Stokes equations to describe a flow field, the continuum hypothesis must apply. The mass of a fluid is concentrated in the nuclei of the atoms that compose the fluid. The continuum hypothesis assumes that, despite these distinct 'point' masses, fluids can be treated as continuous structures and, therefore, physical properties are considered to be spread uniformly over a unit volume instead of being concentrated at points [12]. A substance can be treated as a continuum if the mean free path (distance a molecule travels between collisions) is much smaller than the length scale of the system.

The Navier-Stokes equations also apply to turbulent flow. In order for solutions to be found, however, the equations must be modified. Variables are split into time-averaged (or time-smoothed) and fluctuating components [17, 43].

2.3 Solution at low Reynolds number

Batchelor [12] provides a solution for the two-dimensional Navier-Stokes equations for flow around a rigid circular cylinder at low Reynolds numbers. With the help of the Oseen's variation of the equations of motion, the flow field near a cylinder can be

computed [12]. Starting with expressions for the pressure drop and the vorticity, ω $(= \nabla \times u)$,

$$\begin{aligned} \frac{p - p_o}{\mu} &= \frac{C\mathbf{U}\cdot\mathbf{x}}{r^2} \\ \omega &= \frac{C\mathbf{U}\times\mathbf{x}}{r^2} \end{aligned} \tag{2.6}$$

where **U** is the velocity of the cylinder (Batchelor [12] considers a cylinder moving in a stationary fluid, which is equivalent to the problem of flow moving past a stationary cylinder considered here), C is a constant, and (r,θ) are the polar coordinates of the two-dimensional vector **x**. Expressing the stream function, $\psi = U sin\,\theta f(r)$, and

$$\frac{d^2 f}{dr^2} + \frac{1}{r}\frac{df}{dr} - \frac{f}{r^2} = -\frac{C}{r} \tag{2.7}$$

which gives

$$f(r) = -\frac{1}{2} Cr \log r + Lr + Mr^{-1} \tag{2.8}$$

where

$$\begin{aligned} L &= 1 + \frac{1}{4} C + \frac{1}{2} C \log a \\ M &= -\frac{1}{4} a^2 C \end{aligned} \tag{2.9}$$

and a is the radius of the cylinder, yielding a velocity distribution **u**,

$$\mathbf{u} = \mathbf{U} + C\mathbf{U}(-\frac{1}{2} \log\frac{r}{a} - \frac{1}{4} + \frac{1}{4}\frac{a^2}{r^2}) + C\mathbf{x}\frac{\mathbf{U}\cdot\mathbf{x}}{r^2}(\frac{1}{2} - \frac{1}{2}\frac{a^2}{r^2}) \tag{2.10}$$

where

$$C = -\frac{2}{\log 7 \cdot \frac{4}{Re}} \tag{2.11}$$

and the coefficient of drag (discussed below) is calculated from the Reynolds number,

$$C_D = \frac{8\pi}{Re \log 7 \cdot \frac{4}{Re}} \tag{2.12}$$

This solution is applicable only for flow past a cylinder at very low Reynolds numbers. Equation 2.12 yields values of C_D that are consistent with experimental observations near Reynolds number 0.5 [12].

2.4 Rotation of the cylinder

To simulate a rotating cylinder, the no-slip boundary conditions used for the stationary cylinder are modified. The cylinder is subjected to periodically oscillating boundary conditions, described by the following:

$$\begin{aligned} u &= yA\sin(2\pi ft) \\ v &= -xA\sin(2\pi ft) \end{aligned} \tag{2.13}$$

The rotational boundary conditions are shown schematically in Figure 2.3. These

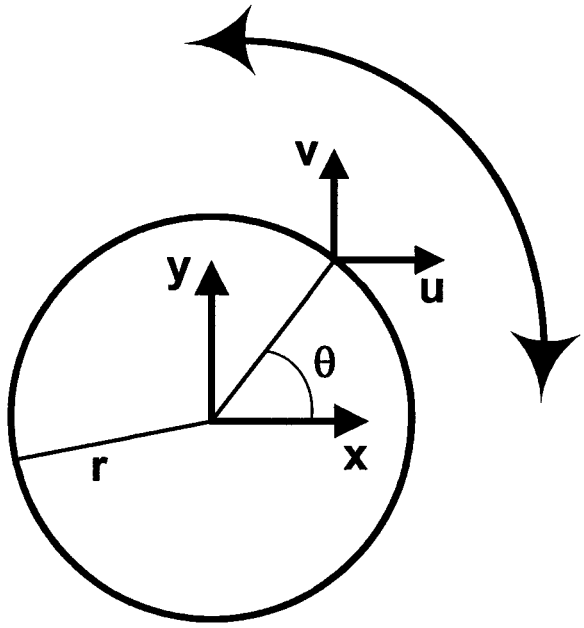

Figure 2.3: Diagram of cylinder in oscillatory rotation.

boundary conditions result in an overall rotation of the cylinder with amplitude A and frequency f.

2.5 Discretization

These simulations are solved within the FEMLAB simulation environment that uses a finite element approach to compute the solution of the flow field as described by the

above equations. The exact form of the spatial discretization mesh is shown in Figure 2.4 for the benchmark problem, and the mesh for the infinite fluid problem is shown in Figure 2.5. The most dynamic region in the flow field is around and directly behind

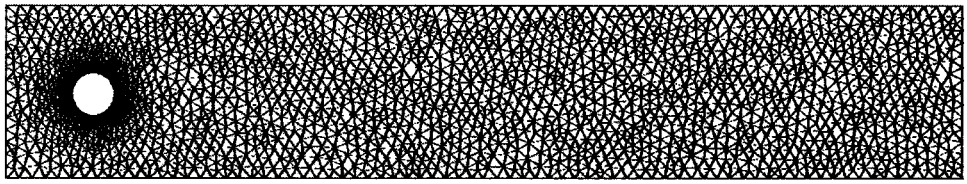

Figure 2.4: Spatial domain and finite element mesh for the benchmark problem.

the cylinder. Because the largest velocity gradients are present in these regions, the mesh is very refined around the cylinder edges. To reduce the computational load of this demanding problem, the mesh is less refined further away from the cylinder, where less change is taking place over time and space.

In the case of the benchmark problem, the domain has a total of 2366 nodes, 240 edges, and 4492 elements. For the infinite fluid, there are 4395 nodes, 238 edges, and 8552 elements in the domain. In each case, around the cylinder itself, there are 64 edges. The fine resolution around the cylinder in each case is necessary for accurate measurement of the drag exerted by the fluid on the cylinder.

2.6 Mesh independence

In order to establish the fact that the solution to the flow field is not dependent on the structure of the mesh used or the number of finite elements employed, several simulations are performed with varying mesh configurations. These results are compared. The solution of the flow field is considered to be mesh independent and, therefore, the level of discretization is considered to be adequate, when the computed values of the properties of the flow field do not change significantly as increasing numbers of

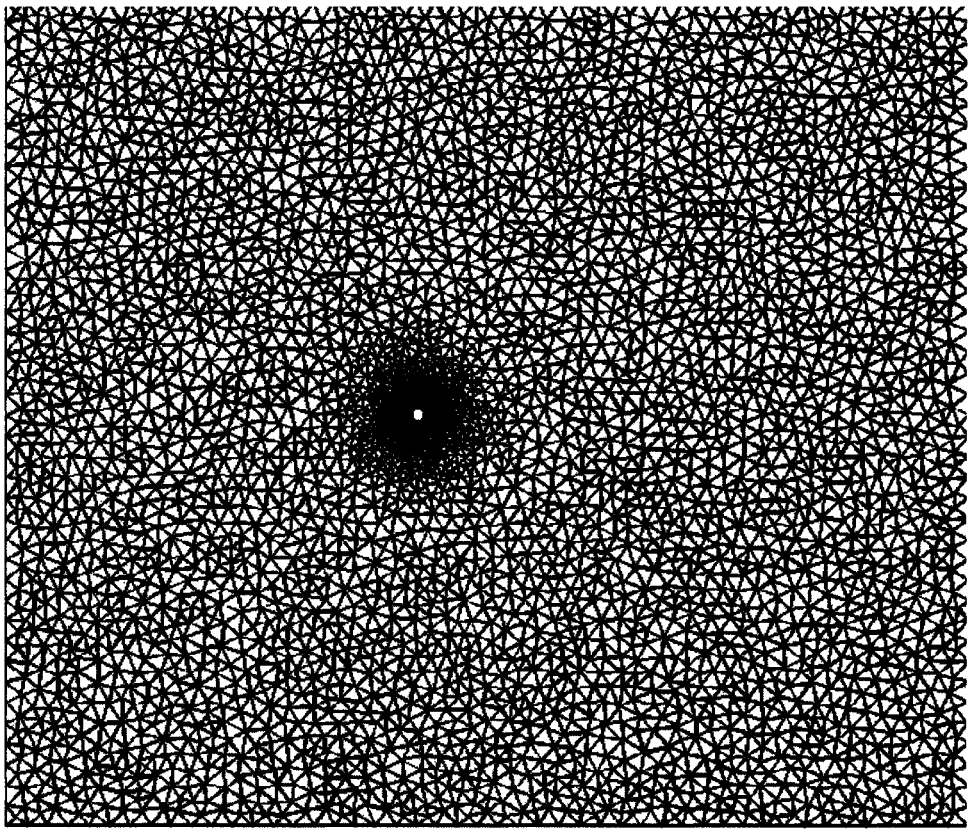

Figure 2.5: Spatial domain and finite element mesh for the infinite fluid problem.

finite elements are employed.

Table 2.1 shows the results from simulations with different numbers of elements for each mesh. Three different cases are shown: the benchmark problem at Reynolds

Table 2.1: U^2 and C_D for different mesh.

Benchmark, Re 20			
No. of elements	U^2	C_D	% dev. of C_D from max no. of elements
641	0.043734	5.5830	0.0573
1960	0.043737	5.5797	0.0018
4492	0.043733	5.5803	0.0090
5928	0.043733	5.5795	0.0054
8852	0.043733	5.5805	0.0125
17968	0.043733	5.5798	0
Benchmark, Re 100			
516	1.1395	2.8361	11.197
1052	1.1881	3.1092	2.6458
2218	1.2037	3.1742	0.6106
4492	1.2065	3.1868	0.2161
9367	1.2074	3.1937	0
Infinite, Re 100			
1028	34.114	1.0963	16.9344
2054	33.976	1.2100	8.3194
4120	33.674	1.3186	0.0909
8552	33.160	1.2921	2.0988
11258	33.986	1.3198	0

numbers 20 and 100, and the infinite fluid problem at Re 100. To quantify the changes in the flow field as the number of mesh elements is increased, the quantity U^2 ($= u^2 + v^2$) is integrated over the entire flow field. To quantify the effect

of varying the number of elements around the edge of the cylinder, C_D (discussed below) is calculated around the cylinder for each simulation. Assuming that the mesh with the largest number of elements yields the most accurate solution, values of U^2 and C_D can be compared to the values found in the simulation with greatest number of elements to determine whether or not each solution is mesh-independent. As Table 2.1 shows, U^2 remains relatively constant as the number of mesh elements is increased for each of the three cases. Except for the benchmark case at Reynolds number 100 with the least number of elements (516) and the infinite fluid case with the 2 least numbers of elements (1028 and 2054), the values of C_D are reasonably close in every other case to C_D in the simulation with largest number of elements. This indicates that mesh-independent solutions can be achieved in each case with most of the mesh configurations examined. For both the benchmark case and the infinite fluid case, a relatively large number of mesh elements is employed to ensure the accuracy of the solutions in situations where larger gradients in velocity and pressure are present around the edge of the cylinder. These larger gradients are characteristic of simulations of the rotating cylinder.

2.7 Vortex shedding

The formation of vortices behind the flow past a circular cylinder above a critical Reynolds number has been well-documented, both numerically and experimentally (e.g., [12, 105, 109, 114] as well as many others). Initially, at flows below Reynolds number 10, streamlines form around the cylinder. The fluid travels along the boundary of the cylinder as it moves by. Starting at Reynolds numbers above 10, the streamlines separate from the boundary behind the cylinder, and vortices are formed. The vortices remain behind the cylinder. At Reynolds number above roughly 47,

these vortices are successively formed and then shed from the top and bottom of the cylinder periodically. The regular pattern of shedding vortices is called the von Karman vortex street [12, 17]. In these two-dimensional problems, the cylinder is considered to be infinitely long and the effects that might be present due to the ends of the cylinder in 3-D are ignored.

At Reynolds number 100, vortices are shed regularly at a frequency f which has different values for various geometries. To facilitate comparison of dissimilar flow fields, dimensionless frequency, called the Strouhal number St, is defined by the following relationship:

$$St = \frac{f\,d}{U_{mean}} \tag{2.14}$$

The Strouhal number will be the same for infinite flow fields at a given Reynolds number, regardless of the cylinder diameter or the mean velocity. The natural Strouhal number, St_{nat}, is obtained by using the natural vortex shedding frequency, f_{nat}, for f in Equation 2.14 [96].

2.8 Drag force on the cylinder

A cylinder moving through a fluid experiences a drag force, F_D, in the direction parallel to the flow. This force has two components: frictional (or viscous) drag, F_{frict}, and pressure (or form) drag, F_{press}. The frictional drag is caused by the formation of the boundary layer on the surface, while pressure drag is attributable to the formation of the wake behind the cylinder. The pressure drag, F_{press}, is the component of pressure that is normal to the surface of the cylinder, and the frictional drag, F_{frict}, is the tangential component of the shear stress [13, 69, 112]. The total drag, F_D, is defined by Juárez at al. [69], Whitaker [112], and L. Li et al. [74] in the

following way:

$$F_D = \int_\Gamma (-P\mathbf{n} + \tau \cdot \mathbf{n})(s) \cdot \mathbf{e}_x ds \tag{2.15}$$

where P is the pressure, $\mathbf{n}$ is unit outward normal vector at the boundary, τ is the viscous stress tensor defined at a generic point s defined on the boundary Γ of the cylinder, and $\mathbf{e}_x$ is the unit vector in the x coordinate direction. The first term of the integral is F_{press}, and the second term is the contribution from F_{frict}. In this case, $\tau = \mu(\nabla\mathbf{u} + (\nabla\mathbf{u})^T)$, where

$$\nabla\mathbf{u} = \begin{bmatrix} \frac{\partial u}{\partial x} & \frac{\partial v}{\partial x} \\ \\ \frac{\partial u}{\partial y} & \frac{\partial v}{\partial y} \end{bmatrix} \tag{2.16}$$

As a result of Equation 2.16, the contribution from F_{frict} is computed from the following equation:

$$F_{frict} = \int_\Gamma (\tau \cdot \mathbf{n})(s) \cdot \mathbf{e}_x ds = \mu \left(\mathbf{n}_x 2 \frac{\partial u}{\partial x} + \mathbf{n}_y \left(\frac{\partial u}{\partial y} + \frac{\partial v}{\partial x} \right) \right) \tag{2.17}$$

where $\mathbf{n}_x$ and $\mathbf{n}_y$ are the outward unit normal vectors in the x and y coordinate directions, respectively [69, 74].

At low Reynolds numbers, the pressure drag is significantly larger than the frictional drag for bluff bodies. Protas et al. [89] observed that, for the circular cylinder at Reynolds number 150, the pressure drag constitutes approximately 81% of the total drag.

Vortex shedding from the cylinder occurs at Reynolds numbers above the critical value of roughly 47. This vortex shedding results in fluctuations of the drag force on the cylinder. Vortices are shed from alternate sides of the cylinder. As each vortex is shed, a force is applied to each side of the cylinder. As the vortices are shed over time, applying forces to alternating sides of the cylinder, the overall mean drag fluctuates.

The objective of implementing active control in this problem is to reduce the overall drag experienced by the cylinder. The non-dimensional drag coefficient (per

unit length) is defined by the following expression:

$$C_D = \frac{F_D}{\frac{1}{2}\rho U_{mean}^2 d} \tag{2.18}$$

where F_D is the total drag force on the cylinder as defined in Equation 2.15, ρ is the density of the fluid, which is unity for these simulations, and d is the diameter of the cylinder, which is 0.1 in all cases [12].

2.9 Conclusions

The flow problems in this study are governed by the viscous, incompressible Navier-Stokes equations. An exact solution for the Navier-Stokes equations in the case of flow past a circular cylinder can only be obtained for very low Reynolds number, and was given here for Re = 0.5. In simulations in which the cylinder is rotated, the oscillations are sinusoidal and occur around the center of the cylinder. The flow problems were solved with the finite element method, with the finest parts of the finite element mesh being located around the perimeter of the cylinder. This refined mesh was required to yield accurate drag calculations. The solutions found were shown to be mesh independent. The drag force on the cylinder has both pressure drag and frictional drag components, with pressure drag being dominant at the Reynolds numbers examined in this study.

Chapter 3

Solution of the Flow Field for the Stationary Cylinder

3.1 Introduction

In this chapter, the benchmark and infinite fluid problems are described. Comparisons are made to the literature for, where applicable, both numerical and experimental results. The non-dimensional natural shedding frequency, the Strouhal number, is compared to numerical and experimental results for the infinite fluid case. Finally, the contribution of friction and pressure drag to the overall drag is discussed and illustrated for Reynolds numbers in the range of 50 to 500.

3.2 Benchmark problem

In a study to compare different solution methods, Schäfer et al. [95] compared the results of 15 approaches by groups that were tasked to solve the same benchmark problem at Reynolds number 20 and 100. Part of this study was repeated by the FEMLAB Model Library [62]. At Reynolds number 20, after reaching a steady flow,

the drag on the cylinder remains constant over time. Vortices are formed behind the cylinder at this Reynolds number but remain attached to the cylinder and are not shed into the flow field. The resulting C_D computed by the groups in the study be Schäfer et al. was between 5.57 and 5.59 [95]. Using the FEMLAB environment, the solution of the flow field for the same problem is obtained, and the average C_D is 5.58, which is the same as the result given in the FEMLAB Model Library [62]. The velocity field, U $(= \sqrt{u^2 + v^2})$, at Reynolds number 20 for the benchmark problem is shown in Figure 3.1. Solutions of the benchmark problem at Reynolds number 100

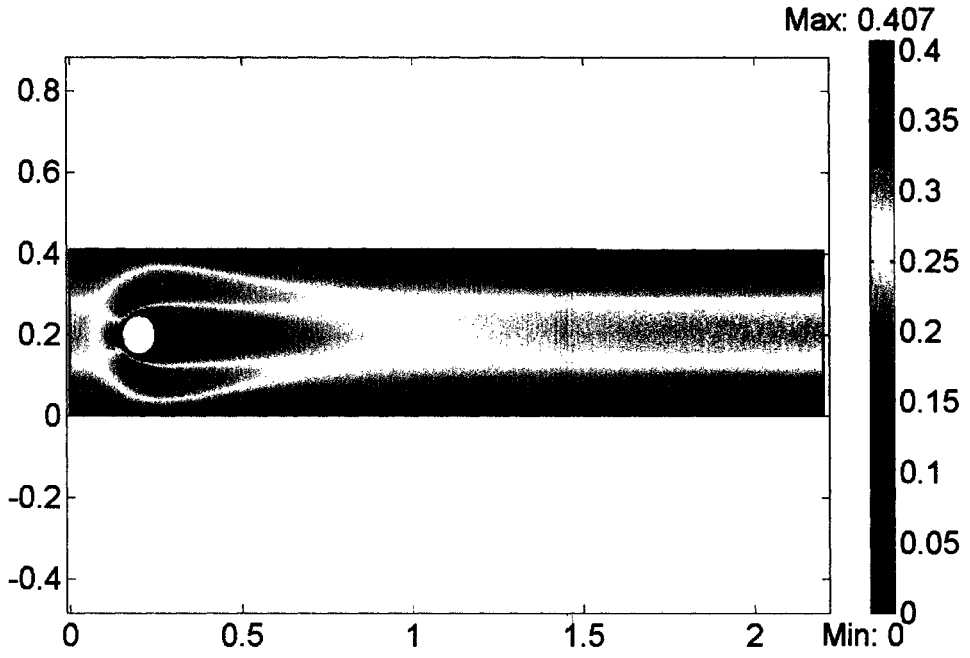

Figure 3.1: Total velocity (U) surface plot for the benchmark problem at Re = 20.

are also summarized in Schäfer et al. [95]. A total of ten different approaches were used. Based on these results, the maximum C_D is between 3.22 and 3.24 [95]. For this study, the resulting maximum drag coefficient is 3.22, which is the same as the result given in the FEMLAB Model Library [62]. The variation of drag coefficient over time for the benchmark problem is shown in Figure 3.2. Because the values of C_D

at Reynolds numbers 20 and 100 in this study agree with values obtained in previous studies on the the same benchmark study, the model for the benchmark problem in this study is validated. After the maximum drag is reached, the value of C_D exhibits

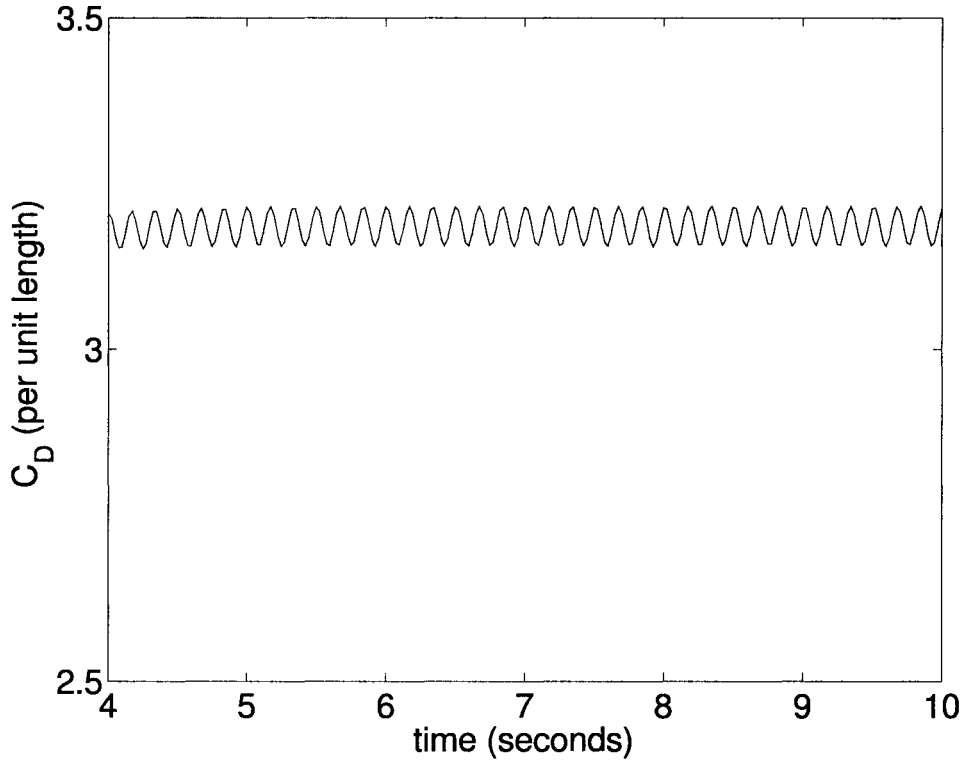

Figure 3.2: Variation of C_D over time for the benchmark problem at Re = 100.

small oscillations around its mean value, 3.17. The velocity field (U) after 10 seconds at Reynolds number 100 is shown in Figure 3.3. Because the total velocity surface plot of the benchmark system at Reynolds number 20 (Figure 3.1) has a stationary steady state as expected and the total velocity surface plot at Reynolds number 100 (Figure 3.3) has a periodic oscillatory steady state as expected, the model for the benchmark problem in this study is further validated.

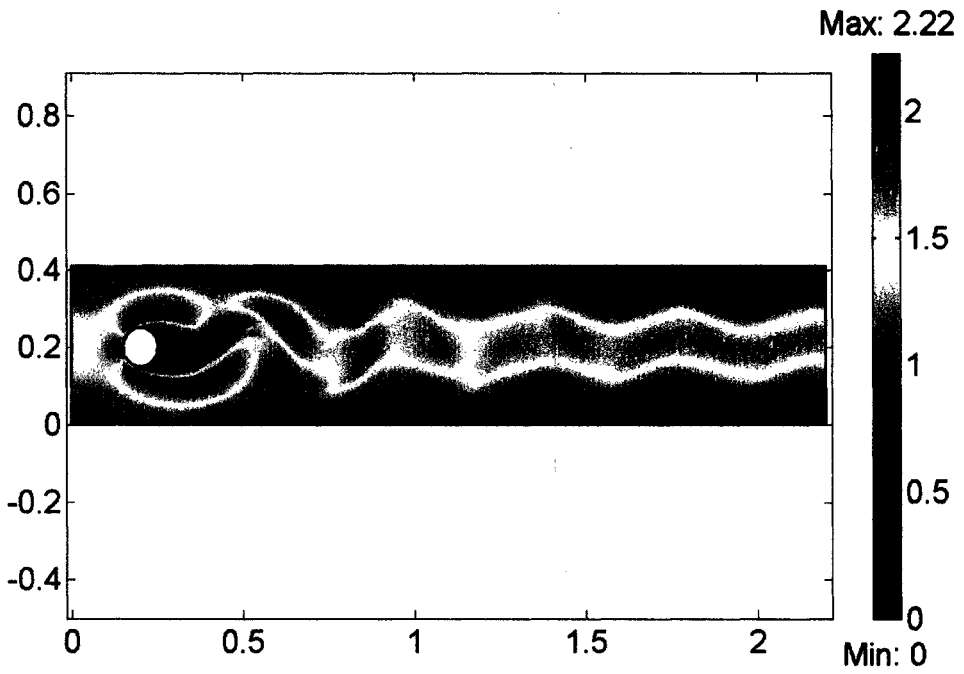

Figure 3.3: Total velocity (U) surface plot for the benchmark problem at Re = 100.

3.3 Infinite fluid problem

The vast majority of the previous studies on flow past a viscous, incompressible flow have focused on an 'infinite' flow field. The channel in which the cylinder is located is large enough such that the forces acting on the cylinder are not influenced by the walls of the channel. Li et al. [73] states that, when the ratio of the lateral boundary width to the cylinder diameter is greater than 5, the lateral boundary effect can be neglected. For this study, for the infinite fluid, the lateral channel boundary width to cylinder diameter ratio is 60, and the channel length to cylinder ratio is 70. To prevent the chance of the inlet boundary condition artificially affecting the drag on the cylinder, the cylinder is placed 30 diameters away from the inlet of the channel.

To validate the infinite fluid model used in this study, the coefficient of drag on the cylinder is compared to other numerical and experimental investigations at several

Reynolds numbers. Figure 3.4 compares the results of this study to the experimental results of Tritton (as shown by Batchelor [12]) and the numerical results of He et al. [57], Henderson [58], and Braza et al. [18] at several different Reynolds numbers. Shiels et al. [96] has also made consistent observations. At Re 100, the value of C_D also agrees well with a study by Li et al. [73] (1.33-1.35). As shown, the results of this study are in good agreement with other studies.

The stationary benchmark problem is further extended to other Reynolds numbers. Figure 3.4 shows the relationship between *log* C_D and *log* Re for benchmark compared to the infinite fluid. Both problems follow the same trend of decreasing C_D with increasing Reynolds number.

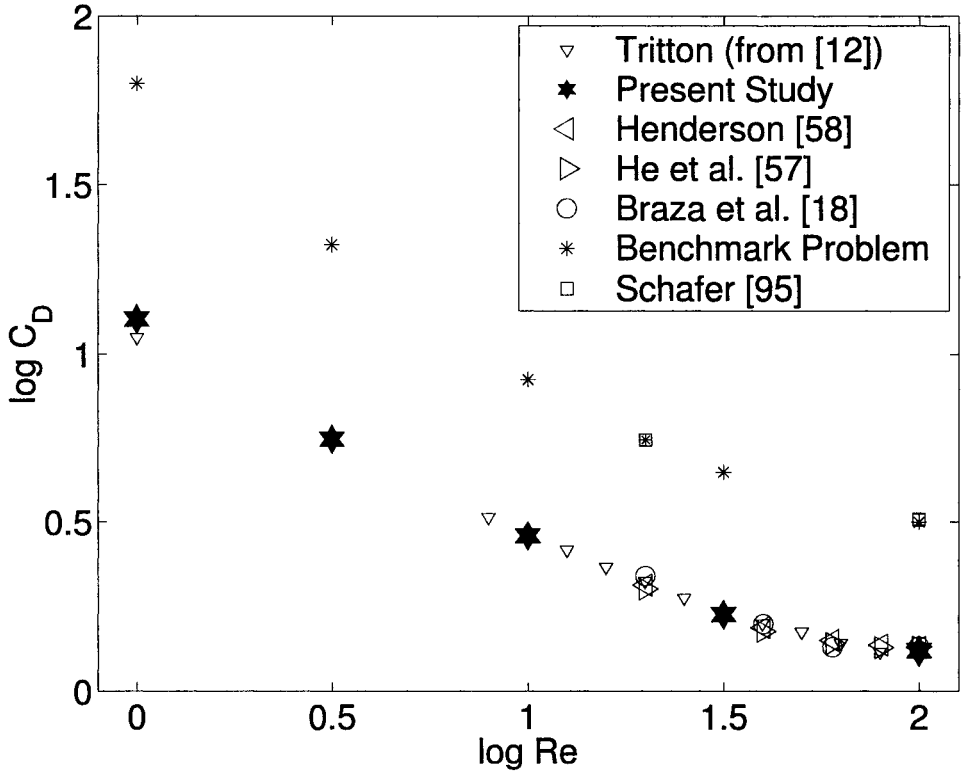

Figure 3.4: C_D at various Reynolds numbers from different studies.

A surface plot of the velocity field (U) for the infinite fluid after 10 seconds at

Reynolds number 100 is shown in Figure 3.5.

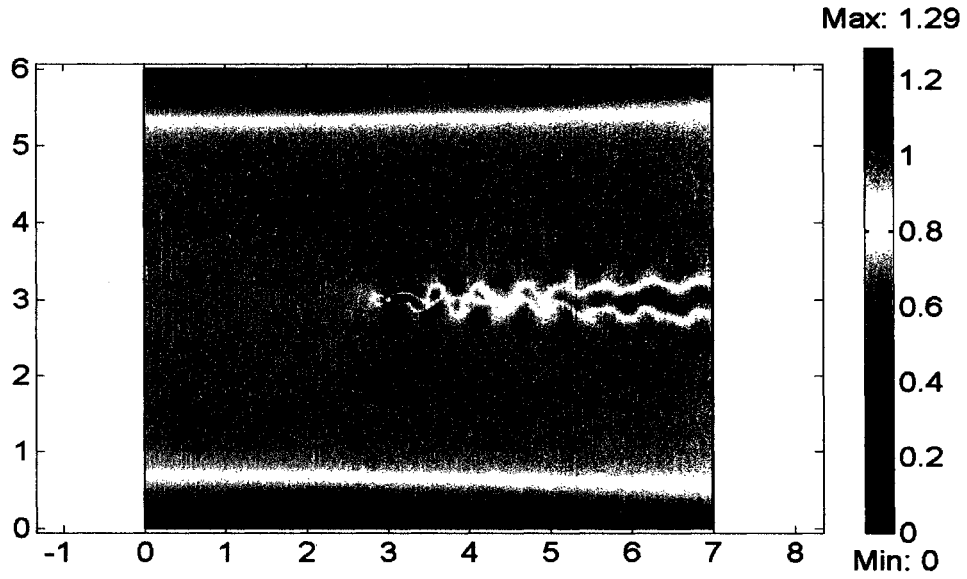

Figure 3.5: Total velocity (U) surface plot for the infinite fluid problem at Re = 100.

3.4 Natural shedding frequency

At Reynolds numbers greater than a critical value, in incompressible, viscous flow, vortices develop in the wake behind the cylinder and are shed into the passing fluid. The shed vortices form a periodic pattern known as the von Karman vortex street [12, 17]. According to Williamson [114], the critical Reynolds number is 49, while Li et al. [73] cites a range of 35 - 47 from a few different researchers. For this study, the critical Reynolds number is taken as 47.

At a given Reynolds number, the vortices are shed from the cylinder at characteristic natural frequency, f_{nat}, corresponding to a non-dimensionalized frequency called the Strouhal number, $St_{nat} = \frac{f_{nat}\, d}{U_{mean}}$. For the benchmark problem, f_{nat} at Reynolds number 100 is determined to be 3.0, which corresponds to St_{nat} of 0.30. For the infinite fluid, the natural frequency is 1.6 at Reynolds number 100, which results in a

St_{nat} of 0.16. The value of St_{nat} for the infinite fluid agrees closely with several other studies [18, 57, 58, 73, 89, 113] as shown in Table 3.1 (data from the first five studies are obtained from He et al. [57]) .

Table 3.1: St_{nat} at Re = 100 from various studies.

Study	St_{nat}
Present Work	0.16
Braza et al. [18]	0.16
He et al. [57]	0.1670
Henderson [58]	0.1664
Williamson [113]	0.1640
Roshko [57]	0.1670
Li et al. [73]	0.158-0.163
Protas et al. [89]	0.167

For both the infinite fluid and the benchmark problem, the frequency of vortex shedding varied linearly with Reynolds number from Re 1 to Re 500, as shown in Figure 3.6 and Figure 3.7. Williamson [113, 114] presents data from several studies regarding the relationship between Strouhal number and Reynolds number, and the present study agrees well with these results.

3.5 Pressure drag vs. friction drag

As discussed in Section 2.8, the total drag force, F_D, consists of two components: the pressure drag, F_{press}, and the friction drag, F_{frict}. For a bluff body at low Reynolds number such as the circular cylinder studied in the present work, the majority of the drag force comes from the pressure drag. Protas et al. [89] found that, at Reynolds number 150 for the circular cylinder, F_{press} constitutes roughly 81% of the total drag.

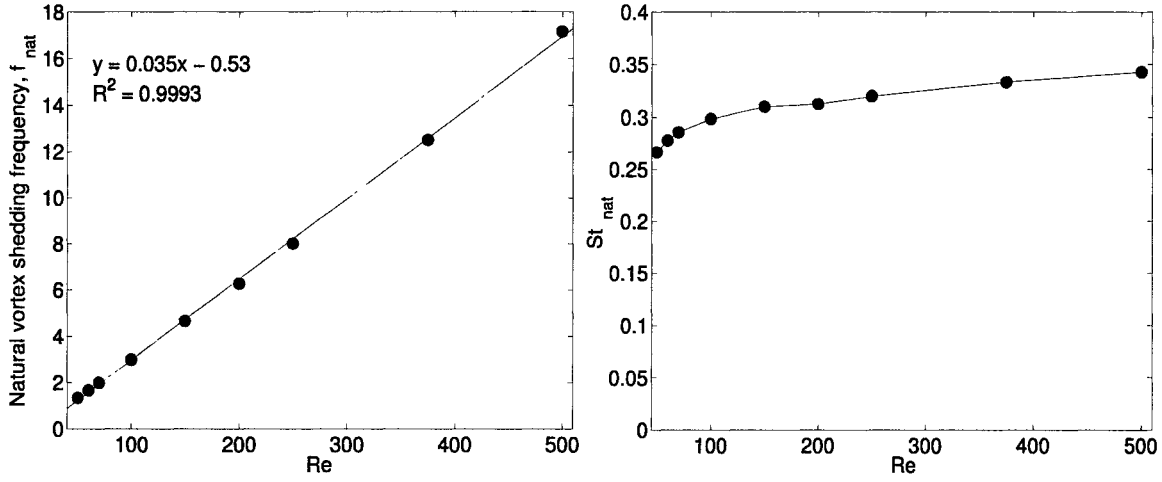

Figure 3.6: Relationship between vortex shedding and Reynolds number for the benchmark problem - Left: in terms of frequency, Right: in terms of Strouhal number.

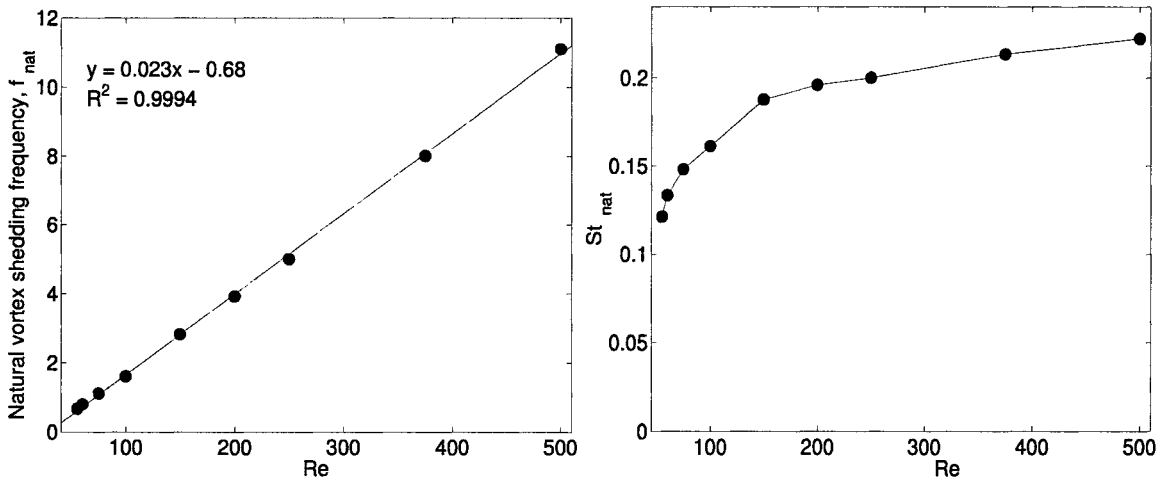

Figure 3.7: Relationship between vortex shedding and Reynolds number for the infinite fluid problem - Left: in terms of frequency, Right: in terms of Strouhal number.

This value is in agreement with that found in the present study. Table 3.2 shows what percent F_{press} accounted for the total F_D for four different Reynolds numbers simulated in this work.

Table 3.2: Percent contribution of F_{press} to F_D at various Re, infinite fluid.

Reynolds number	$\frac{F_{press}}{F_D}$ (%)
100	74.23
150	78.05
200	80.60
250	82.44

In this range of Reynolds numbers, the pressure drag contribution varies logarithmically with the Reynolds number, as shown in Figure 3.8 for the benchmark problem. Although this trend is exhibited for this range of Reynolds number values, this may not be the case for Reynolds numbers much larger than 500. The same trend is also seen in the infinite fluid, as shown in Figure 3.9. Because the primary contribution to the drag on the cylinder over Reynolds number 100 comes from the pressure drag, any effective drag modification at this Reynolds number (or greater) must be achieved by changing the pressure drag [89].

3.6 Conclusions

The benchmark and infinite fluid cases of the flow over a circular cylinder problem that are the focus of this study were discussed. The flow field of the benchmark problem was illustrated by a surface plot, showing that the flow field reaches a constant steady state for Re = 20. The flow field for the benchmark and infinite fluid cases were also shown at Re = 100, at which point the flow field has a periodic oscillatory steady state.

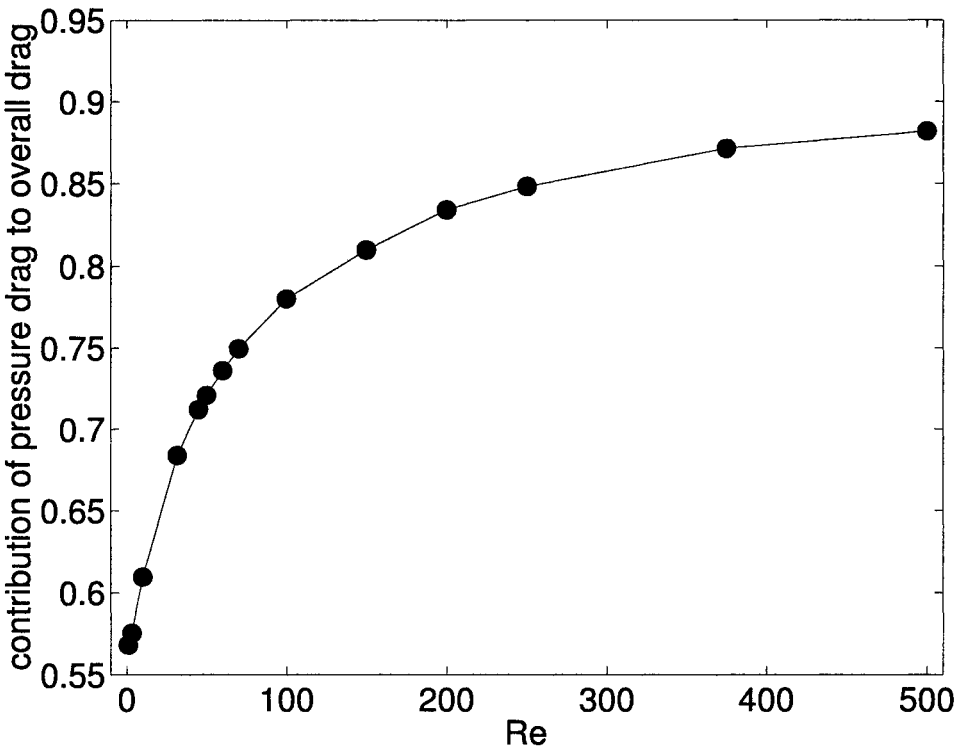

Figure 3.8: Contribution of F_{press} to F_D for varying Reynolds number for the benchmark problem.

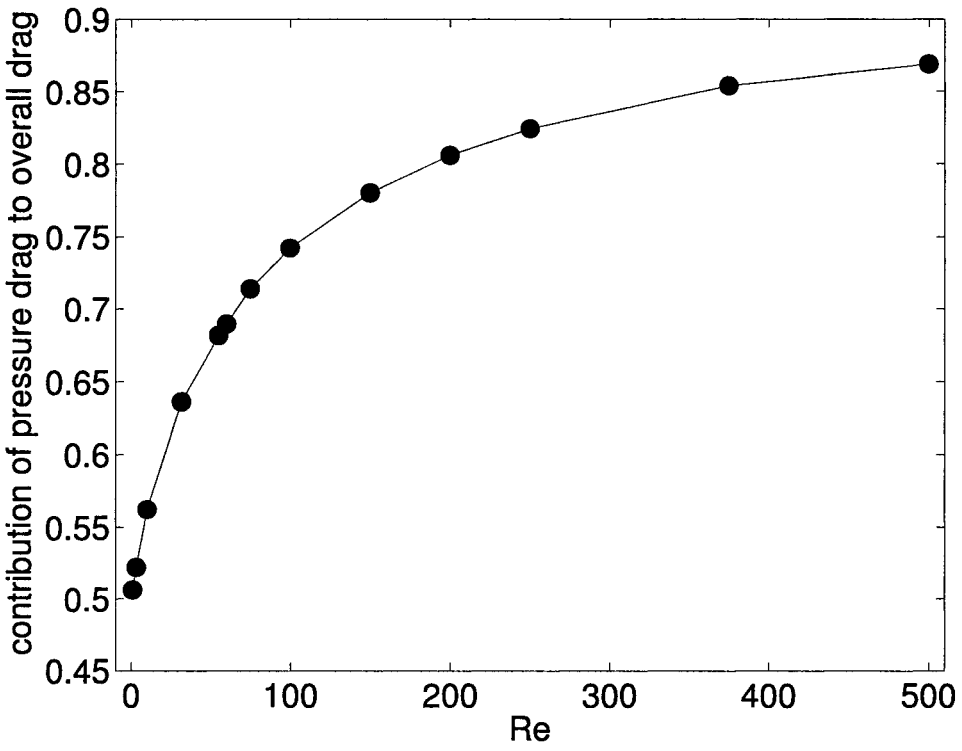

Figure 3.9: Contribution of F_{press} to F_D for varying Reynolds number for the infinite fluid problem.

Because of this, the drag profile oscillates regularly at this Reynolds number. The non-dimensional shedding frequency, $St_{nat} = 0.16$, of the infinite fluid at Reynolds number 100 was shown to match both experimental and numerical results. Finally, the contributions of pressure drag and frictional drag to the overall drag are shown for both the benchmark and infinite fluid cases. Although the contributions are roughly equal at very low Reynolds number, as the Reynolds number increases, the pressure drag dominates the overall drag for the circular cylinder and bluff bodies in general. The pressure drag component, therefore, must be altered to effectively reduce drag.

Chapter 4

Open-loop Control

4.1 Introduction

In this chapter, the effect of open-loop rotational oscillation on the benchmark and infinite fluid problems is shown. Several simulations with varying parameters (frequency and amplitude of rotation) are conducted. Trends in the drag reduction, grouped by varying frequency, varying amplitude, and total drag reduction are shown for Reynolds number 100. Comparisons are made to other studies of rotational oscillation of a circular cylinder at different Reynolds numbers. An observation about the amount of fluctuation in the drag versus time is made. Finally, the phenomena of wake stabilization by rotation and phase lock-on are demonstrated.

4.2 Rotational oscillation

There have been numerous studies, both experimental and numerical, that have focused on reducing drag past a circular cylinder by active control. There are several possible actuation methods for active control, including acoustic forcing, transverse or in-line oscillation, and rotational oscillation. Among these methods of active con-

trol actuation, rotational oscillation is of particular interest to the United States Air Force. Protas et al. [89], Lu et al. [78], and Fujisawa et al. [46] have cited several papers, including review papers, on the topic of reduction of drag on a cylinder by oscillatory rotation.

There are three main parameters which may be varied for uniform flow past a rotationally oscillating cylinder: Reynolds number, $Re = \frac{U_{mean}\, d}{\nu}$, forcing Strouhal number, $St_f = \frac{f_f\, d}{U_{mean}}$ (where f_f is the forcing frequency), and A, the amplitude of rotation [78]. For purposes of comparison, some studies report their results in terms of $R_{f/n} = \frac{St_f}{St_{nat}}$, the ratio of the forcing Strouhal number to the natural Strouhal number, and $W = \frac{A\, d}{2U_{mean}}$, the normalized amplitude.

Most of the open-loop simulations in the present study are conducted at Reynolds number 100. The cylinder is oscillated in our simulations by changing the no-slip boundary conditions, $u = v = 0$, on the cylinder to the following:

$$\begin{aligned} u &= yA\sin(2\pi ft) \\ v &= -xA\sin(2\pi ft) \end{aligned} \tag{4.1}$$

4.3 Frequency variation with fixed amplitude

Several studies [46,78,89,104] have observed the effect of frequency variation at a fixed amplitude on drag, initiated by the study of Tokumaru et al. [109]. These studies have observed the same trends from varying frequency in drag reduction regardless of differences in Reynolds number. At a fixed normalized amplitude (W = 2), Figure 4.1 shows the variation of C_D with $R_{f/n}$ for the present work at Reynolds number 100. Qualitatively, this agrees well with the results of Protas et al. [89] and Lu et al. [78]. At the same normalized amplitude and at Reynolds number 15,000, Tokumaru et al. [109] found the same results experimentally, as did Srinivas [104] for numerical simulations.

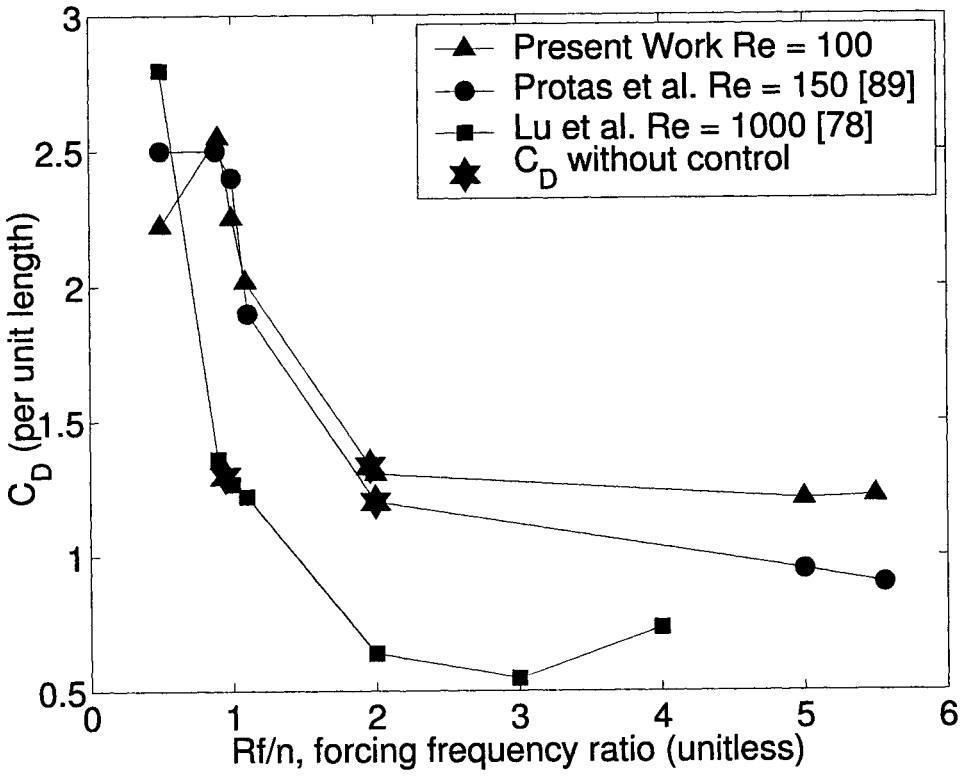

Figure 4.1: Change in C_D vs. $R_{f/n}$, W = 2, for the infinite fluid problem for different Reynolds numbers.

One of the characteristics of the trend of drag versus frequency illustrated in Figure 4.1 is the sharp increase to roughly twice the unforced (without control) value of C_D when the forcing Strouhal number, St_f, is equal (or nearly equal) to the natural vortex shedding Strouhal number, St_{nat} (where $R_{f/n}$ is 1). At $R_{f/n}$ slightly greater than and slightly less than 1, C_D falls off sharply. At $R_{f/n}$ greater than around 2.5, C_D falls below the value of C_D without control, reaching a minimum around $R_{f/n} = 5$. Both Protas et al. [89] and the present study find the unforced value of C_D at $R_{f/n} = 2$. Cheng et al. [26] also noted the large increase in drag at $R_{f/n} = 1$. This trend of the peak value of C_D occurring at $R_{f/n} = 1$ followed by a sharp decrease in C_D is more pronounced at greater amplitudes [26].

Unlike the other studies (as shown in Figure 4.1), at Reynolds number 1000, Lu et al. [78] observed the drop in C_D at $R_{f/n} = 1$. However, they did observe the sharp increase in C_D at $R_{f/n}$ slightly less than 1 and the reduction of drag below the unforced C_D at $R_{f/n}$ greater than 1. In an experimental study, at W = 0.38 and Reynolds number 20,000, Fujisawa et al. [46] found that the drag increases at the natural Strouhal number, and also observed an overall decrease in C_D at larger forcing frequencies.

At other normalized amplitudes and fixed Re = 100 for the benchmark problem in this study, C_D changed in a similar way with respect to $R_{f/n}$. This is illustrated in Figure 4.2. The infinite fluid exhibits the same trend at varying values of W and Re = 100 as shown in Figure 4.3. At the largest values of W, C_D changes very rapidly at values of $R_{f/n}$ below 2. As W increases, the rate of change of C_D decreases below $R_{f/n} = 2$. Above $R_{f/n} = 2$, changes in W do not result in large changes in C_D. At $R_{f/n} = 5$, very little change in C_D is seen even when W is increased by a factor of six.

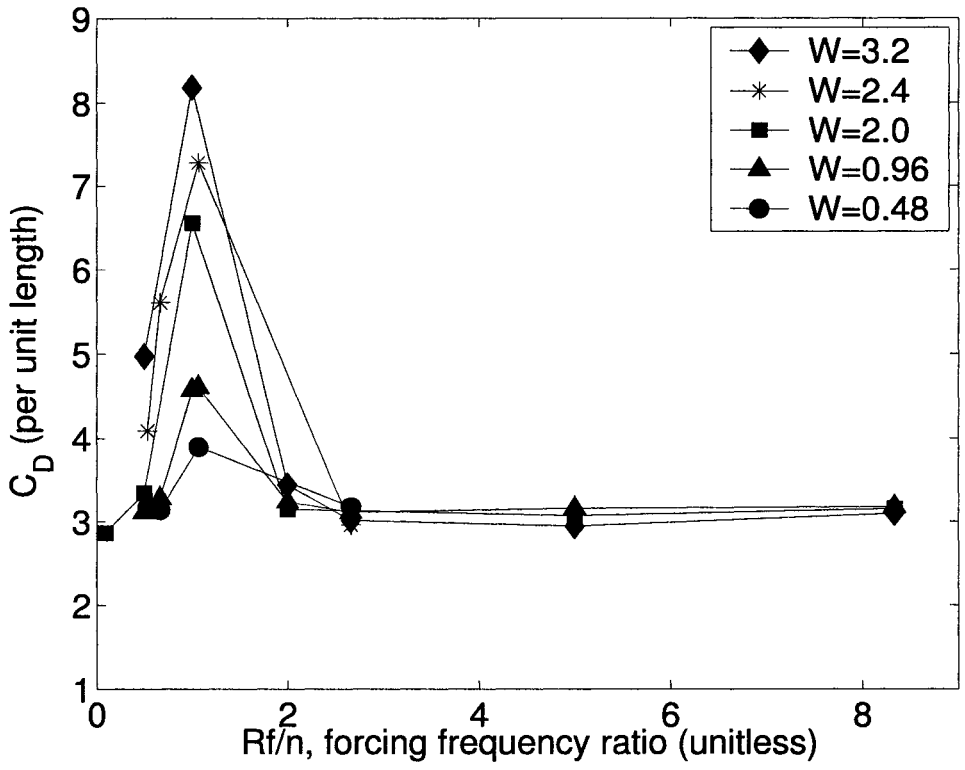

Figure 4.2: Change in C_D vs. $R_{f/n}$ for varying values of W for the benchmark problem, Re = 100.

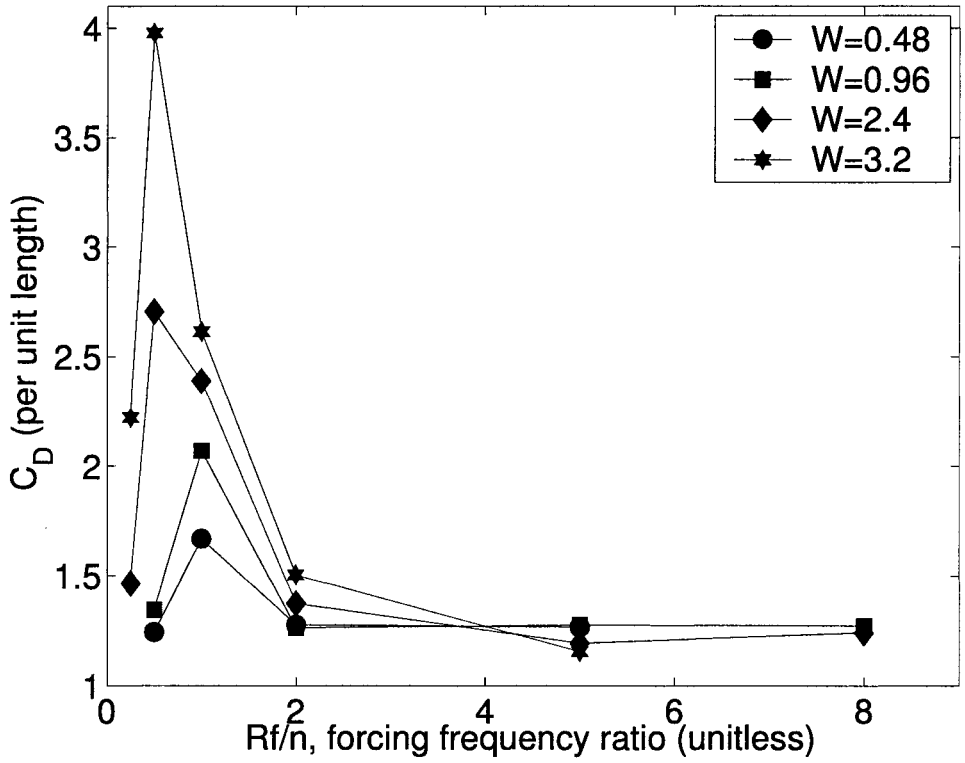

Figure 4.3: Change in C_D vs. $R_{f/n}$ for varying values of W for the infinite fluid problem, Re = 100.

The natural drag is doubled at $R_{f/n} = 1$, followed by a sharp decrease and a very low C_D at $R_{f/n} = 5$. In agreement with the infinite fluid and Protas et al. [89], at W = 2, the natural C_D is reached at an $R_{f/n}$ of 2. Increasing values of the amplitude result in greater drag at $R_{f/n} = 1$, and the minimum drag is reached between $R_{f/n}$ = 3 and 5.

4.4 Amplitude variation with fixed frequency

As shown in Figures 4.1, 4.2, and 4.3, at $R_{f/n} = 5$, an increase in amplitude results in a decrease in the drag relative to the unforced case. However, at values of $R_{f/n}$ lower than 5, the opposite trend is observed. Increases in amplitude result mostly in increases in drag. For the benchmark problem, this result is illustrated in Figure 4.4 for different values of $R_{f/n}$ and contrasted with the decrease in drag seen at $R_{f/n} = 5$. The same relationship is shown for the infinite fluid in Figure 4.5. As $R_{f/n}$ increases, the rate of change of C_D decreases with increasing W. This is shown in Figure 4.5 by the fact that the slope of the lines of C_D versus W decrease as $R_{f/n}$ increases from 0.5 to 2.0. At $R_{f/n} = 5$, the trend of C_D versus W has a slight negative slope. This decrease in C_D with increasing W occurs at ratios greater than $R_{f/n} = 2$. At $R_{f/n}$ = 2.67, C_D exhibits a slight reduction, returning to its original value as W increases. Above $R_{f/n} = 5$, the trend reverses, and C_D again increases with increasing W. The greatest reductions in C_D (with increasing W) are seen at $R_{f/n} = 5$.

4.5 Total drag reduction

Protas et al. [89] and Shiels et al. [96] have both observed that the total drag reduction that can be achieved by rotary oscillation of the cylinder is very dependent on the

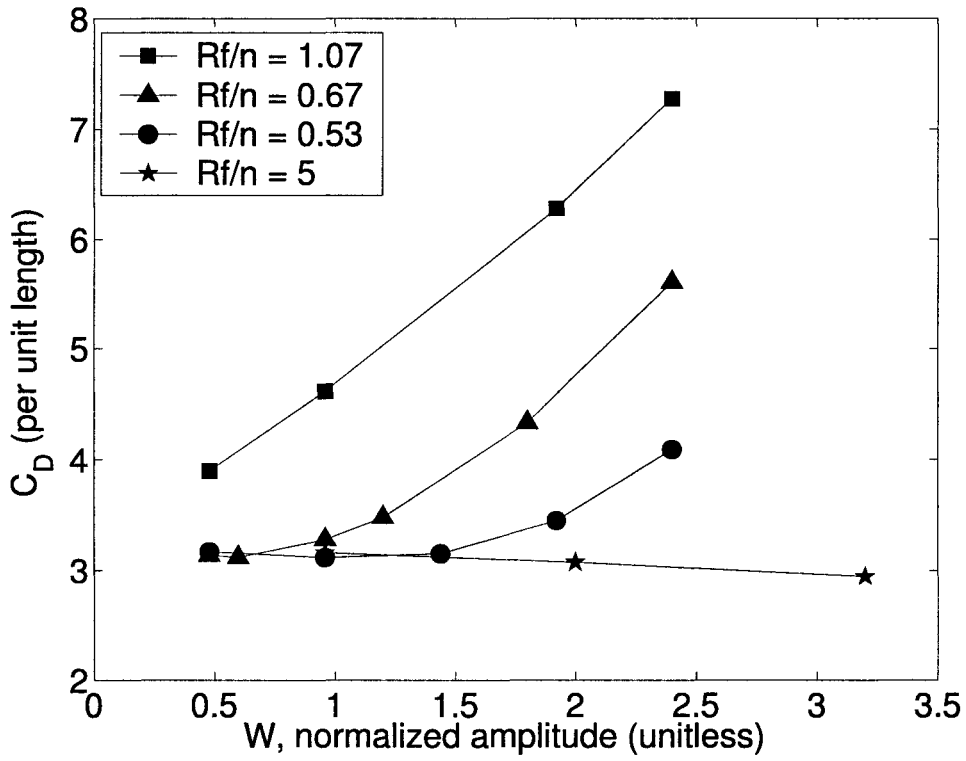

Figure 4.4: Change in C_D vs. W for varying values of $R_{f/n}$ for the benchmark problem, Re = 100.

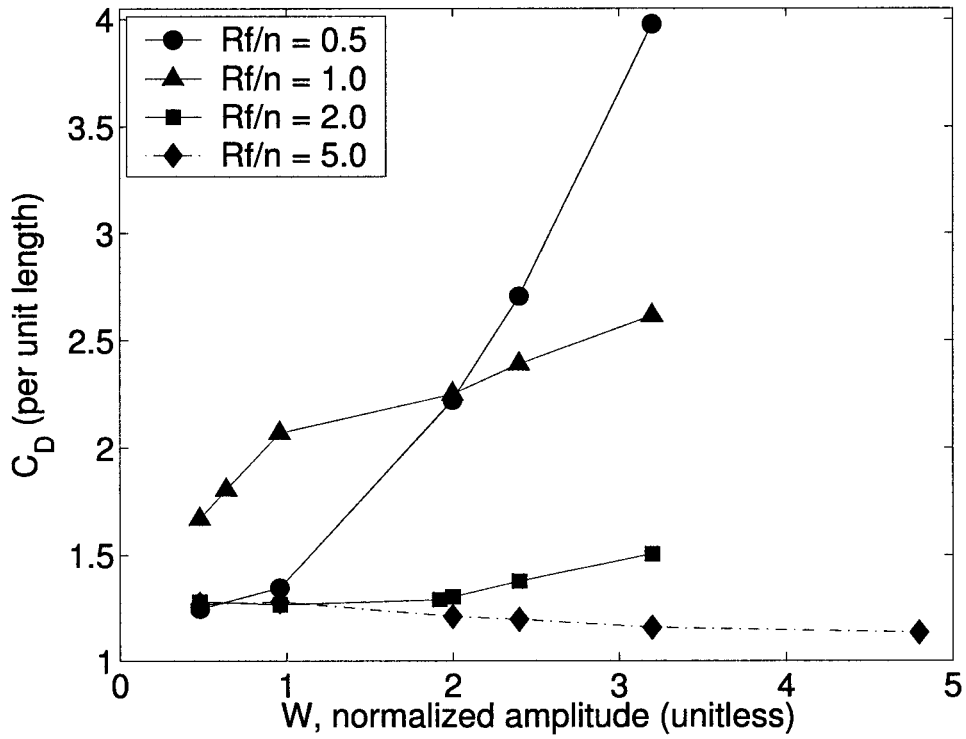

Figure 4.5: Change in C_D vs. W for varying values of $R_{f/n}$ for the infinite fluid problem, Re = 100.

Reynolds number. In his experimental studies at Reynolds number 15,000, Tokumaru et al. [109] saw a reduction in C_D from 1.4 to 0.2, an 86% decrease at a forcing ratio of $R_{f/n} = 5$ and a normalized amplitude of W = 2. Shiels et al. [96] repeated Tokumaru's experiments numerically, and saw reduction from 1.4 to 0.4, roughly a 70% decrease. Shiels attributes his larger value of C_D to the fact that his two-dimensional simulation could not capture all of the three-dimensional effects present in Tokumaru's experiment. At the much lower Reynolds number 150, but the same W and $R_{f/n}$, Protas et al. [89] saw a 25% reduction from the unforced value of 1.2 to 0.9, and notes that smaller decreases in drag are observed at lower Reynolds numbers. For the infinite fluid case, the present work is consistent with this trend, exhibiting a 9% drop in C_D at Re 100 from 1.33 to 1.21 at the same amplitude and frequency of oscillation as Tokumaru [109], Shiels [96], and Protas [89]. With the same parameters, a reduction of 3% is observed in the benchmark problem. These results are summarized in Table 4.1

Table 4.1: Percent reduction in C_D at different Reynolds numbers at $W = 2, R_{f/n} = 5$.

Study	Re	% reduction
Present Work	100	9
Protas et al. [89]	150	25
Lu et al. [78]	1000	58[1]
Shiels et al. [96]	15,000	70
Tokumaru et al. [109]	15,000	86
Benchmark Problem	100	3

At a fixed Reynolds number 100 and $R_{f/n} = 5$, as W increased, C_D decreased to a minimum and then increased. In Figure 4.6, this trend is shown as the percent

[1]Lu's minimum C_D was observed at $R_{f/n} = 3$

reduction of C_D versus W for both the benchmark and infinite fluid cases. The

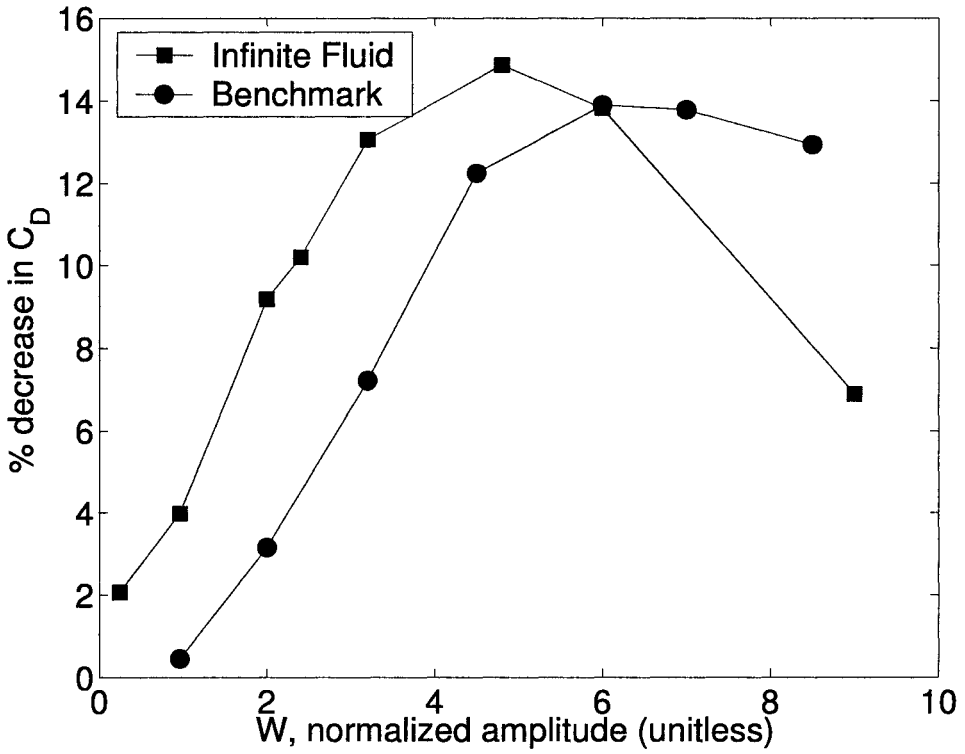

Figure 4.6: Percent reduction of C_D vs. W at $R_{f/n} = 5$ for both cases, Re = 100.

greatest reduction in drag is observed at W = 4.8 for the infinite fluid and W = 6 for the benchmark case. A similar trend is also noted by Shiels et al. [96]. In each case, the maximum drag reduction is around 14% of the stationary value of C_D.

4.6 Amount of drag fluctuation vs. time

All values of drag that have been shown thus far are mean values. The shedding of the vortices at Reynolds number 100 (or at any Reynolds number above the critical value of 47) results in fluctuations of the drag force on the cylinder over time. Vortices are shed from alternate sides of the cylinder. As each vortex is shed, a force is applied to each side of the cylinder. The vortices are shed over time, applying forces

to alternating sides of the cylinder. The overall drag fluctuates as a result of this alternating shedding. Some combinations of frequency and amplitude of rotation resulted in the same mean drag. Although these combinations of parameters had the same mean drag, the flow field sometimes exhibited different fluctuations of the instantaneous drag force. For the infinite fluid case, the mean C_D at W = 0.96 and $R_{f/n} = 1$ is essentially the same as C_D at W = 2 and $R_{f/n} = 1.094$ (2.07 and 2.02, respectively). As shown by Figure 4.7, however, the drag fluctuations over time are significantly smaller for the former case than for the latter.

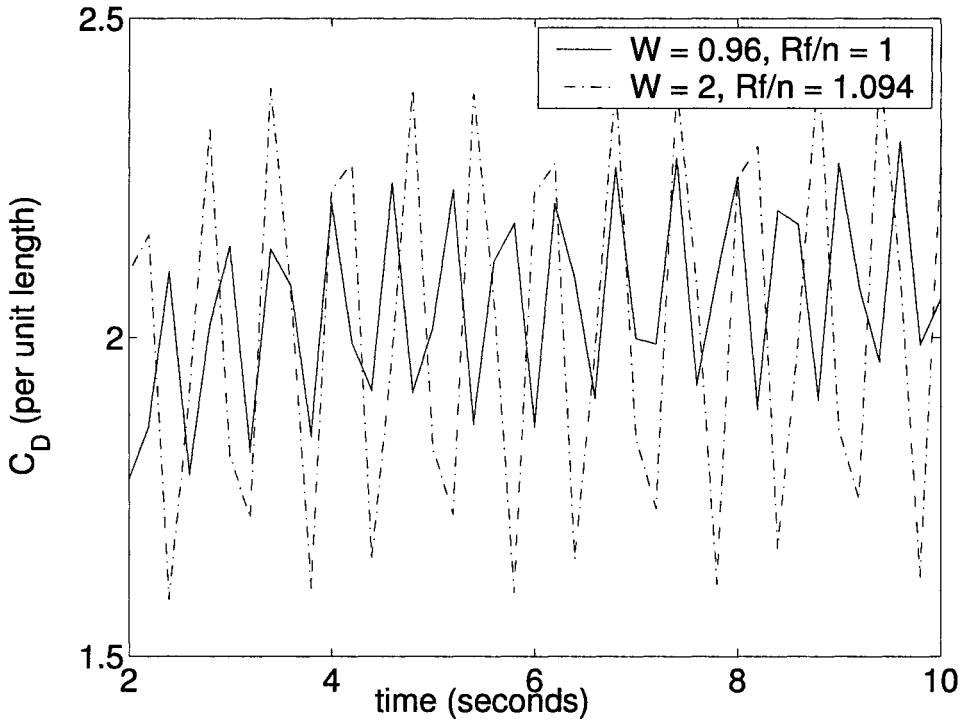

Figure 4.7: Differences in drag fluctuations over time for the same average C_D for the infinite fluid problem, Re = 100.

4.7 Rotation and wake stability

Both Tokumaru et al. [109] and Taneda [105] made observations regarding the effect of open-loop rotation on the structure of the wake behind the cylinder. At Reynolds numbers between 30 and 300, Taneda [105] noted that the 'deadwater' region, which is the region of low velocity flow immediately behind the cylinder, can be eliminated with the proper rotary oscillation. Tokumaru et. al [109], around Reynolds number 15,000, found that certain rotation conditions led to a more narrow wake than that observed behind a cylinder with no rotation at the same flow speed.

The present study illustrates the stabilizing effect of rotational oscillation. Taneda [105] showed that, in a certain range of Reynolds numbers, the proper rotational oscillation can prevent the formation of the vortices present at Reynolds numbers greater than the critical Reynolds number (which is 47 in this study). The present study has shown that rotation can prevent vortex formation at Reynolds number 60. Figure 4.8 illustrates the stabilizing effect of rotation for the benchmark problem.

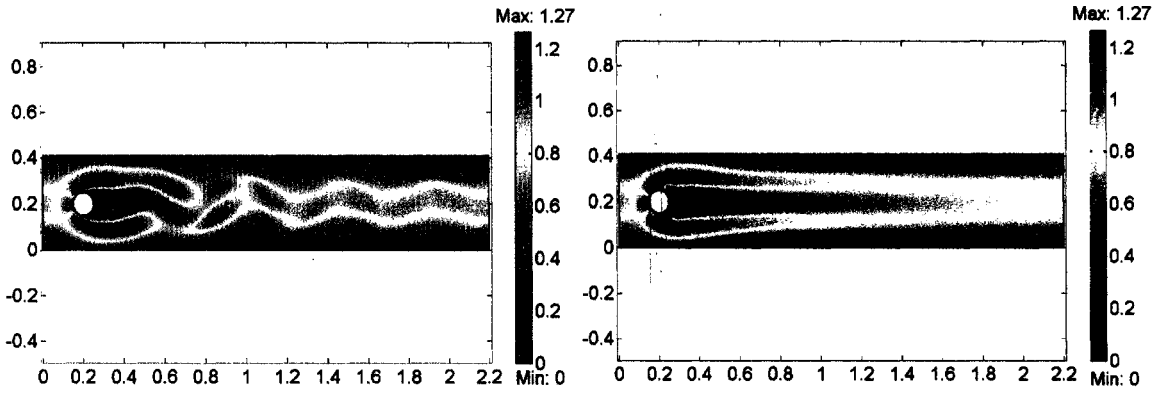

Figure 4.8: Wake stabilization at Re = 60 for the benchmark problem - Left: Total velocity (U) surface plot for the stationary cylinder, Right: Total velocity (U) surface plot for the rotating cylinder ($W = 3.2$ and $R_{f/n} = 5$).

The left half of the figure shows the stationary cylinder at Re 60, and the right half

of the figure shows the flow field at the same flow speed with the cylinder undergoing rotational oscillation. The stabilized wake has the appearance of an unforced wake at a lower Reynolds number. The wake greatly resembles the time-independent velocity field at a Reynolds number less than 47. It should be noted that drag reduction achieved by rotary oscillation does not always result in wake stabilization.

4.8 Phase lock-on

The phenomenon of phase lock-on (also called vortex lock-in, synchronization, or resonance) is observed in the present study. In a certain range of amplitude and frequency of oscillation, the forced motion of the cylinder can take control of the instability mechanism that leads to vortex shedding. The vortex shedding occurs at the same frequency as the oscillation of the cylinder [74]. The control over the vortex shedding frequency occurs above some minimum amplitude. The range of frequencies at which phase lock-on becomes larger at greater amplitudes [74]. This phenomenon has been studied by Li et al. [74], Cheng et al. [26], Fujisawa et al. [46], and Sheils et al. [96] (among others). Phase lock-on is best illustrated in the present study by comparing the infinite flow field past the stationary cylinder with the rotating cylinder at W = 2, $R_{f/n} = 0.5$, as shown in Figure 4.9. In the stationary case, vortices are being shed at the natural Strouhal number St_{nat}, 0.16. In the rotating case, the cylinder is oscillating at a $St_f = 0.08$. The vortex shedding frequency has decreased to half of the original, matching (or locking-on to) the oscillation frequency. For rotational and transverse oscillations, the phenomenon of lock-on occurs only in a limited range centered around $R_{f/n} = 1$, whereas for in-line oscillations, lock-on is exhibited at $R_{f/n} = 2$ [26]. As observed in Section 4.3, C_D increases to a peak value in the region where $R_{f/n}$ is near 1, so the drag force on the cylinder is at or near a

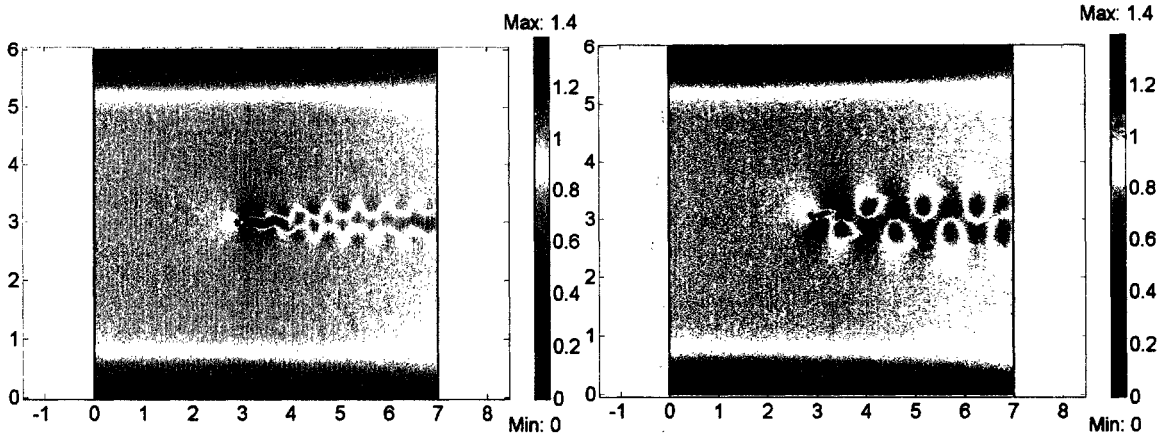

Figure 4.9: Example of vortex lock-on for the infinite fluid problem, Re = 100 - Left: Total velocity (U) surface plot of the stationary cylinder, Right: Total velocity (U) surface plot for the rotating cylinder at W = 2, $R_{f/n} = 0.5$.

maximum when vortex lock-on occurs [26]. Cheng et al. [26] attributes the increase in drag to the fact that the shed vortices gain additional strength from the oscillations.

4.9 Conclusions

It was found that rotational oscillation of the cylinder has a large effect on the drag depending on the rotational parameters in both the benchmark and infinite fluid cases. Furthermore, the behavior of the benchmark problem with open-loop rotation matched the infinite fluid with open-loop rotation phenomenologically. The results of the present work, at a specified amplitude of rotation and varying forcing frequencies, are compared to two other studies at the same amplitude and varying frequencies, but conducted at different Reynolds numbers. The same trends are seen, regardless of Reynolds number. A large spike (increase) in C_D is seen at low forcing frequencies (around $R_{f/n} = 1$), followed by a quick drop off in C_D at increasing frequencies. In the present work, the greatest drag reduction occurs at a forcing ratio $R_{f/n} = 5$. At fixed frequency and varying amplitudes, increasing W (normalized amplitude) at

most frequencies results in larger and larger increases in drag. However, at $R_{f/n} = 5$, larger W results in a larger drag decrease. This increasing drag reduction does have a limit in both the benchmark and infinite fluid cases, however. The maximum drag reduction achieved in both cases is around 14% of the unforced C_D. The open-loop rotation was shown to have a wake stabilizing effect under certain conditions. When the wake is stabilized, it appears to resemble a flow field at a lower Reynolds number. Finally, above a certain amplitude and around a forcing frequency of $R_{f/n} = 1$, the vortex shedding frequency locks-on to the forcing frequency, thereby shifting away from the natural shedding frequency.

Chapter 5

Closed-loop Control

5.1 Introduction

In this chapter, closed-loop control simulations are performed on the benchmark problem. Because of the size of the infinite fluid problem, closed-loop simulations on the infinite fluid are so computationally expensive as to be prohibitive. A proportional controller is tested on the benchmark problem, varying controller gain and measurement sampling time. A PI controller is also tested, varying the integral time. A novel active controller is formulated based on open-loop observations for operation at Reynolds numbers between 50 and 500. This active controller is also tested in the presence of measurement error.

5.2 Proportional controller

A simple proportional (P) controller is first implemented on the system described by the benchmark problem. The controller recorded drag measurements and computed a value for the amplitude of rotation based on the measured drag. Equation 5.1

describes the control law that is used:

$$A = g(C_{D_{avg}} - C_{D_{sp}}) + A_{nom} \tag{5.1}$$

where A is the amplitude of rotation, g is the controller gain, $C_{D_{avg}}$ is the average drag coefficient (defined by Equation 2.18) measured on the surface of the cylinder, $C_{D_{sp}}$ is the desired, or set point, drag coefficient, and A_{nom} is the nominal amplitude of rotation. The frequency of rotation is set at 15 and remained constant for all of the simulations. The speed of the flow through the channel is Reynolds number 100.

As discussed in Chapter 4, at certain frequencies, the drag on the surface of a circular cylinder in a viscous flow field is reduced by increasing the amplitude of rotation of the cylinder. More specifically, it has been observed in open-loop simulations that drag decreases as amplitude increases when a cylinder is forced to oscillate at five times its natural shedding frequency. At Reynolds number 100, the natural shedding frequency, f_{nat}, for the cylinder in the benchmark problem is 3 hz. The forcing frequency of the cylinder at which decreases in drag caused by rotation may be observed is, therefore, around five times this value, 15 hz, which is equivalent to $R_{f/n} = 5$ in non-dimensional terms. This decrease in drag coefficient can be observed at a small range around five times f_{nat} (or St_{nat}). At forcing frequencies above or below this range, the drag increases with increasing amplitude. The goal of the controller is simply to achieve the lowest possible drag by adjusting the amplitude of rotation using only drag measurements.

Several different values of the gain, g, are tested using the control law described in Equation 5.1. Values ranging from 1 to 60 are tested for g. Values used for A_{nom} are 0 and 10. In all cases, $C_{D_{sp}}$ is 2, significantly below the lowest value of C_D achieved with open-loop rotation, which is 2.9435. This value of $C_{D_{sp}}$ is selected as a best case goal for closed-loop control. The actuator is not limited to a specific range of

values by the controller design. However, although the controller-specified actuation could assume any value, the amount of actuation is practically limited by the inherent oscillation of the system.

The effect of all of these combinations of values is essentially the same. None of these controllers reduces the drag on the cylinder below the lowest C_D value achieved with open-loop rotation. Furthermore, the controllers only produces rotation that results in values of the drag coefficient close to the best achieved by open-loop rotation at very high gain. Figure 5.1 shows the effect of changing the value of the gain. In

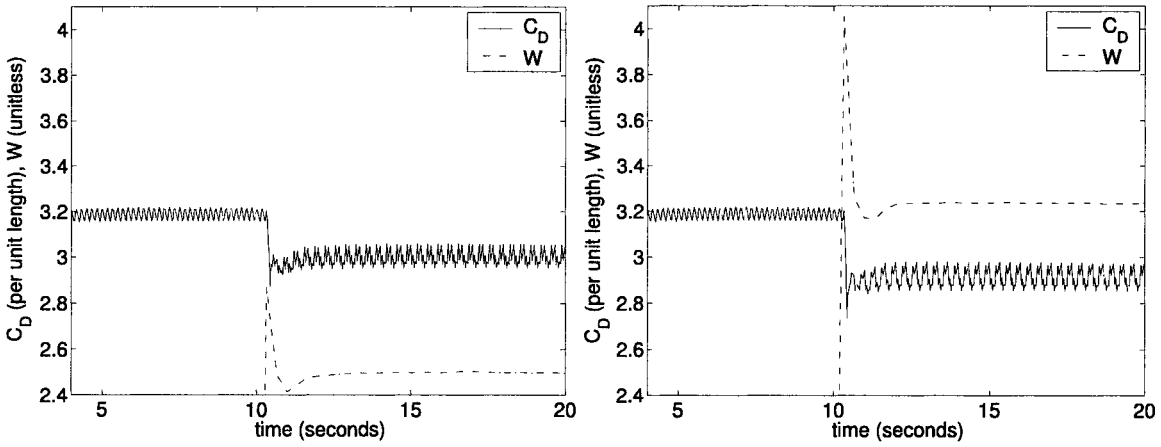

Figure 5.1: Implementation of the P controller showing the effect of changes in gain on C_D, controller turned on at 10 seconds, Re = 100 - Left: gain = 40, Right: gain = 60.

each figure, the solid line is C_D, and the dashed line is W, the normalized amplitude specified by the controller. In both instances, A_{nom} is 10, and the controller is turned on at 10 seconds. As can be seen in both cases, once the controller is turned on, a quick adjustment is made in W and the final value of the drag coefficient is reached with no further changes induced by the controller. The oscillations that occur in other unactuated and open-loop simulations persist in the presence of the controller. In both cases, the amplitude resulting from the controller action is what would be expected from Equation 5.1. In other words, the final value for the amplitude specified

by the controller for each gain value is directly a result of the magnitude of the gain used. The controller does not 'find' the appropriate value of A by making several adjustments. Instead, the controller simply settles on a value of the amplitude that is roughly equal to the gain, g, plus A_{nom}, the nominal amplitude. Once the controller is turned on, it immediately returns this preset value and then oscillates in the same manner as the unactuated and open-loop rotation systems. For the simulation with the gain of 40, the average C_D for the rotating cylinder is 3.01, and the average C_D for the portion of the simulation where the cylinder is rotating with a gain of 60 is 2.92.

The period of rotation is the inverse of the frequency of rotation, T = $\frac{1}{f}$. At Reynolds number 100, T is $\frac{1}{15}$ seconds. In the simulations using the proportional controller, the value of C_D is sampled and averaged over five periods of rotation, or $\frac{1}{3}$ seconds. After this average is calculated, the value of A is computed using the Equation 5.1. One possible explanation for the controller's poor performance is that the period of sampling C_D is too long. If this was the case, this would mean that the controller was not able to provide values of A in time to affect the system in the appropriate way to successfully lower the drag to the desired level. To ensure that the controller is reacting quickly enough to have an opportunity to lower the drag, the controller is simulated with a sampling time of $\frac{1}{15}$ seconds. The results are shown in Figure 5.2. The solid line is C_D, and the dashed line is W, the normalized amplitude. The gain is 60 and A_{nom} is 10. The controller is turned on at 5 seconds. When compared to the profile shown on the right side of Figure 5.1, which is run under the same condition except with a sampling period of $\frac{1}{3}$ seconds, it is evident that there is very little difference between the two. Both have the same average final drag. The simulation with the shorter sampling period in Figure 5.2 shows that C_D

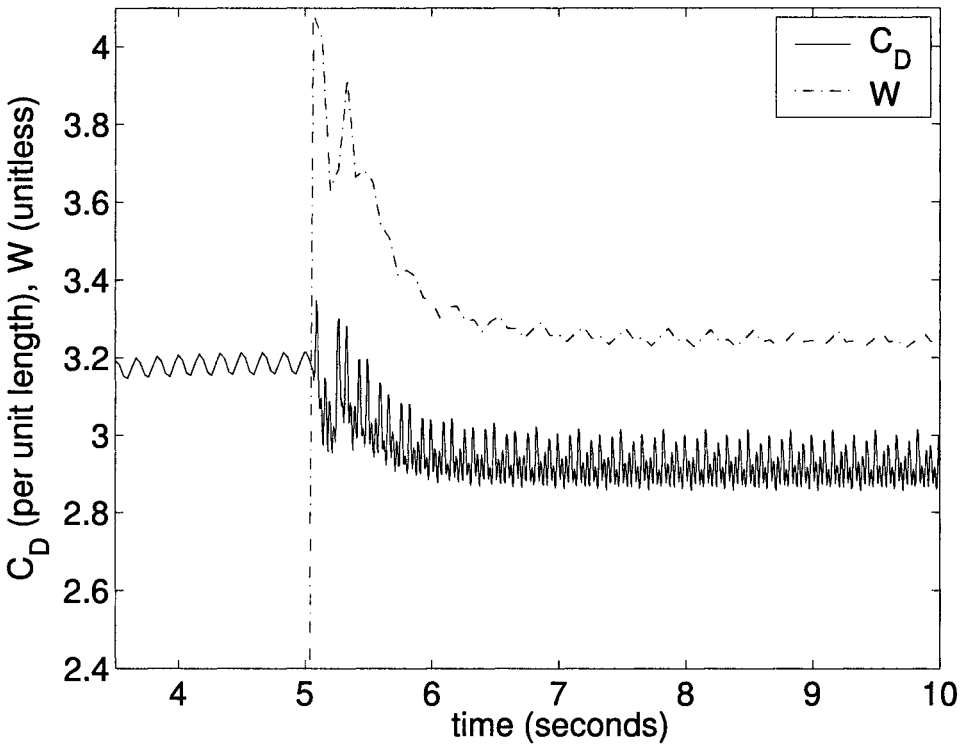

Figure 5.2: Effect of smaller sampling period ($\frac{1}{15}$ sec) for C_D on the efficacy of the P controller, gain = 60, $A_{nom} = 10$, Re = 100.

exhibits a more gradual, less abrupt transition from the unactuated to the closed-loop drag coefficient value. Similarly, the dashed line in Figure 5.2 indicates that W, as specified by the controller, changes more gradually than the controller with the longer sampling time shown in Figure 5.1.

Regardless of sampling time used, the proportional controller is not effective at reducing the drag on the cylinder using rotational oscillation actuation. The oscillations in the drag inherent in the system at this Reynolds number dominate the system, preventing the proportional controller from being effective. Based on drag measurements of open-loop actuation shown in Chapter 4, the addition of the proportional controller does not destabilize the drag, but the controller does not improve the drag relative to open-loop actuation either.

5.3 Proportional integral controller

A proportional integral (PI) controller is also tested on the system described by the benchmark problem. Similar to the proportional controller described by Equation 5.1, the control law for the PI controller is given in Equation 5.2:

$$A = g\left((C_{D_{avg}} - C_{D_{sp}}) + \frac{1}{\tau}\int (C_{D_{avg}} - C_{D_{sp}})dt\right) + A_{nom} \qquad (5.2)$$

All the terms in Equation 5.2 have the same meaning as in Equation 5.1, and τ is the integral or reset time. As with the P controller, the actuator is not limited to a specific range of values by the PI controller design. However, although the controller-specified actuation could assume any value, the amount of actuation is practically limited by the inherent oscillation of the system.

Like the P controller, the PI controller is not successful in suppressing the oscillations. Given that the introduction of an integral time parameter can yield oscillatory

behavior in non-oscillating systems, it is to be expected that the oscillations of the circular cylinder wake would persist with PI control. However, the PI controller is not able to reduce the overall drag below the level of the open-loop rotation, either. Figure 5.3 shows a typical drag profile resulting from the application of PI control. The solid line is C_D, and the dashed line is W, the value of the normalized amplitude

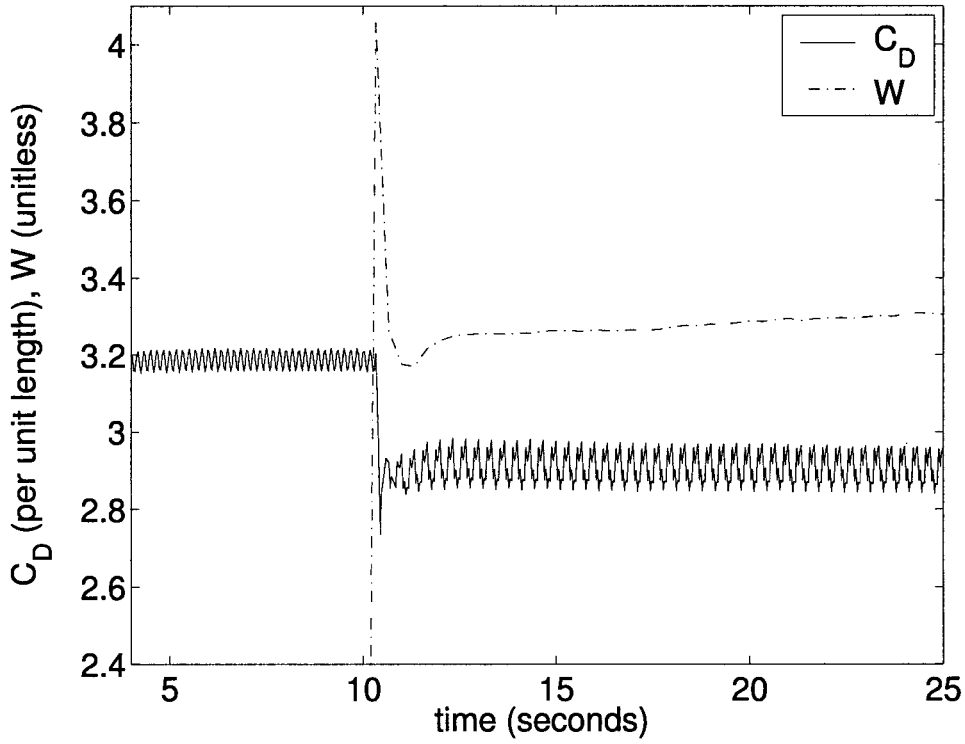

Figure 5.3: Implementation of the PI controller and its effect on C_D, gain = 60, A_{nom} = 10, $\tau = 20$.

specified by the controller. In this simulation, the controller is turned on at 10 seconds. The gain is 60, A_{nom} is 10, and τ is 20. As in the case of the P controller, the drag coefficient changes quickly and then oscillates around a value that is less than the unactuated drag. The final average value of C_D, 2.91, is essentially the same as the proportional controller with the same parameters.

The presence of the integral action either drove the cylinder to rotate such that

drag coefficient either oscillated out of control or did not change significantly compared with the open loop rotation. This is best illustrated in Figure 5.4. In both cases, the gain is 60 and A_{nom} is 10. The solid line is C_D, and the dashed line is

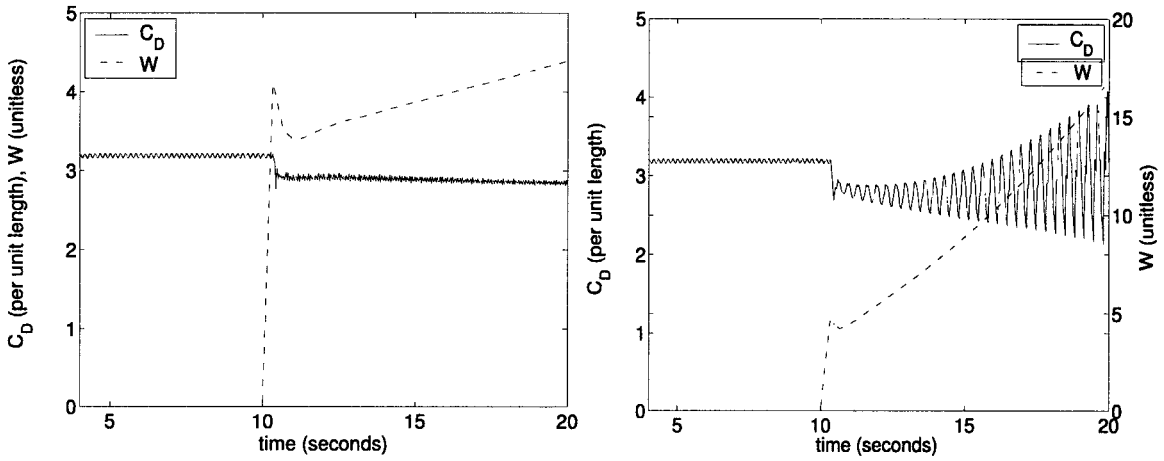

Figure 5.4: Demonstration of the PI controller driving the system to an unstable state - Left: $\tau = 1$, Right: $\tau = 0.1$.

W, the value of the normalized amplitude specified by the controller. In these simulations, the controller is turned on at 10 seconds. In the left figure, the integral time, τ, is 1. In the right figure, τ is 0.1. In the right figure, W has very large values, and, therefore, is plotted on a separate y axis. The PI controller with τ set at 0.1 drives the amplitude out of control, leading to unstable oscillation of C_D. The difference between the values of τ in Figure 5.4 is very small. The case where τ is 1 exhibits a very small reduction of C_D over time. This controller shows only a very slight improvement (less than 2%) in the overall reduction of C_D compared to the P controller with the same specifications (or, therefore, the reduction of C_D achieved with open-loop rotation with the same parameters). Yet, a small decrease in τ drives the cylinder to rotate such that the drag coefficient oscillates out of control. The PI controller is not able to control the circular cylinder wake better than open-loop

actuation.

The reason that both the proportional and the proportional integral controller failed is that the oscillations inherent in the unactuated system tend to dominate the control action dictated by the controller. After the initial action taken by the controllers, the oscillation of the system prevents both controllers from making further significant adjustments in the amplitude of rotation of the cylinder. Essentially, the controller is manipulated by the oscillations of the drag force. It should be emphasized that the final value of the amplitude, A, specified by the controllers is less than the A_{max} the amplitude which results in the maximum reduction of C_D at the given rotation frequency, $R_{f/n} = 5$. Based on drag measurements of open-loop actuation shown in Chapter 4, the addition of the proportional controller and the proportional integral controller do not destabilize the drag, but the controllers do not improve the drag relative to open-loop actuation either.

5.4 Active controller

The present study, among others [78,89,96,109], has shown that a cylinder oscillating at five times St_{nat} exhibits a reduction in C_D compared to a stationary cylinder. As shown above, the P and the PI controller are not successful at reducing C_D around the circular cylinder more than open-loop rotation. An alternative kind of control is, therefore, simulated which takes data from stationary cylinder simulations at varying Reynolds numbers. A schematic diagram for this control methodology is shown in Figure 5.5.

As discussed in Section 3.4 and shown in Figure 3.6, a distinct linear relationship exists between the natural frequency of vortex shedding, f_{nat}, and the Reynolds number of the flow field, Re, for the cylinder in the range of Reynolds numbers between

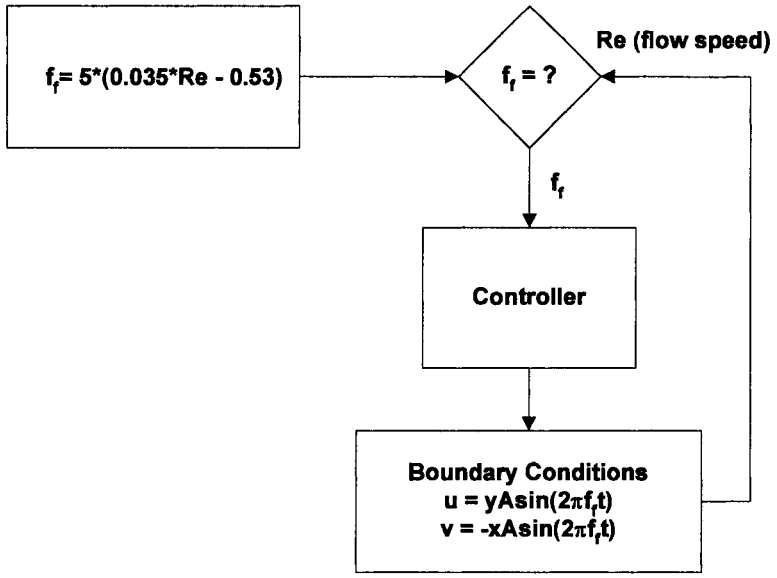

Figure 5.5: Diagram of active controller methodology.

50 and 500. Using this linear relationship, St_f ($= \frac{f_f\, d}{U_{mean}} = 5St_{nat}$) is determined for each of five Reynolds numbers: 100, 150, 200, 250, and 500. A controller is designed that can detect the speed of the oncoming flow field and change the oscillation frequency of the cylinder, f_f, based on the linear relationship shown in Figure 3.6 as the Reynolds number changes to maintain a reduction in C_D. This control methodology can also be considered to be a type of feedforward control.

Figure 5.6 shows the profile of C_D versus time when speed of the flow field is changing from Reynolds number 100 to 500 and the cylinder is stationary. In the stationary simulation, the flow field passes the unactuated cylinder first at Reynolds number 100. Then, at the time denoted by the first vertical line in Figure 5.6, the flow instantaneously changes to Reynolds number 150. The flow field remains at Reynolds number 150 until it changes instantaneously to Reynolds number 200, denoted by the second vertical line in Figure 5.6. In this fashion, the flow varied from Reynolds number 100 to 500.

The values of St_f for each Reynolds number that are specified by the controller

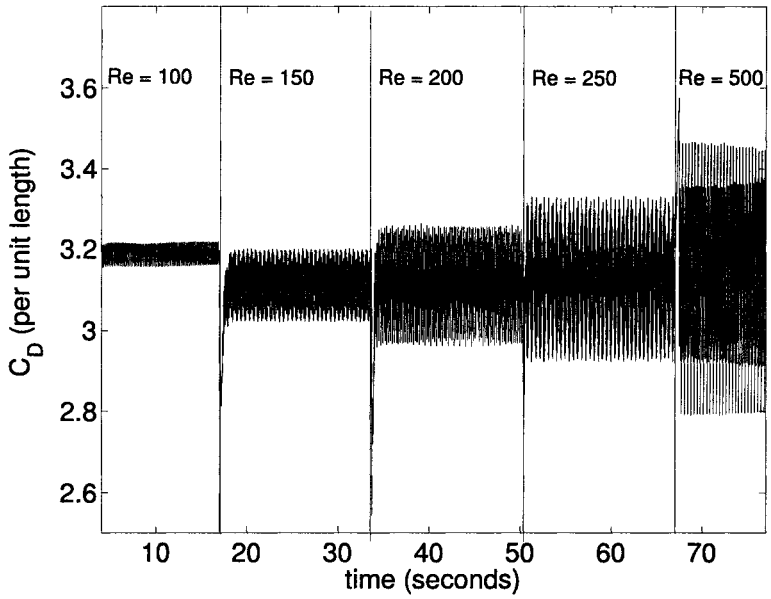

Figure 5.6: C_D vs. time at varying Reynolds numbers under open-loop conditions (no actuation).

are given in Table 5.1. In the simulation incorporating this controller, the speed of

Table 5.1: St_f at different Reynolds numbers.

Re	Period, T_{nat}	f_{nat}	f_f	St_{nat}	St_f
100	0.333	3	15	0.300	1.50
150	0.215	4.6512	23.256	0.310	1.55
200	0.160	6.25	31.25	0.3125	1.5625
250	0.125	8	40	0.32	1.6
500	0.058	17.153	85.763	0.3431	1.7153

the flow field is increased from Reynolds number 100 to 500, as in the stationary cylinder simulation described above and depicted by Figure 5.6. At each Reynolds number, the cylinder rotated at the given frequency for the first half of the time, and then is stationary for the remaining time. The controller sensed the speed of the flow field and changed f_f accordingly. Figure 5.7 shows the drag profile resulting

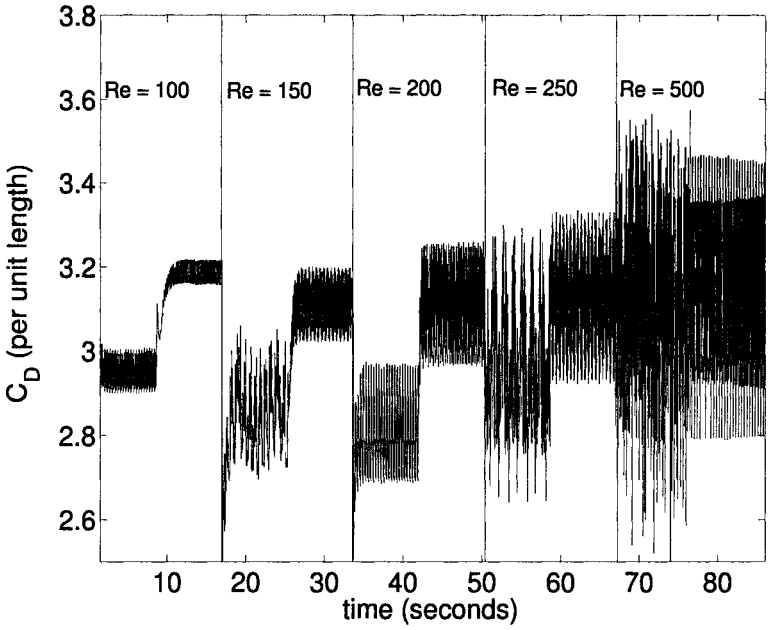

Figure 5.7: Closed-loop control: C_D vs. time for Reynolds number varying from 100 to 500. The controller is initially on at the beginning of each interval, then turned off at the middle of each interval. The Reynolds number is instantaneously changed from one interval to the next.

from the application of this controller. As shown, the controller reduces the drag on the cylinder at every Reynolds number. When the controller is turned off, the drag increases. Comparing Figures 5.7 and 5.6 shows that the drag coefficient in the actuated system returns to same unforced values when the cylinder stops rotating as when there is no actuation of the cylinder at any time.

A second series of closed-loop simulations are completed to evaluate the performance of the controller. Specifically, the Reynolds number is increased from 100 to 500 again, this time with gradual increases in the Reynolds number instead of instantaneous increases. Figure 5.8 shows the values of C_D vs. time for two different cases:

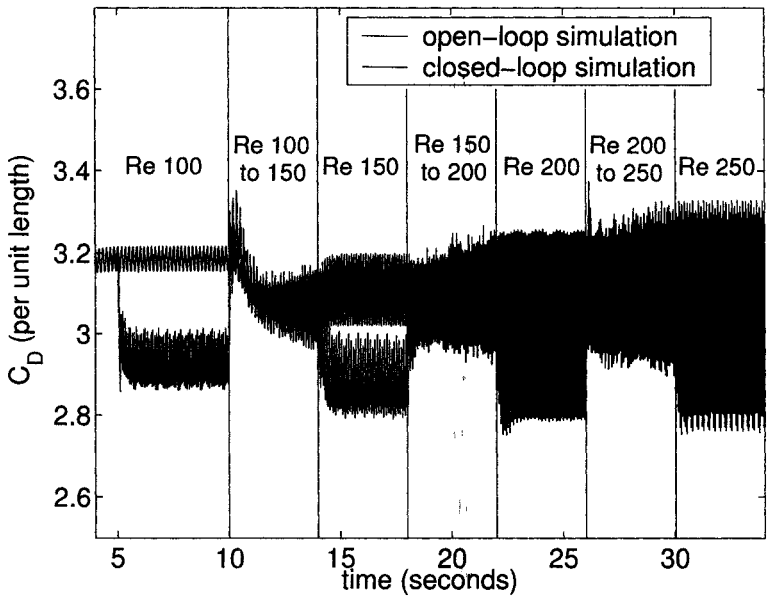

Figure 5.8: Closed-loop control: C_D vs. time for Reynolds number varying from 100 to 250 under open-loop (blue line) and closed-loop (black line) conditions.

one open-loop simulation and one closed-loop simulation. Figure 5.8 shows only the change from Reynolds number 100 to 250 in each case. Initially, in both cases, the Reynolds number is 100. After 10 seconds, the Reynolds number is gradually increased (over a period of four seconds) from 100 to 150. This is accomplished by raising the average flow speed at the inlet boundary, U_{mean}. After the flow is brought

to Reynolds number 150, it is held there for another four seconds. In this manner, the Reynolds number is raised over four seconds and successively held for four seconds at 200, 250, and 500. In this closed-loop simulation, the controller is turned on at five seconds at Reynolds number 100. Using the linear relationship given in Figure 3.6, the frequency of oscillation is determined by measuring the Reynolds number every 0.01 seconds and altering the frequency of rotation at the cylinder boundary accordingly. During the periods where the Reynolds number is gradually increased, the frequency of oscillation is also gradually increased, as the controller takes Reynolds number readings every 0.01 seconds and adjusts the frequency of rotation based on its measurements.

One way to evaluate the performance of the active controller is to compare the effect of each of the five frequencies used in the active controller at all five of the Reynolds numbers that are considered. Table 5.2 shows the percent reduction of C_D at each combination of frequency and Reynolds number. The boldface values on the

Table 5.2: Percent reduction of C_D by rotating cylinder at given f_f and Re.

	forcing frequency, f_f				
Re	15	23.256	31.25	40	85
100	**7.49**	-2.08	-5.32	-4.01	0.00
150	16.32	**8.78**	6.21	2.82	0.18
200	16.35	11.14	**6.14**	7.63	0.45
250	10.37	0.45	7.31	**5.04**	0.85
500	-12.04	3.35	-1.90	1.97	**1.15**

diagonal of the table are the percent reduction of C_D achieved by the active controller. In most cases, the reductions of C_D resulting from the frequencies specified by the controller are above average compared to the other frequencies tested. A no-

table exception occurs at $f_f = 15$, at which the values of C_D are lower than those yielded by most of the other frequencies. However, at Reynolds number 500, $f_f = 15$, which is very effective at reducing drag at other speeds, causes a large increase in drag. This result emphasizes the fact that the controller is not an optimal one, which would produce the greatest possible reduction in drag under all conditions. The active controller is intended only to produce a consistent drag reduction at changing flow speeds. Figure 5.9 shows the resulting values of C_D for the combinations of Reynolds

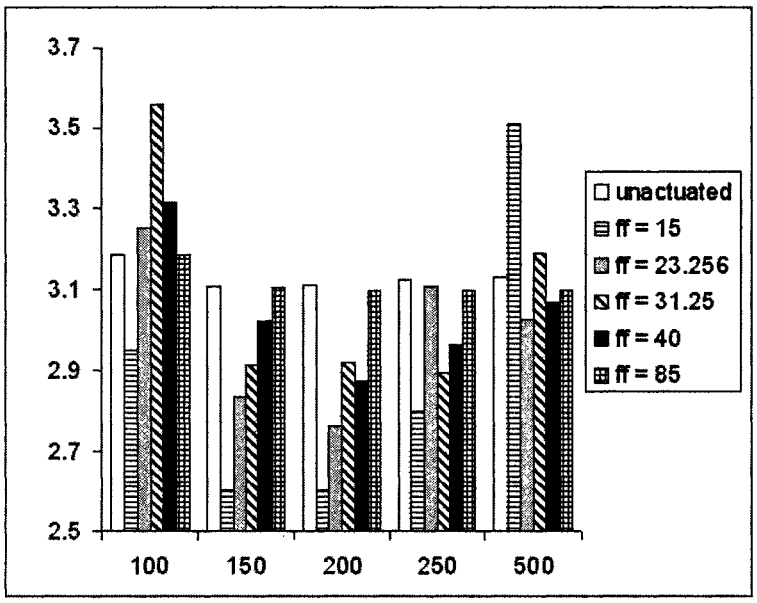

Figure 5.9: C_D values from the closed-loop simulation shown in Figure 5.7 at various combinations of f_f and Reynolds number.

number and forcing frequency given in Table 5.2. Because of the large amount of oscillation in C_D that is present in some of the combinations of frequency and Reynolds number, it is difficult in some cases to determine the mean drag by inspection of the drag profiles. For this reason, in Figure 5.9, the mean drag values have been substituted for the time-varying drag profiles that have been shown previously for other simulations.

It should be noted that the claim of the effectiveness of this controller only extends to Reynolds number 500. Observations at Reynolds numbers greater than 500 have not been made in the study, so it is not known whether or not the controller would be effective outside the observed range of Reynolds numbers.

The performance of the controller in the presence of measurement errors was also evaluated. The simulation described above, where the Reynolds number is increased from 100 to 500 (holding the Reynolds number constant at each intermediate Reynolds number for four seconds) is repeated in the presence of measurement errors.

Two cases with measurement errors are simulated. The first case corresponds to underestimation of the sensed flow speed. Specifically, the controller uses 80% of the actual Reynolds number value to determine the forcing frequency. For example, when the flow field is at Reynolds number 100, the controller uses a reading of Reynolds number 80 (instead of the real value of 100), and it then adjusts the frequency of rotation as if the Reynolds number is actually 80. This -20% error is maintained throughout the simulation so that, at every Reynolds number, the controller uses a Reynolds number that is 20% less than the actual. As can be seen in Figure 5.10, even with the presence of the measurement error, the controller is successful at reducing the drag compared to the open-loop case.

The second case with measurement error corresponds to the overestimation of the sensed flow speed. In this case, the controller uses 120% of the actual Reynolds number value to determine the forcing frequency. Reynolds number 120 is used by the controller when the actual Reynolds number is 100. This is a $+20\%$ error, and is maintained throughout the simulation so that, at every Reynolds number, the controller uses a Reynolds number that is 20% more than the actual. Figure 5.11 shows the performance of the controller in the presence of this error. As with Figure 5.10,

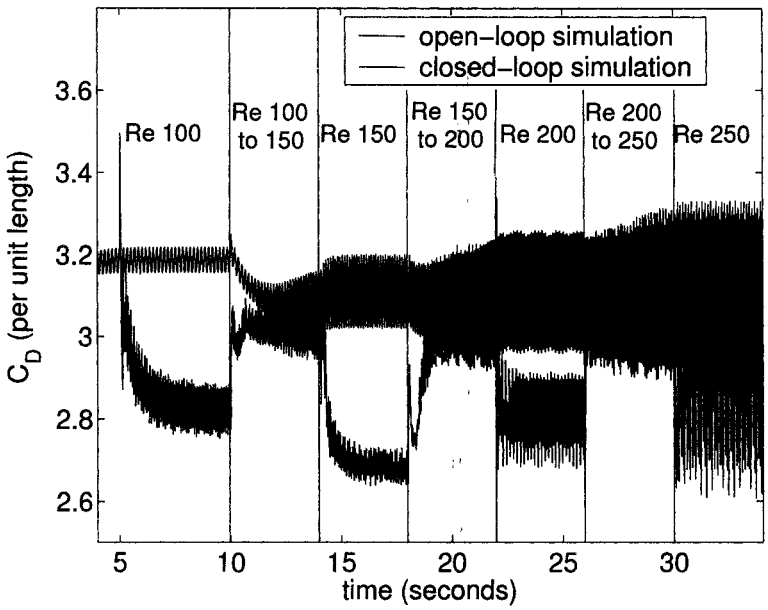

Figure 5.10: Closed-loop simulation in the presence of measurement errors: C_D vs. time for Reynolds number varying from 100 to 250 under open-loop conditions (blue line) and under closed-loop conditions in the presence of -20% measurement error (black line).

Figure 5.11 shows that the controller exhibits very good robustness with respect to measurement error, reducing the drag compared to the open-loop case. This controller is robust, as shown by Figure 5.10 and Figure 5.11, because a consistent drag reduction can be obtained with rotation within a range of frequencies around $5f_{nat}$, as shown in Chapter 4. Because of this range, if there is some limited amount of error in sensing the flow speed resulting in a flow speed reading that is close to the actual, the frequency returned by the controller will still be able to reduce the drag. Naturally, if there is a large error in sensing the flow speed, the frequency determined by the controller will not be effective at reducing the drag.

The novel active controller senses the speed of the flow field and determines appropriate oscillation parameters based on the Reynolds number of the flow. This controller is successful at actuating the cylinder at various flow speeds. When the cylinder oscillates with the parameters specified by the controller, the drag coefficient

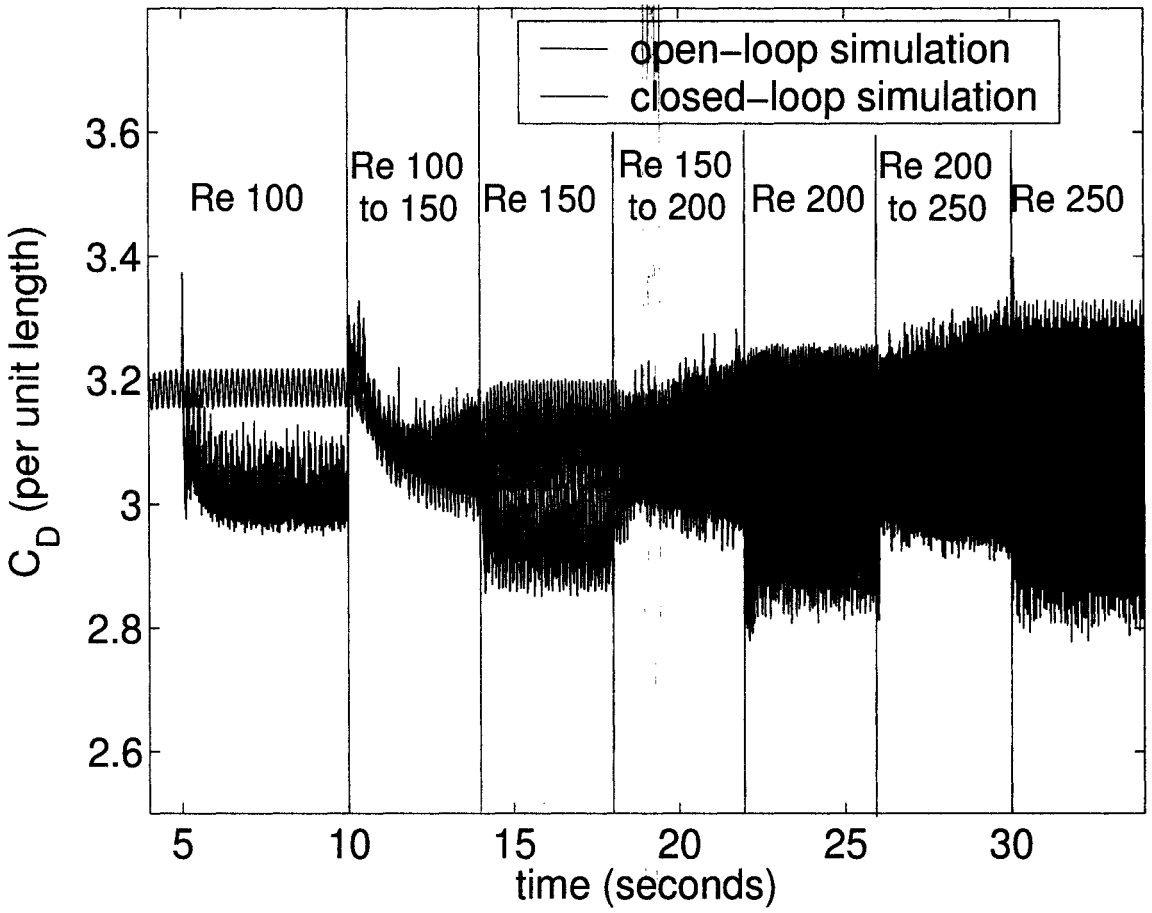

Figure 5.11: Closed-loop simulation in the presence of measurement errors: C_D vs time for Reynolds number varying from 100 to 250 under open-loop conditions (blue line) and under closed-loop conditions in the presence of +20% measurement error (black line).

at each Reynolds number is less than the stationary drag coefficient.

5.5 Conclusions

In closed-loop simulations, it was found that neither a P nor a PI controller showed any improvement over open-loop actuation in reduction of drag over a circular cylinder in the case of the benchmark problem. Varying gain and measurement sampling time in the case of P controller and integral time in the case of the PI controller did not result in significant reductions in drag compared to the open-loop rotation. Based on open-loop observations, a novel active controller was designed that measures incoming flow speed and adjusts the frequency of rotation. This controller was found to yield consistent, although not optimal, drag reductions from Reynolds numbers 50 to 500. Finally, the controller was also tested in the presence of 20% measurement error, and found to still yield consistent drag reduction.

Chapter 6

Proper Orthogonal Decomposition and Galerkin Projection

6.1 Introduction

In this chapter, Proper Orthogonal Decomposition (POD) and the Galerkin Projection of the Navier-Stokes equations are discussed. Initially, the geometry and discretization of the cylinder flow problem used for obtaining the POD modes is illustrated. A general discussion of the method for computing empirical eigenfunctions with POD is then given. The specific application of the Proper Orthogonal Decomposition method to flow past the cylinder is next. After this, the chapter is concluded with a demonstration of how the Galerkin Projection of the Navier-Stokes equations uses the empirical eigenfunctions generated by POD to produce a reduced-order model of the flow.

6.2 Geometry

In order to apply the Proper Orthogonal Decomposition (POD) Method and perform the Galerkin Projection of the two-dimensional, incompressible Navier-Stokes equations, a different flow field is used. This alternate flow field is also an essentially unbounded flow field, as shown in Figure 2.2. The alternate flow field geometry is the same as that in a study by Siegel et al. [98] for the United States Air Force Academy. A schematic of the flow field and its relative dimensions are shown in Figure 6.1. The

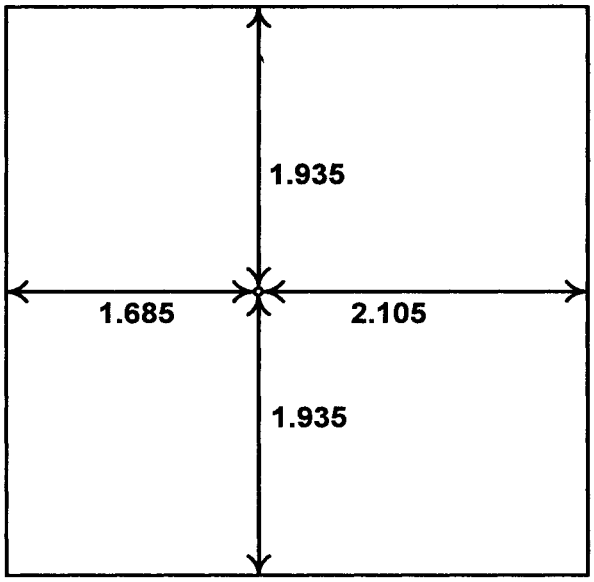

Figure 6.1: Schematic of the flow field, dimensions in cylinder diameters.

cylinder diameter is 0.1. As shown in Figure 6.1, the lateral channel boundary width to cylinder diameter ratio in this study is 39.7, and the channel length to cylinder ratio is 38.8. These dimensions are much larger than five cylinder diameters, which is specified by Li et al. [73] for an unbounded fluid. The boundaries of the flow field are, therefore, far enough away so that they do not influence the drag force on the cylinder.

The two-dimensional, incompressible Navier-Stokes equations given in Chapter 2,

Equation 2.2 apply to this system. The same boundary conditions given in Equations 2.3, 2.4, and the 30^{th} order polynomial given in Section 2.2 apply to this flow field as well. The stationary cylinder has the same no-slip, no penetration boundary conditions given previously.

6.3 Discretization

These simulations are again solved within the $FEMLAB^{TM}$ simulation environment Two different mesh structures are used. The exact form of the spatial discretization mesh for each case is shown in Figure 6.2. The most dynamic region in the flow field

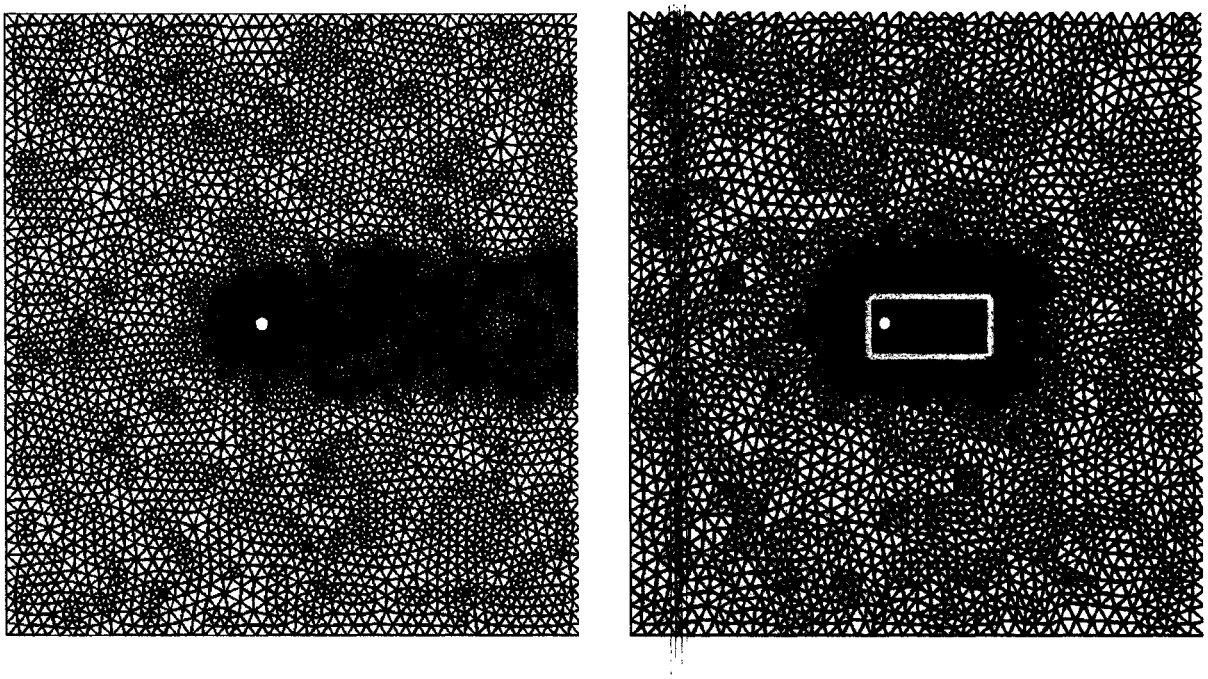

Figure 6.2: Finite element mesh used - Left: entire flow field used to calculate POD modes, Right: subset of flow field used to calculate POD modes.

is around and directly behind the cylinder. Because the largest velocity gradients are present in these regions, the mesh is very refined around the cylinder edges. To reduce the computational load of this demanding problem, the mesh is less refined further away from the cylinder, where less change is taking place over time. The fine

resolution around the cylinder in each case is necessary for accurate measurement of drag.

In the case of the flow field with only one domain, shown on the left half of Figure 6.2, the domain has a total of 7360 nodes, 320 edges, and 14400 elements. The problem is also solved with a simulation with two separate computational domains, modeled after work done by the United States Air Force Academy [98]. For the flow field with two domains, shown on the right half of Figure 6.2, the smaller yellow rectangle, immediately outside the cylinder is the interior domain. The whole domain has 6158 nodes, 390 edges, and 12032 elements, while the interior domain has 2675 nodes, 234 edges, and 5116 elements. Siegel et al. [98] use the whole domain to compute the flow field, but use only the interior domain to calculate the POD modes. This study also solves the flow field with the whole domain and uses the interior domain to compute the POD modes in the cases where the two domain mesh structure is employed.

6.4 Computation of empirical eigenfunctions via Proper Orthogonal Decomposition

The method of Proper Orthogonal Decomposition, also known as Karhunen-Loéve expansion (or K-L expansion), is reviewed in the context of nonlinear one-dimensional parabolic PDE systems of the following form:

$$\begin{aligned} \frac{\partial \bar{x}}{\partial t} &= L(\bar{x}) + wb(z)u + f(\bar{x}) \\ y^i &= \int_\alpha^\beta c^i(z) k\bar{x} dz, \quad i = 1, \ldots, l \end{aligned} \tag{6.1}$$

subject to the boundary conditions:

$$C_1\bar{x}(\alpha, t) + D_1\frac{\partial \bar{x}}{\partial z}(\alpha, t) = R_1, \;\; C_2\bar{x}(\beta, t) + D_2\frac{\partial \bar{x}}{\partial z}(\beta, t) = R_2 \tag{6.2}$$

and the initial condition:

$$\bar{x}(z,0) \;=\; \bar{x}_0(z) \tag{6.3}$$

where $\bar{x}(z,t) = [\bar{x}_1(z,t) \;\cdots\; \bar{x}_n(z,t)]^T$ denotes the vector of state variables, $z \in [\alpha,\beta] \subset \mathbb{R}$ is the spatial coordinate, $t \in [0,\infty)$ is the time, $u = [u^1\; u^2 \;\cdots\; u^l]^T \in \mathbb{R}^l$ denotes the vector of manipulated inputs, and $y^i \in \mathbb{R}$ denotes the i-th controlled output. $L(\bar{x})$ is a nonlinear differential operator which involves first- and second-order spatial derivatives, $f(\bar{x})$ is a nonlinear vector function, w, k are constant vectors, C_1, D_1, C_2, D_2 are constant matrices, R_1, R_2 are column vectors, and $\bar{x}_0(z)$ is the initial condition. $b(z)$ is a known smooth vector function of z of the form $b(z) = [b^1(z)\; b^2(z) \;\cdots\; b^l(z)]$, where $b^i(z)$ describes how the control action $u^i(t)$ is distributed in the interval $[\alpha,\beta]$, and $c^i(z)$ is a known smooth function of z which is determined by the desired performance specifications in the interval $[\alpha,\beta]$. Whenever the control action enters the system at a single point z_0, with $z_0 \in [\alpha,\beta]$ (i.e., point actuation), the function $b^i(z)$ is taken to be nonzero in a finite spatial interval of the form $[z_0-\epsilon, z_0+\epsilon]$, where ϵ is a small positive real number, and zero elsewhere in $[\alpha,\beta]$.

See [47, 60] for a general presentation and analysis of the K-L expansion. We assume that the solution of the system of Equation 6.1 is known and consider a sufficiently large set (which is called an ensemble), $\{\bar{v}_\kappa\}$, consisting of N sampled states, $\bar{v}_\kappa(z)$, (which are typically called "snapshots") of the solution of Equation 6.1. To simplify our presentation, we assume uniform-in-time sampling of, $\bar{v}_\kappa(z)$, (i.e., the time interval between any two successive sampled states is the same), while we define the ensemble average of snapshots as $< \bar{v}_\kappa >:= \dfrac{1}{K}\sum_{n=1}^{K}\bar{v}_n(z)$ (we note that non-uniform sampling of the snapshots and weighted ensemble average can be also considered; see, for example, [54]). Furthermore, the ensemble average of snapshots

$< \bar{v}_\kappa >$ is subtracted out from the snapshots i.e.,:

$$v_\kappa = \bar{v}_\kappa - < \bar{v}_\kappa > \tag{6.4}$$

so that only fluctuations are analyzed. The issue is how to obtain the most typical or characteristic structure $\phi(z)$ among these snapshots $\{v_\kappa\}$. Mathematically, this problem can be posed as the one of obtaining a function $\phi(z)$ that maximizes the following objective function:

$$\begin{aligned} &\text{Maximize } \frac{< (\phi, v_\kappa)^2 >}{(\phi, \phi)} \\ &s.t.\ (\phi, \phi) = 1, \quad \phi \in L^2([\alpha, \beta]) \end{aligned} \tag{6.5}$$

The constraint $(\phi, \phi) = 1$ is imposed to ensure that the function, $\phi(z)$, computed as a solution of the above maximization problem, is unique. The Lagrangian functional corresponding to this constrained optimization problem is:

$$\bar{L} = < (\phi, v_\kappa)^2 > -\lambda((\phi, \phi) - 1) \tag{6.6}$$

and necessary conditions for extrema is that the functional derivative vanishes for all variations $\phi + \delta\psi \in L^2[\alpha, \beta]$, where δ is a real number:

$$\frac{d\bar{L}(\phi + \delta\psi)}{d\delta}(\delta = 0) = 0, \ (\phi, \phi) = 1 \tag{6.7}$$

Using the definitions of inner product and ensemble average, $\frac{d\bar{L}(\phi + \delta\psi)}{d\delta}(\delta = 0)$ can be computed as follows:

$$\begin{aligned} \frac{d\bar{L}(\phi + \delta\psi)}{d\delta}(\delta = 0) &= \frac{d}{d\delta}\left[< (v_\kappa, \phi + \delta\psi)(\phi + \delta\psi, v_\kappa) > -\lambda(\phi + \delta\psi, \phi + \delta\psi)\right]_{\delta=0} \\ &= 2Re\left[< (v_\kappa, \psi)(\phi, v_\kappa) > -\lambda(\phi, \psi)\right] \\ &= \left\langle \int_\alpha^\beta \psi(z) v_\kappa(z) dz \int_\alpha^\beta \phi(\bar{z}) v_\kappa(\bar{z}) d\bar{z} \right\rangle - \lambda \int_\alpha^\beta \phi(\bar{z})\psi(\bar{z}) d\bar{z} \\ &= \int_\alpha^\beta \left(\left\{ \int_\alpha^\beta < v_\kappa(z) v_\kappa(\bar{z}) > \phi(z) dz \right\} - \lambda\phi(\bar{z}) \right) \psi(\bar{z}) d\bar{z} \end{aligned} \tag{6.8}$$

Since $\psi(\bar{z})$ is an arbitrary function, the necessary conditions for optimality take the form:

$$\int_{\alpha}^{\beta} < v_{\kappa}(z)v_{\kappa}(\bar{z}) > \phi(z)dz = \lambda\phi(\bar{z}), \quad (\phi, \phi) = 1 \tag{6.9}$$

Introducing the two-point correlation function:

$$K(z, \bar{z}) =< v_{\kappa}(z)v_{\kappa}(\bar{z}) >= \frac{1}{K}\sum_{\kappa=1}^{K} v_{\kappa}(z)v_{\kappa}(\bar{z}) \tag{6.10}$$

and the linear operator:

$$R := \int_{\alpha}^{\beta} K(z, \bar{z})d\bar{z} \tag{6.11}$$

the optimality condition of Equation 6.9 reduces to the following eigenvalue problem of the integral equation:

$$R\phi = \lambda\phi \Longrightarrow \int_{\alpha}^{\beta} K(z, \bar{z})\phi(\bar{z})d\bar{z} = \lambda\phi(z) \tag{6.12}$$

The computation of the solution of the above integral eigenvalue problem is, in general, a very expensive computational task. To circumvent this problem, Sirovich introduced in 1987 [100, 101] the method of snapshots. The central idea of this technique is to assume that the requisite eigenfunction, $\phi(z)$, can be expressed as a linear combination of the snapshots i.e.,:

$$\phi(z) = \sum_{k} c_k v_k(z) \tag{6.13}$$

Substituting the above expression for $\phi(z)$ in Equation 6.12, we obtain the following eigenvalue problem:

$$\int_{\alpha}^{\beta} \frac{1}{K}\sum_{\kappa=1}^{K} v_{\kappa}(z)v_{\kappa}(\bar{z})\sum_{k=1}^{K} c_k v_k(\bar{z})d\bar{z} = \lambda\sum_{k=1}^{K} c_k v_k(z) \tag{6.14}$$

Defining:

$$B^{\kappa k} := \frac{1}{K}\int_{\alpha}^{\beta} v_{\kappa}(\bar{z})v_k(\bar{z})d\bar{z} \tag{6.15}$$

the eigenvalue problem of Equation 6.14 can be equivalently written as:

$$Bc = \lambda c \tag{6.16}$$

The solution of the above eigenvalue problem (which can be obtained by utilizing standard methods from matrix theory) yields the eigenvectors $c = [c_1 \cdots c_K]$ which can be used in Equation 6.13 to construct the eigenfunction $\phi(z)$. From the structure of the matrix B, it follows that B is symmetric and positive semi-definite, and thus, its eigenvalues, λ_κ, $\kappa = 1, \ldots, K$, are real and non-negative. Furthermore,

$$\int_\alpha^\beta \phi_\kappa(z)\phi_k(z)dz = 0, \quad \kappa \neq k \tag{6.17}$$

The optimality of the empirical eigenfunctions obtained via K-L expansion can be shown as follows. Consider a snapshot $v_\kappa(z)$ of the ensemble of snapshots, v_κ, and the set of empirical eigenfunctions obtained by applying K-L expansion to v_κ, and let:

$$v_\kappa(z) = \sum_{l=1}^{L} \gamma_l \phi_l(z) \tag{6.18}$$

be the decomposition of $v_\kappa(z)$ with respect to this basis. Assume that the eigenfunctions have been ordered so the corresponding eigenvalues satisfy $\lambda_1 > \lambda_2 > \cdots > \lambda_{l+1}$. Then, it can be shown [60] that if $\{\psi_1, \psi_2, \ldots, \psi_\kappa\}$ is some arbitrary set of orthonormal basis functions in which we expand $v_\kappa(z)$, then the following result holds for any L:

$$\sum_{l=1}^{L} < (\phi_l, v_\kappa)^2 > = \sum_{l=1}^{L} \lambda_l \geq \sum_{l=1}^{L} < (\psi_l, v_\kappa)^2 > \tag{6.19}$$

This implies that the projection on the subspace spanned by the empirical eigenfunctions will on average contain the most energy possible compared to all other linear decompositions, for any number of modes L.

6.5 Application of Proper Orthogonal Decomposition

The POD method is performed to find a set of ordered orthonormal basis vectors in a subspace (without loss of generality) [75]. The Navier - Stokes equations provides an infinite-dimensional solution to the distributed parameter system of flow past the circular cylinder. The Proper Orthogonal Decomposition provides a low-dimensional solution to this system with the use of orthogonal empirical spatial eigenfunctions (also known as modes) and time-varying modal amplitudes (coefficients) [52]. In this study, the velocity field is approximated with two different representations, as shown by the following:

$$\begin{aligned} u(x,y,t) &\approx \sum_{i=1}^{N} a_i(t)\Phi^i(x,y) \\ v(x,y,t) &\approx \sum_{i=1}^{N} b_i(t)\Psi^i(x,y) \end{aligned} \tag{6.20}$$

$$\begin{aligned} u(x,y,t) &= \overline{u(x,y)} + u'(x,y,t) \approx \overline{u(x,y)} + \sum_{i=1}^{N} a_i(t)\Phi^i(x,y) \\ v(x,y,t) &= \overline{v(x,y)} + v'(x,y,t) \approx \overline{v(x,y)} + \sum_{i=1}^{N} b_i(t)\Psi^i(x,y) \end{aligned} \tag{6.21}$$

where the terms in Equation 6.20 and Equation 6.21 are defined in Table 6.5. Data

Table 6.1: Explanation of terms found in Equation 6.20 and Equation 6.21

Total Velocity Component	$u(x,y,t)$	$v(x,y,t)$
Modal Amplitude	$a_i(t)$	$b_i((t)$
Empirical Eigenfunction (Mode)	$\Phi^i(x,y)$	$\Psi^i(x,y)$
Mean Velocity Component	$\overline{u(x,y)}$	$\overline{v(x,y)}$
Fluctuating Velocity Component	$u'(x,y,t)$	$v'(x,y,t)$

from each instant in time, $u(x,y,t)$ or $v(x,y,t)$, is called a snapshot. The mean velocity components, $\overline{u(x,y)}$ and $\overline{v(x,y)}$, are also referred to as the ensemble averages

of the snapshots, $< u >$ and $< v >$, respectively. In each case, each component of velocity is represented by a linear combination of N modes. As indicated, the modal amplitudes vary only with time, and the modes vary only with space. The decomposition defined in Equation 6.20 is used by Holmes et al. [59], and the definition in Equation 6.21 is used by Siegel et al. [98], among others [33, 52, 53, 55].

In order to define how the modes are obtained, the definition of the inner product must first be established. Two definitions of the inner product are considered in this study, given by the following equations:

$$\langle u, u \rangle = u^T \cdot u \tag{6.22}$$

$$\langle u, u \rangle = \int_\Omega u \cdot u \, dA \tag{6.23}$$

The definition in Equation 6.22 is a vector inner product. Equation 6.23 is in an integral inner product, integrated over the whole domain, Ω.

In order to generate the modes, flow field data is taken from the simulation while the system is in a periodic oscillatory state. Flow field data is taken from an integer number of periods of oscillation [51]. The set of data used to calculated the modes is called an ensemble [47]. The time interval between any two successive sampled states is the same. To construct the modes, the average autocorrelation matrix is defined as the following [106]:

$$C_u = \langle u(x,y,t), u(x,y,t') \rangle, \quad C_v = \langle v(x,y,t), v(x,y,t') \rangle \tag{6.24}$$

$$C'_u = \langle u'(x,y,t), u'(x,y,t') \rangle, \quad C'_v = \langle v'(x,y,t), v'(x,y,t') \rangle \tag{6.25}$$

where C_u and C'_u are the autocorrelation matrices constructed from the u component data, and C_v and C'_v are the autocorrelation matrices from the v component data. All of the component data are column vectors that have length P, where P is the number

of nodes (or points) in the flow field. In Equation 6.25, the fluctuating components are $u' = u - \overline{u}$ and $v' = v - \overline{v}$. The inner product of each the M snapshots is taken with every other snapshot. In this study, a total of 487 snapshots ($M = 487$) are used, spaced 0.01 seconds apart. Equation 6.24 applies to the POD definition in Equation 6.20 (total velocity), and Equation 6.25 applies to the POD definition in Equation 6.21 (velocity fluctuations). The mean components of the data fields, $\overline{u}$ and $\overline{v}$, are calculated from one period of oscillation. The eigenvectors and eigenvalues of the autocorrelation matrix are then calculated with $C_u P = \lambda_u P$ and $C_v Q = \lambda_v Q$. The eigenvectors, which are scaled by $MATLAB^{TM}$ such that norm of each eigenvector is one, are divided by the square root of their respective eigenvalues, $\sqrt{\lambda^M}$, where λ^M is the eigenvalue for snapshot M. The POD modes are then constructed using the following relationships:

$$\Phi^K = \sum_{i=1}^{M} p_i^K u_i \qquad \Psi^K = \sum_{i=1}^{M} q_i^K v_i \tag{6.26}$$

$$\Phi^K = \sum_{i=1}^{M} p_i^K u_i' \qquad \Psi^K = \sum_{i=1}^{M} q_i^K v_i' \tag{6.27}$$

where Equation 6.26 refers to the definition in Equation 6.20 (total velocity), and Equation 6.27 refers to Equation 6.21 (velocity fluctuations). The terms p_i^K and q_i^K refer to the i^{th} element of the K^{th} eigenvector of the autocorrelation matrices, P and Q, respectively. Each mode K incorporates all M snapshots. Siegel et al. [98], who used the POD definition in Equation 6.21 (velocity fluctuations), found that more than 90% of the kinetic energy of the flow could be represented in the first four modes of this system. The fact that the flow field can be represented with accuracy with far fewer number of modes (N) than the number of snapshots (M) used makes the POD method a powerful order-reduction tool [59]. This is true for both definitions of the POD method. The order of the system has been reduced from M snapshots to N modes. In this case, the system of $M = 487$ snapshots can be adequately

represented by $N = 5$ modes, which is a significant reduction of order. The modes generated, both Φ and Ψ, are orthonormal and orthogonal. Therefore, the following is true [55, 59, 106]:

$$\langle \Phi^i, \Phi^k \rangle = \left\{ \begin{array}{cc} 1 & if \quad i = k \\ 0 & if \quad i \neq k \end{array} \right\} \tag{6.28}$$

The time-dependent modal amplitudes, a_i and b_i from Equations 6.20 and 6.21, can be reconstructed from flow field data. This is done with the following relationships [24]:

$$a_k(t) = \langle u(x,y,t), \Phi^K(x,y) \rangle \quad b_k(t) = \langle v(x,y,t), \Psi^K(x,y) \rangle \tag{6.29}$$

$$a_k(t) = \langle u'(x,y,t), \Phi^K(x,y) \rangle \quad b_k(t) = \langle v'(x,y,t), \Psi^K(x,y) \rangle \tag{6.30}$$

Equation 6.29 refers to the POD definition in Equation 6.20 (total velocity), and Equation 6.30 refers to the Equation 6.21 (velocity fluctuations). For each mode, K, these inner products are calculated for all times, t. These are the expected values of the modal amplitudes that should be valid for the unforced case. These values are taken directly from the data and are not the result of any reduced-order model calculations.

6.6 Galerkin Projection

In order to obtain a low-order model to predict the evolution of the flow, a Galerkin projection of the Navier-Stokes equations is performed [24, 51, 55, 59, 94]. The non-dimensionalized Navier-Stokes equation may be written with the following notation:

$$u_x + v_y = 0 \tag{6.31}$$

$$\begin{aligned} u' + uu_x + vu_y - \frac{1}{Re}(u_{xx} + u_{yy}) + p_x &= 0 \\ v' + uv_x + vv_y - \frac{1}{Re}(v_{xx} + v_{yy}) + p_y &= 0 \end{aligned} \tag{6.32}$$

where a single subscripted variable denotes a first spatial derivative, a double subscripted variable denotes a second spatial derivative, and u' and v' are time derivatives. If the POD definition in Equation 6.20 (total velocity) is used, each term in Equation 6.32 can be rewritten in terms of the modes and modal amplitudes as shown below:

$$
\begin{aligned}
u' &= \sum_{i=1}^{N} \dot{a}_i \Phi^i \\
uu_x &= \left(\sum_{i=1}^{N} a_i \Phi^i\right)\left(\sum_{i=1}^{N} a_i \Phi_x^i\right) = \sum_{i=1}^{N}\sum_{j=1}^{N} a_i a_j \Phi^i \Phi_x^j \\
vu_y &= \left(\sum_{i=1}^{N} b_i \Psi^i\right)\left(\sum_{i=1}^{N} a_i \Phi_y^i\right) = \sum_{i=1}^{N}\sum_{j=1}^{N} b_i a_j \Psi^i \Phi_y^j \\
u_{xx} &= \sum_{i=1}^{N} a_i \Phi_{xx}^i \\
u_{yy} &= \sum_{i=1}^{N} a_i \Phi_{yy}^i \\
v' &= \sum_{i=1}^{N} \dot{b}_i \Psi^i \\
uv_x &= \left(\sum_{i=1}^{N} a_i \Phi^i\right)\left(\sum_{i=1}^{N} b_i \Psi_x^i\right) = \sum_{i=1}^{N}\sum_{j=1}^{N} a_i b_j \Phi^i \Psi_x^j \\
vv_y &= \left(\sum_{i=1}^{N} b_i \Psi^i\right)\left(\sum_{i=1}^{N} b_i \Psi_y^i\right) = \sum_{i=1}^{N}\sum_{j=1}^{N} b_i b_j \Psi^i \Psi_y^j \\
v_{xx} &= \sum_{i=1}^{N} b_i \Psi_{xx}^i \\
v_{yy} &= \sum_{i=1}^{N} b_i \Psi_{yy}^i
\end{aligned}
\tag{6.33}
$$

The modes, generated from the solution of the Navier-Stokes equations, inherently obey the incompressibility constraint (Equation 2.1 or 6.31). Therefore, when generating the reduced-order model with the Galerkin projection of the Navier-Stokes equation, the incompressibility constraint does not need to be considered explicitly. Only Equation 2.2 (which is the same as Equation 6.32) needs to be considered. When the terms in Equation 6.33 are substituted back into Equation 6.32 and solved for $\sum_{i=1}^{N} \dot{a}_i \Phi^i$ and $\sum_{i=1}^{N} \dot{b}_i \Psi^i$, the Navier-Stokes equations reduce to the following form:

$$\begin{aligned}
\sum_{i=1}^{N} \dot{a}_i \Phi^i &= \frac{1}{Re}\left(\sum_{i=1}^{N} a_i \Phi^i_{xx} + \sum_{i=1}^{N} a_i \Phi^i_{yy}\right) - \sum_{i=1}^{N}\sum_{j=1}^{N} a_i a_j \Phi^i \Phi^j_x \\
&\quad - \sum_{i=1}^{N}\sum_{j=1}^{N} b_i a_j \Psi^i \Phi^j_y - p_x \\
\sum_{i=1}^{N} \dot{b}_i \Psi^i &= \frac{1}{Re}\left(\sum_{i=1}^{N} b_i \Psi^i_{xx} + \sum_{i=1}^{N} b_i \Psi^i_{yy}\right) - \sum_{i=1}^{N}\sum_{j=1}^{N} b_i b_j \Psi^i \Psi^j_y \\
&\quad - \sum_{i=1}^{N}\sum_{j=1}^{N} a_i b_j \Phi^i \Psi^j_x - p_y
\end{aligned} \tag{6.34}$$

Taking advantage of the property of orthogonality illustrated in Equation 6.28, all of the $\dot{a}_i$'s and $\dot{b}_i$'s can be eliminated from the left-hand side of Equation 6.34 except for one by taking the inner product of both sides of the equations with Φ^k and Ψ^k, respectively [55, 59]. Taking these inner products yields the following:

$$\begin{aligned}
\dot{a}_k &= \frac{1}{Re}\sum_{i=1}^{N} \left\langle \Phi^i_{xx} + \Phi^i_{yy}, \Phi^k \right\rangle a_i - \sum_{i=1}^{N}\sum_{j=1}^{N} \left\langle \Phi^i \Phi^j_x, \Phi^k \right\rangle a_i a_j \\
&\quad - \sum_{i=1}^{N}\sum_{j=1}^{N} \left\langle \Psi^i \Phi^j_y, \Phi^k \right\rangle b_i a_j - \left\langle p_x, \Phi^k \right\rangle \\
\dot{b}_k &= \frac{1}{Re}\sum_{i=1}^{N} \left\langle \Psi^i_{xx} + \Psi^i_{yy}, \Psi^k \right\rangle b_i - \sum_{i=1}^{N}\sum_{j=1}^{N} \left\langle \Psi^i \Psi^j_y, \Psi^k \right\rangle b_i b_j \\
&\quad - \sum_{i=1}^{N}\sum_{j=1}^{N} \left\langle \Phi^i \Psi^j_x, \Psi^k \right\rangle a_i b_j - \left\langle p_y, \Psi^k \right\rangle
\end{aligned} \tag{6.35}$$

This result is the reduced-order, coupled, ordinary differential equation representation of the Navier-Stokes equations for the flow past the circular cylinder using the POD definition in Equation 6.20, which uses the total velocity. Since a total of 5 modes ($k = N = 5$) are being used for each component, the infinite-dimensional Navier-Stokes equations have been reduced to 10 ordinary differential equations. Equation 6.35 is the model that will predict the behavior of the flow field by computing all of the time-dependent modal amplitudes for the total velocity POD definition (Equation 6.20) [59].

If the POD definition in Equation 6.21 (subtracting the mean flow field from each snapshot) is used, each term in Equation 6.32 can be rewritten in terms of the modes

and modal amplitudes as shown below:

$$
\begin{aligned}
u' &= \sum_{i=1}^{N} \dot{a}_i \Phi^i \\
uu_x &= \left(\overline{u} + \sum_{i=1}^{N} a_i \Phi^i\right)\left(\overline{u}_x + \sum_{i=1}^{N} a_i \Phi^i_x\right) = \overline{u}\overline{u}_x + \sum_{i=1}^{N} a_i \overline{u} \Phi^i_x \\
&\quad + \sum_{i=1}^{N} a_i \overline{u}_x \Phi^i + \sum_{i=1}^{N}\sum_{j=1}^{N} a_i a_j \Phi^i \Phi^j_x \\
vu_y &= \left(\overline{v} + \sum_{i=1}^{N} b_i \Psi^i\right)\left(\overline{u}_y + \sum_{i=1}^{N} a_i \Phi^i_y\right) = \overline{v}\overline{u}_y + \sum_{i=1}^{N} a_i \overline{v} \Phi^i_y \\
&\quad + \sum_{i=1}^{N} b_i \overline{u}_y \Psi^i + \sum_{i=1}^{N}\sum_{j=1}^{N} b_i a_j \Psi^i \Phi^j_y \\
u_{xx} &= \overline{u}_{xx} + \sum_{i=1}^{N} a_i \Phi^i_{xx} \\
u_{yy} &= \overline{u}_{yy} + \sum_{i=1}^{N} a_i \Phi^i_{yy} \\
v' &= \sum_{i=1}^{N} \dot{b}_i \Psi^i \\
uv_x &= \left(\overline{u} + \sum_{i=1}^{N} a_i \Phi^i\right)\left(\overline{v}_x + \sum_{i=1}^{N} b_i \Psi^i_x\right) = \overline{u}\overline{v}_x + \sum_{i=1}^{N} b_i \overline{u} \Psi^i_x \\
&\quad + \sum_{i=1}^{N} a_i \overline{v}_x \Phi^i + \sum_{i=1}^{N}\sum_{j=1}^{N} a_i b_j \Phi^i \Psi^j_x \\
vv_y &= \left(\overline{v} + \sum_{i=1}^{N} b_i \Psi^i\right)\left(\overline{v}_y + \sum_{i=1}^{N} b_i \Psi^i_y\right) = \overline{v}\overline{v}_y + \sum_{i=1}^{N} b_i \overline{v} \Psi^i_y \\
&\quad + \sum_{i=1}^{N} b_i \overline{v}_y \Psi^i + \sum_{i=1}^{N}\sum_{j=1}^{N} b_i b_j \Psi^i \Psi^j_y \\
v_{xx} &= \overline{v}_{xx} + \sum_{i=1}^{N} b_i \Psi^i_{xx} \\
v_{yy} &= \overline{v}_{yy} + \sum_{i=1}^{N} b_i \Psi^i_{yy}
\end{aligned}
\tag{6.36}
$$

When the terms in Equation 6.36 are substituted back into the Equation 6.32 and solved for $\sum_{i=1}^{N} \dot{a}_i \Phi^i$ and for $\sum_{i=1}^{N} \dot{b}_i \Psi^i$, the Navier-Stokes equations take the following form:

$$\begin{aligned}
\sum_{i=1}^{N} \dot{a}_i \Phi^i &= \frac{1}{Re}\left(\sum_{i=1}^{N} a_i \Phi^i_{xx} + \sum_{i=1}^{N} a_i \Phi^i_{yy}\right) - \sum_{i=1}^{N} a_i \overline{u} \Phi^i_x - \sum_{i=1}^{N} a_i \overline{u}_x \Phi^i - \sum_{i=1}^{N} a_i \overline{v} \Phi^i_y \\
&- \sum_{i=1}^{N} b_i \overline{u}_y \Psi^i - \sum_{i=1}^{N}\sum_{j=1}^{N} a_i a_j \Phi^i \Phi^j_x - \sum_{i=1}^{N}\sum_{j=1}^{N} b_i a_j \Psi^i \Phi^j_y \\
&+ \left(\frac{1}{Re}\left(\overline{u}_{xx} + \overline{u}_{yy}\right) - \overline{u}\overline{u}_x - \overline{v}\overline{u}_y\right) - p_x \\
\\
\sum_{i=1}^{N} \dot{b}_i \Psi^i &= \frac{1}{Re}\left(\sum_{i=1}^{N} b_i \Psi^i_{xx} + \sum_{i=1}^{N} b_i \Psi^i_{yy}\right) - \sum_{i=1}^{N} b_i \overline{u} \Psi^i_x - \sum_{i=1}^{N} b_i \overline{v}_y \Psi^i - \sum_{i=1}^{N} b_i \overline{v} \Psi^i_y \\
&- \sum_{i=1}^{N} a_i \overline{v}_x \Phi^i - \sum_{i=1}^{N}\sum_{j=1}^{N} b_i b_j \Psi^i \Psi^j_y - \sum_{i=1}^{N}\sum_{j=1}^{N} a_i b_j \Phi^i \Psi^j_x \\
&+ \left(\frac{1}{Re}\left(\overline{v}_{xx} + \overline{v}_{yy}\right) - \overline{u}\overline{v}_x - \overline{v}\overline{v}_y\right) - p_y
\end{aligned} \tag{6.37}$$

Taking advantage of the property of orthogonality illustrated in Equation 6.28 as before, all of the $\dot{a}_i$'s and $\dot{b}_i$'s can be eliminated from the left-hand side of Equation 6.37 except for one by taking the inner product of both sides of the equations with Φ^k and Ψ^k, respectively [55, 59]. Taking these inner products yields the following:

$$\begin{aligned}
\dot{a}_k = &\sum_{i=1}^{N} \left\langle \left(\frac{1}{Re}\left(\Phi^i_{xx} + \Phi^i_{yy}\right) - \overline{u}\Phi^i_x - \overline{u}_x \Phi^i - \overline{v}\Phi^i_y\right), \Phi^k \right\rangle a_i - \sum_{i=1}^{N} \left\langle \overline{u}_y \Psi^i, \Phi^k \right\rangle b_i \\
&- \sum_{i=1}^{N}\sum_{j=1}^{N} \left\langle \Phi^i \Phi^j_x, \Phi^k \right\rangle a_i a_j - \sum_{i=1}^{N}\sum_{j=1}^{N} \left\langle \Psi^i \Phi^j_y, \Phi^k \right\rangle b_i a_j \\
&+ \left\langle \left(\frac{1}{Re}\left(\overline{u}_{xx} + \overline{u}_{yy}\right) - \overline{u}\overline{u}_x - \overline{v}\overline{u}_y\right), \Phi^k \right\rangle - \left\langle p_x, \Phi^k \right\rangle \\
\\
\dot{b}_k = &\sum_{i=1}^{N} \left\langle \left(\frac{1}{Re}\left(\Psi^i_{xx} + \Psi^i_{yy}\right) - \overline{u}\Psi^i_x - \overline{v}_y \Psi^i - \overline{v}\Psi^i_y\right), \Psi^k \right\rangle b_i - \sum_{i=1}^{N} \left\langle \overline{v}_x \Phi^i, \Psi^k \right\rangle a_i \\
&- \sum_{i=1}^{N}\sum_{j=1}^{N} \left\langle \Psi^i \Psi^j_y, \Psi^k \right\rangle b_i b_j - \sum_{i=1}^{N}\sum_{j=1}^{N} \left\langle \Phi^i \Psi^j_x, \Psi^k \right\rangle a_i b_j \\
&+ \left\langle \left(\frac{1}{Re}\left(\overline{v}_{xx} + \overline{v}_{yy}\right) - \overline{u}\overline{v}_x - \overline{v}\overline{v}_y\right), \Psi^k \right\rangle - \left\langle p_y, \Psi^k \right\rangle
\end{aligned} \tag{6.38}$$

Like Equation 6.35, Equation 6.38 is the reduced-order, coupled, ordinary differential equation representation of the Navier-Stokes equations for the flow past the circular cylinder, this time using the POD definition in Equation 6.21 which uses the velocity fluctuations. Since a total of 5 modes ($k = N = 5$) are being used for each component, the infinite-dimensional Navier-Stokes equations have been reduced to 10 ordinary differential equations. Equation 6.38 is the model that will predict the behavior of the flow field by computing all of the time-dependent modal amplitudes for the velocity fluctuation POD definition (Equation 6.21) [55].

6.7 Conclusions

Proper Orthogonal Decomposition and the Galerkin Projection of the Navier-Stokes equations were described. A general overview of the method for obtaining empirical eigenfunctions that are optimal with respect to retained kinetic energy was given, followed by a description of the specific application of this method to flow past the circular cylinder. Finally, the Galerkin Projection of the Navier-Stokes equations was described, and the final form of a reduced-order model which describes the dominant dynamics of the flow past the circular cylinder was given.

Chapter 7

Application of Proper Orthogonal Decomposition to Flow Past a Cylinder

7.1 Introduction

This chapter shows the results of computing Proper Orthogonal Decomposition modes with the various definitions and two different geometries given in Chapter 6. Modes that have been obtained by different methods are compared. A reconstruction of the flow field and a limitation of this reconstruction are given. Modal amplitudes are calculated. Finally, a control scheme based on a previous study is applied to this problem.

7.2 Computation of the modes

At Reynolds number 100, after an initial transient phase, vortices form behind the cylinder and then are shed into the passing flow field behind the cylinder (or wake).

These vortices are shed alternately from the top and the bottom of the cylinder [12].

Siegel et al. [98] used a flow field with the same dimensions as the field used in this study, shown in Figure 6.1. Siegel et al. used this domain to capture the flow profile. However, to compute the empirical eigenfunctions (or modes) for their POD model, Siegel et al. [98] used a subset of this domain. This smaller domain, used to calculate the POD modes, extended 7 cylinder diameters behind the cylinder, 1 diameter in front, 2 diameters above, and 2 diameters below [98].

In one case, the same approach is used in this study. Initially, the entire flow field profile is computed for 15 seconds at Reynolds number 100 using $FEMLAB^{TM}$. The mesh structure shown in the right half of Figure 6.2 is used. In this case, the entire flow field is used to calculate the solution of the flow field, and the subset domain, which is the smaller inner rectangle, is used to calculate the POD modes. From this point forward, this case shall be referred to as the subset domain case. During the simulation, the profile evolves from the initial condition, through the transient phase, reaching a state of periodic oscillations. Figure 7.1 shows a surface velocity plot ($U = \sqrt{u^2 + v^2}$) of the flow field after 15 seconds. The darkest red areas are the highest velocities, and the darkest blue are the lowest velocities. The small, dark blue region immediately behind the cylinder is the recirculation region. The green and red circular (roughly) regions behind the cylinder, centered above and below the cylinder, are the vortices. These vortices are shed successively from the top and bottom of the cylinder during the periodic oscillatory steady state.

In their model, Siegel et al. [98] used the first four modes calculated as described in Section 6.5 and constructed an additional fifth mode. The fifth mode is derived by subtracting the mean (incoming) freestream velocity, u_{inf} or v_{inf}, from the mean flow distribution of the unforced field, $\overline{u}$ or $\overline{v}$ [55]. The u component of the incoming

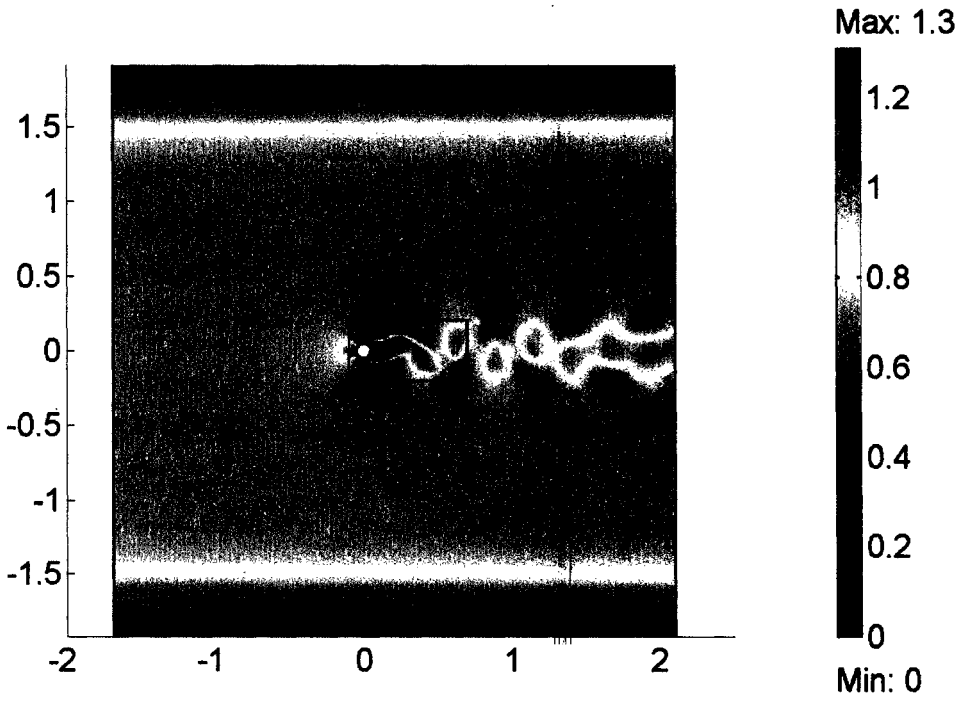

Figure 7.1: Total velocity (U) surface plot after 15 seconds, subset of flow field used to calculate POD modes.

freestream velocity, u_{inf}, in this study is the 30th order polynomial function discussed in Section 2.2 that is used as the inlet boundary condition for u, and v is zero. The mean flow distribution of the unforced field, $\overline{u}$ or $\overline{v}$, is calculated by averaging the velocity values at each point in the flow field over one oscillation period. In this study, when the POD definition of Equation 6.20 (total velocity) is used, the five modes employed are constructed as described in Section 6.5. When Equation 6.21 (velocity fluctuations) is used, the first four modes used are constructed as described in Section 6.5, and a fifth mode, as constructed by Siegel et al. [98] and described above, is also used.

To compute the POD modes in the subset domain case (where the modes are calculated from a subset of total flow field, as shown on the right side of Figure 6.2), velocity data is extracted only from the region enclosed in the box (black outline in

Figure 7.1) immediately around the cylinder. As mentioned above, this region has the same dimensions as the region for which Siegel et al. [98] computed their POD modes. One full period, P, of oscillation is 0.608 seconds. The u and v component data are collected from the inner region for 4.87 seconds, or roughly 8 periods of oscillation. As described in Chapter 6, for each component, the correlation matrices are calculated using the POD definition in Equation 6.21 (velocity fluctuations) and the vector inner product definition in Equation 6.22. The eigenvalues and eigenvectors are computed, normalized, and the first four POD modes are calculated. The fifth mode is $\overline{u} - u_{inf}$, as defined above. Figure 7.2 shows the u component modes, Φ^i, of the subset domain case. The v component modes, Ψ^i, are shown in the Appendix (Figure A.1). Figure 7.2 shows the relationship between the modes. The mode based on $\overline{u}$, Φ^5, is the largest scale spatial structure. Φ^1 and Φ^2 resemble each other, and have smaller spatial structures than Φ^5. Φ^2 looks like Φ^1 with a shift in phase. Φ^3 and Φ^4 have the smallest spatial structures shown. Φ^4 resembles Φ^3 with shift in phase.

The POD modes are also calculated for the mesh structure shown on the left half of Figure 6.2. These POD modes are calculated for the entire flow field. In one case, the u component modes, Φ^i, using the POD definition in Equation 6.20 (total velocity) and the integral inner product in Equation 6.23, are shown in Figure 7.3. In this case, all five modes are calculated as described in Section 6.5. The v component modes, Ψ^i, are shown in Figure A.2 in the Appendix. As with the modes in Figure 7.2, some of the modes in Figure 7.3 resemble each other. Φ^3 looks like Φ^2 with a phase shift, and Φ^5 looks like Φ^4 with a phase shift. The interior of Φ^1 resembles Φ^5 from Figure 7.2, except that the values span a larger range in Φ^5 of Figure 7.2. In this case, just as Φ^1 closely resembles $\overline{u}$, Ψ^3 closely resembles $\overline{v}$.

Figure 7.4 shows the u component modes, Φ^i, using the POD definition in Equation

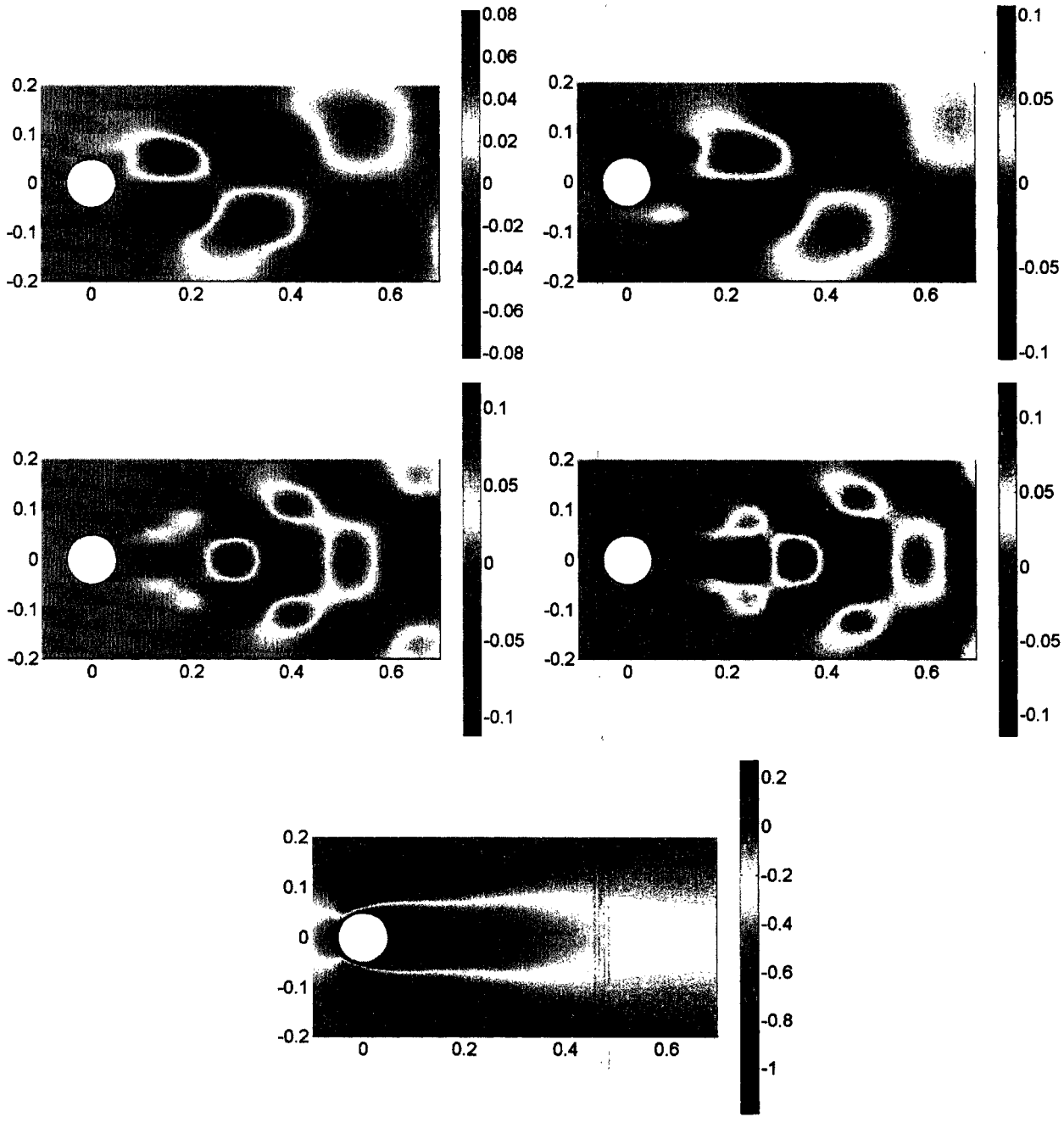

Figure 7.2: Φ^i, subset of flow field used to calculate POD modes: Top Row - Left: Φ^1, Right: Φ^2, Middle Row - Left: Φ^3, Right: Φ^4, Bottom Row - Φ^5.

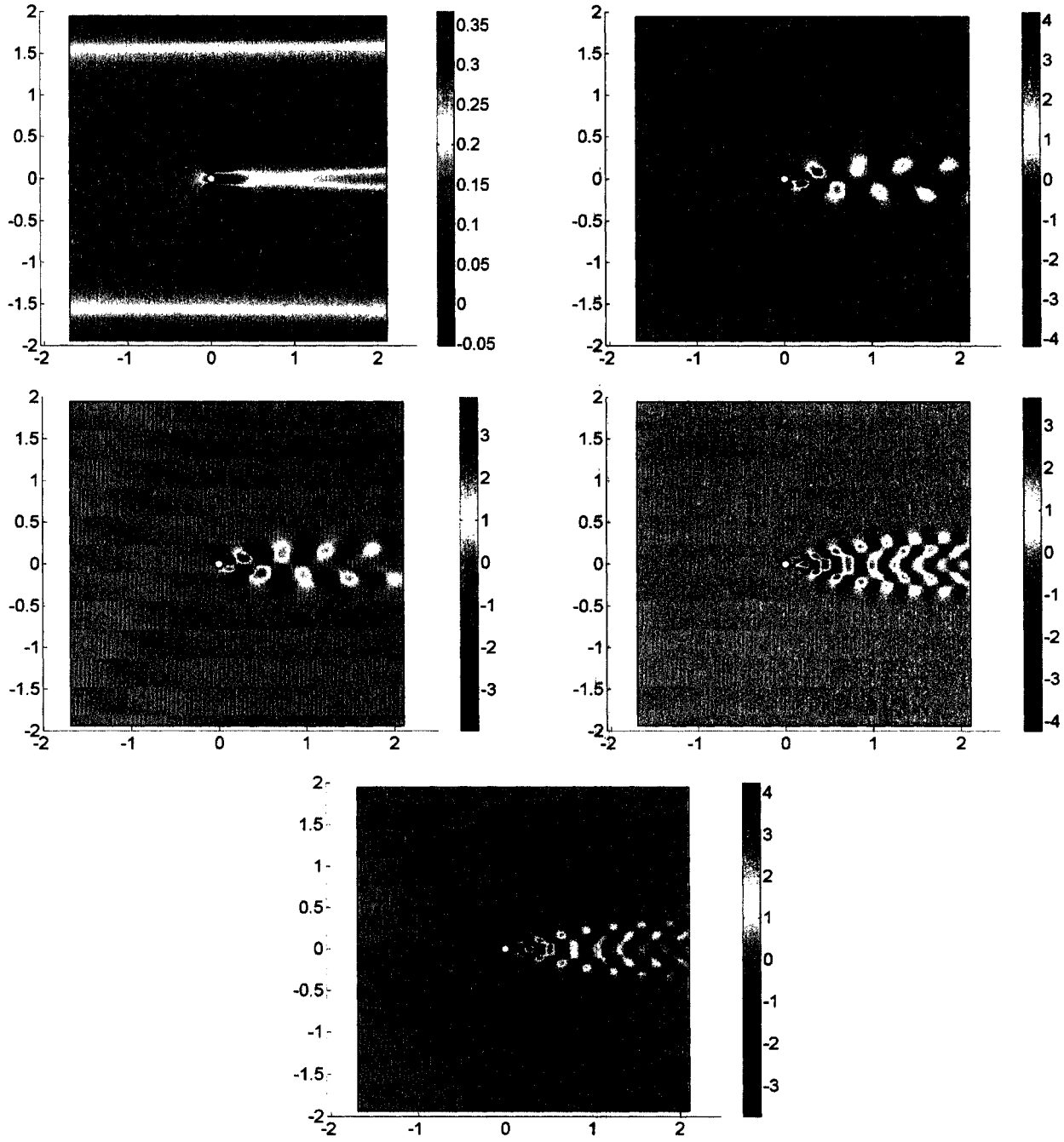

Figure 7.3: Φ^i, total velocity POD definition: Top Row - Left: Φ^1, Right: Φ^2, Middle Row - Left: Φ^3, Right: Φ^4, Bottom Row - Φ^5.

6.21 (velocity fluctuations) and the integral inner product, Equation 6.23. The first four modes are calculated as described in Section 6.5, and the fifth mode is $\overline{u} - u_{inf}$. For the v component, this results in simply $\overline{v}$ since v_{inf} is zero. The v component modes, Ψ^i, are shown in Figure A.3 in the Appendix. As expected, these modes resemble those in Figure 7.2 (for the case where the modes are calculated from a subset of the total flow field domain) because both sets of modes are calculated using the same POD definition.

The vector inner product, Equation 6.22, is also used to find POD modes with both definitions. The surface plots for these modes appear to be exactly the same in a relative sense, but are scaled differently than the POD modes obtained with the integral inner product. In other words, the POD modes obtained with the integral inner product defined by Equation 6.23 are the same as the vector inner product modes obtained by Equation 6.22 multiplied by a constant. The POD modes obtained with the integral inner product are 50 to 100 times greater in magnitude than the vector inner product modes.

7.3 Reconstruction of the unforced flow field

As described by Equations 6.29 (total velocity) and 6.30 (velocity fluctuations), the time-dependent modal amplitudes that describe the evolution of the unforced flow field may be reconstructed. Because the fifth mode from the set of modes defined by Equation 6.21 (velocity fluctuations) is not defined by the normalized eigenvectors of the autocorrelation matrix, but instead is defined as $\overline{u} - u_{inf}$, Φ^5 and Ψ^5 in this set of modes are neither orthogonal nor orthonormal to the other 4 modes. Because of this lack of orthogonality, in the calculation of the modal amplitudes for Φ^5 and Ψ^5 (which are designated a_5 and b_5, respectively) with Equation 6.30, additional terms

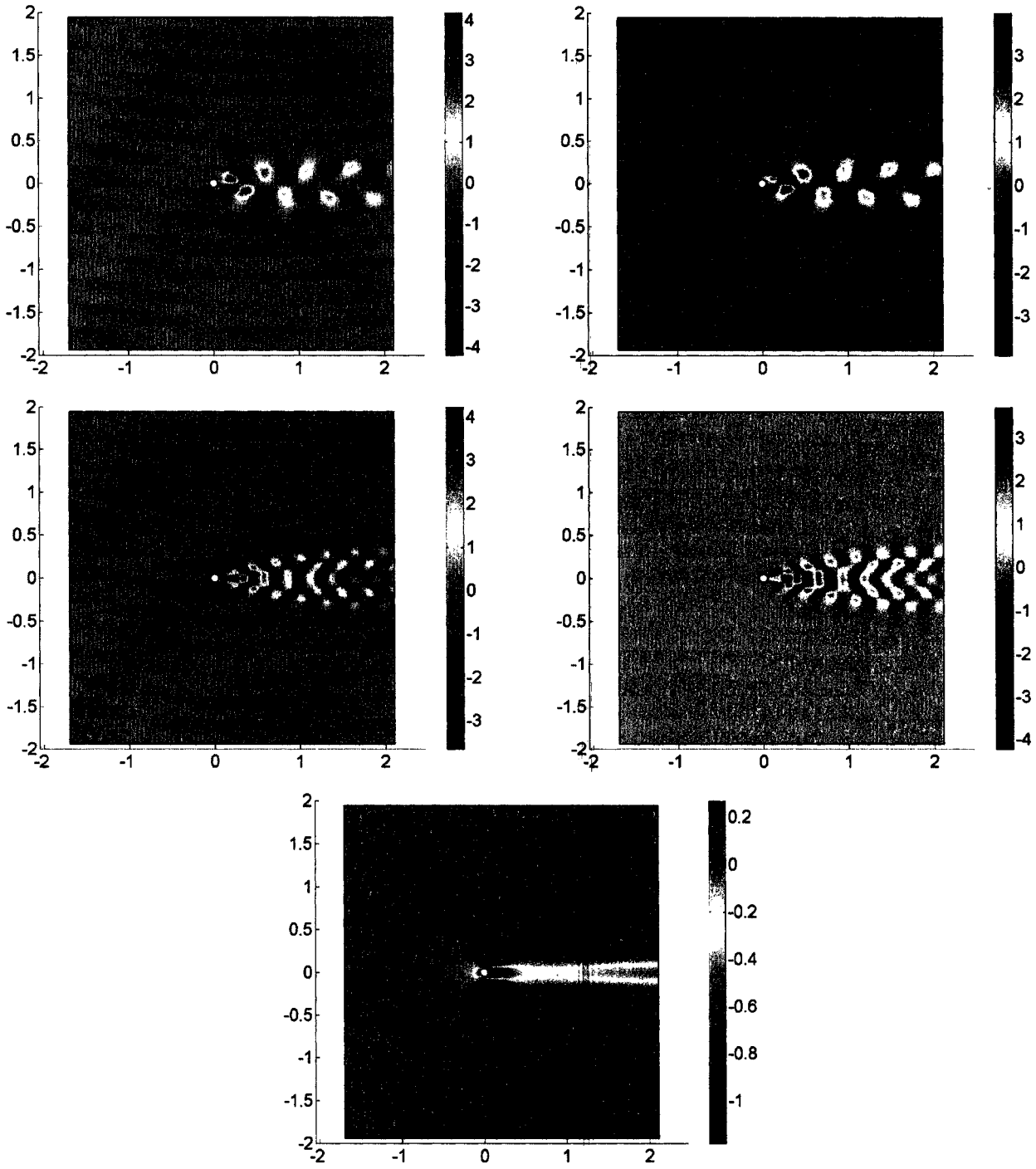

Figure 7.4: Φ^i, velocity fluctuations POD definition: Top Row - Left: Φ^1, Right: Φ^2, Middle Row - Left: Φ^3, Right: Φ^4, Bottom Row - Φ^5.

appear that are normally cancelled out in the computation of the other four modal amplitudes. These additional terms are disregarded, however, in this and all other similar calculations henceforth. Instead, the modal amplitudes, a_5 and b_5, in the case of the POD modes defined by Equation 6.21, are defined just as the other four modal amplitudes (Equation 6.30).

Once the modal amplitudes are obtained, the POD definitions, Equations 6.20 and 6.21, are used to reconstruct the unforced flow field [59]. Figure 7.5 shows a comparison between full Navier-Stokes simulation solved by $FEMLAB^{TM}$ and the

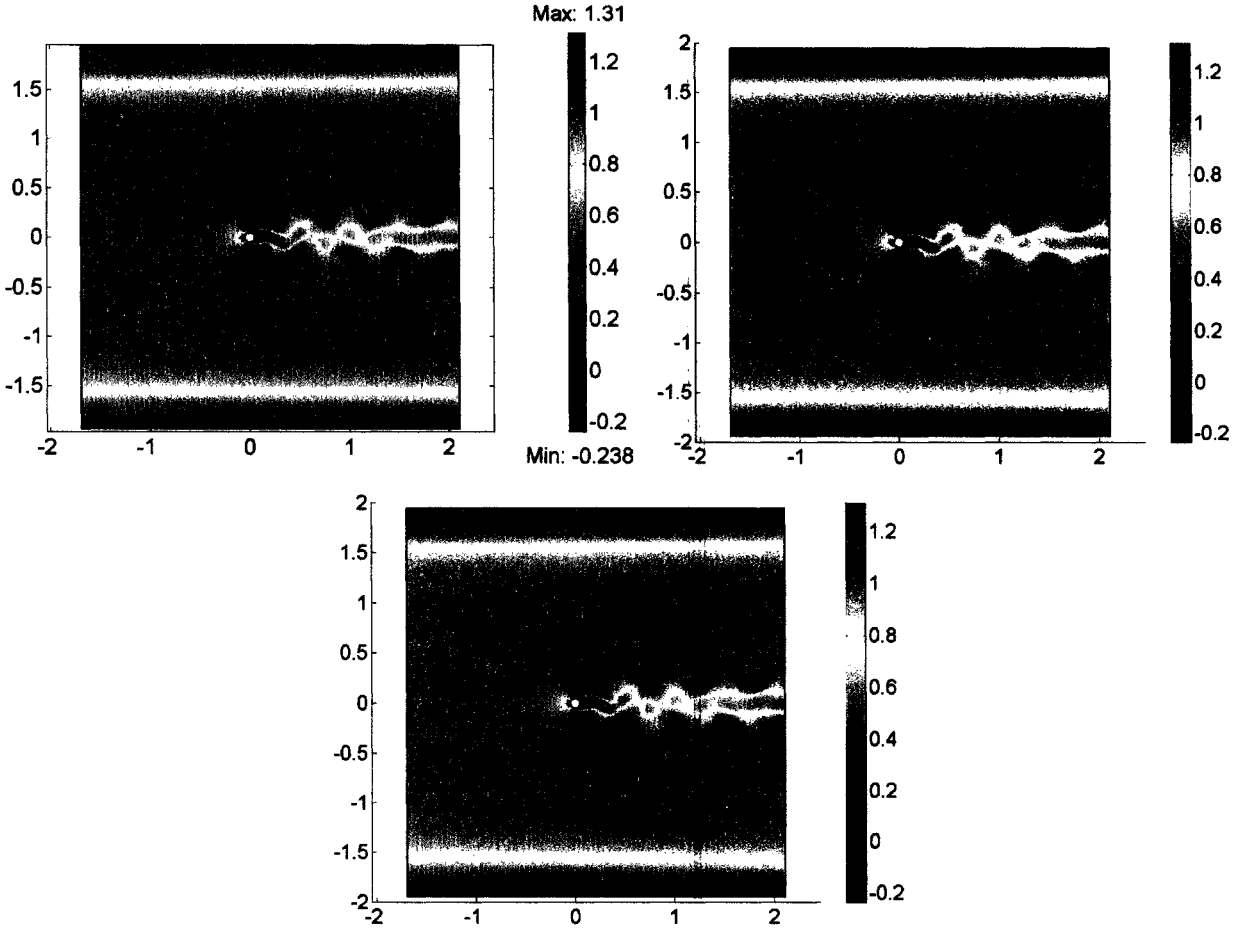

Figure 7.5: Comparison between simulation and POD reconstruction after 15 seconds, u surface plots: Top Row, total velocity POD definition - Left: simulation, Right: POD reconstruction, Bottom Row - reconstruction from velocity fluctuations POD definition.

reconstruction with the modes and modal amplitudes for the u component of the velocity field after 15 seconds. The comparison of the full Navier-Stokes simulation and the the reconstruction for the v component is shown in the Appendix in Figure A.4. Figure 7.6 shows the simulation versus the reconstruction for the subset domain

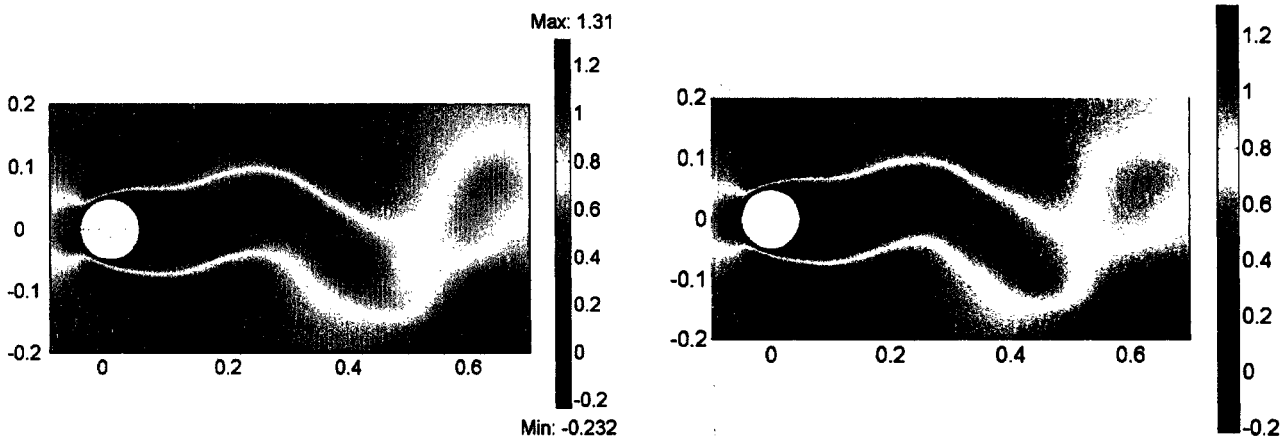

Figure 7.6: Comparison between simulation and POD reconstruction after 15 seconds, subset of total flow field used to calculate POD modes, u surface plots - Left: simulation, Right: POD reconstruction.

case. For this case, the velocity fluctuations definition of the POD modes is used. Both Figure 7.5 and Figure 7.6 show that there is almost no difference between the reconstructions from either POD definition, nor is there any significant difference between the reconstructions with 5 POD modes and the full Navier-Stokes simulation.

Animation of the reconstruction reveals that certain smaller-scale spatial structures that are present in the full simulation are not present in the reconstruction. Due to the level of discretization that is present in the simulation, some computational artifacts are present in the full simulation. at some time in the full simulation before the steady state is reached, these computational artifacts are manifested in the simulation as small disturbances, present near the boundaries of the flow field. The disturbances are very small in structure, and only occur at a certain specific location

on the boundary. The small-scale disturbances are essentially "filtered out" by this reconstruction method. Because only the first five POD modes are used in the reconstruction, all smaller-scale spatial structures that do occur in the full simulation are excluded in the reconstruction.

7.4 Transient state

Because the POD modes are derived only from periodic oscillatory data in all cases, the transient state, before the system reaches the periodic state, is not reproduced. Instead, when the system is reconstructed from the POD modes and modal amplitudes, the system initially is at a state that resembles Φ^1 for the total velocity POD definition or Φ^5 for the velocity fluctuations POD definition. Both of these modes resemble the mean flow distribution. The system stays at this mean flow state for a few seconds (as long as the transient state lasts in the simulation), and then the vortices start to grow and shed periodically. Figure 7.7 shows the difference between the simulation and the reconstruction at $t = 2$ seconds (which is during the time the

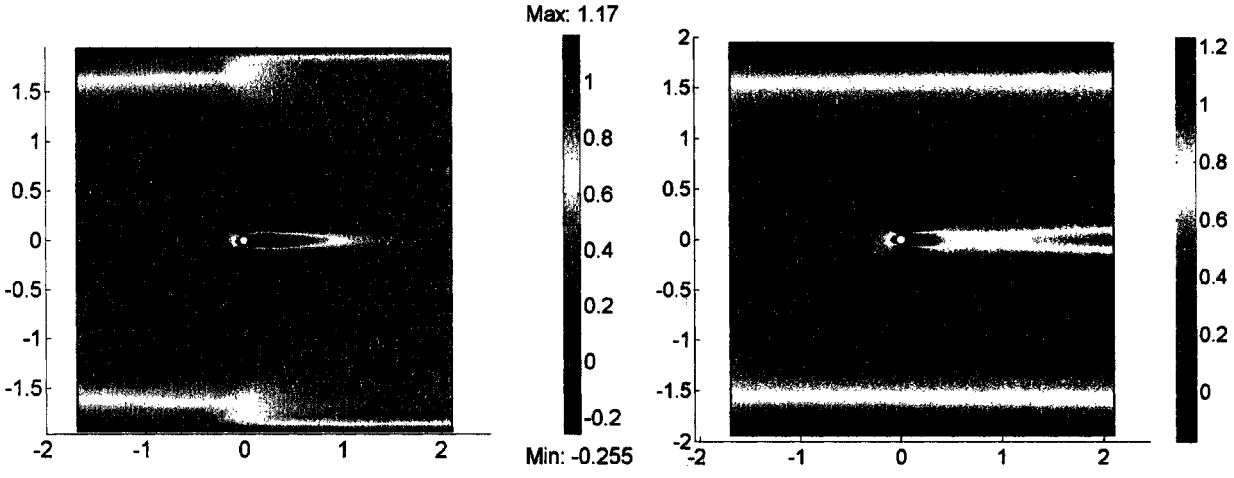

Figure 7.7: Dissimilarity between transient states of simulation and reconstruction, u surface plots after 2 seconds - Left: simulation, Right: POD reconstruction.

system is in the transient state) for the u velocity component. As Figure 7.7 shows, the features of the transient state are not modeled by the POD reconstruction. The formation of the boundary layer and growth of the recirculation region that occur during the transient phase of the simulation do not appear in the POD reconstruction. This is because neither of these events are included in the data that went into the autocorrelation matrix used for computing the POD modes. As shown here, the POD reconstruction is not a substitute for the full simulation, in that all the features of the full simulation are not reproduced by the POD reconstruction.

7.5 Modal amplitudes

Because of how closely the different reconstructions resemble each other, it is useful to compare the modal amplitudes from the different methods with each other to ascertain the variation between the methods. Using the vector inner product definition, Equation 6.22, and the velocity fluctuations POD definition, Equation 6.21, the modal amplitudes, a_i, corresponding to the u component modes, Φ^i shown in Figure 7.2 are calculated. These modal amplitudes are shown in Figure 7.8. For the u component modal amplitudes, the values of a_5 are multiplied by 32 to more clearly show the behavior of a_5 as it evolves over time. For both components, the modal amplitudes start at zero and grow to their periodic oscillatory steady states in about 7 seconds. As can be seen in Figure 7.8, the u component modal amplitudes, a_i, are similar in magnitude to the v component modal amplitudes, b_i. For both u and v components, the modal amplitudes for Mode 1 and 2, a_1 and b_1 for Mode 1 and a_2 and b_2 for Mode 2, are very close to each other, as are the amplitudes for Modes 3 (a_3 and b_4) and 4 (a_4 and b_4). The amplitudes for Mode 5 for both components, a_5 and b_5, are much smaller in magnitude than the other modes. It should be noted that,

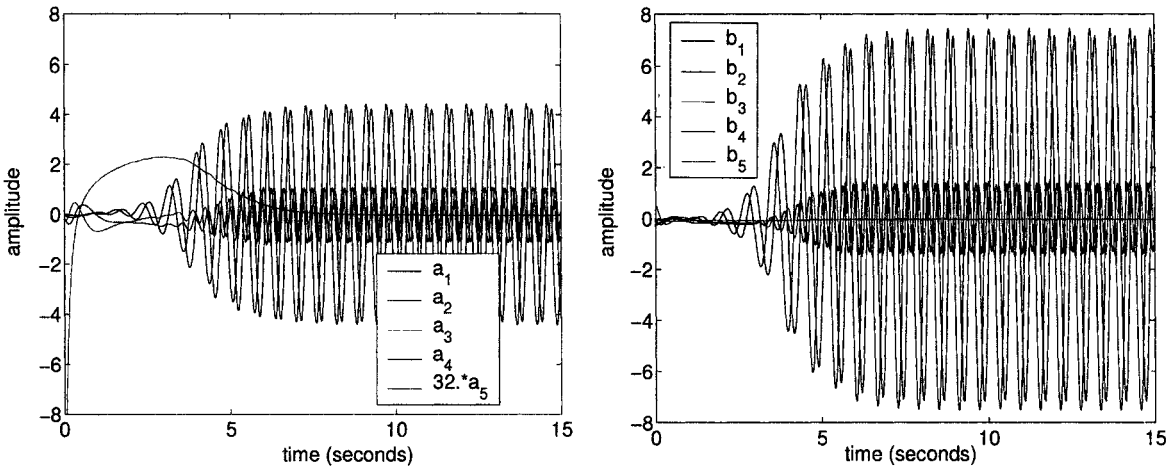

Figure 7.8: Modal amplitudes, vector inner product, subset of flow field used to calculate POD modes - Left: a_i, Right: b_i.

using the velocity fluctuations definition of POD (Equation 6.21) and defining the fifth mode as $\overline{u} - u_{inf}$, the magnitude of a_5 depends strictly on the incoming velocity, u_{inf}, not the Reynolds number. In Siegel et al. [98], where the Reynolds is the same (100), but u_{inf} is 32 times greater, a_5 is 32 times larger, as shown in Figure 7.8.

For the case where the whole domain is used to calculate the modal amplitudes, a_i and b_i, are computed. The integral inner product (Equation 6.23) is used to calculate the modal amplitudes, a_i and b_i, which correspond to the modes Φ^i and Ψ^i, respectively. These modal amplitudes are shown in Figure 7.9. The modal amplitudes shown on the top row of Figure 7.9 are for the POD definition in Equation 6.20 (total velocity) while the bottom row shows the amplitudes for Equation 6.21 (velocity fluctuations). Note the top left figure in Figure 7.9, a_i for the total velocity, is not to the same scale as the other figures. The amplitudes in the bottom row, a_i and b_i for the velocity fluctuations, exhibit the same trends as those found in Figure 7.8, in that the amplitudes for Mode 1 and Mode 2 for both u and v components are very close to each other, and the amplitudes for Mode 3 and 4 are very close to each other. The exception here is that a_5 is significantly greater than zero. For the total velocity case,

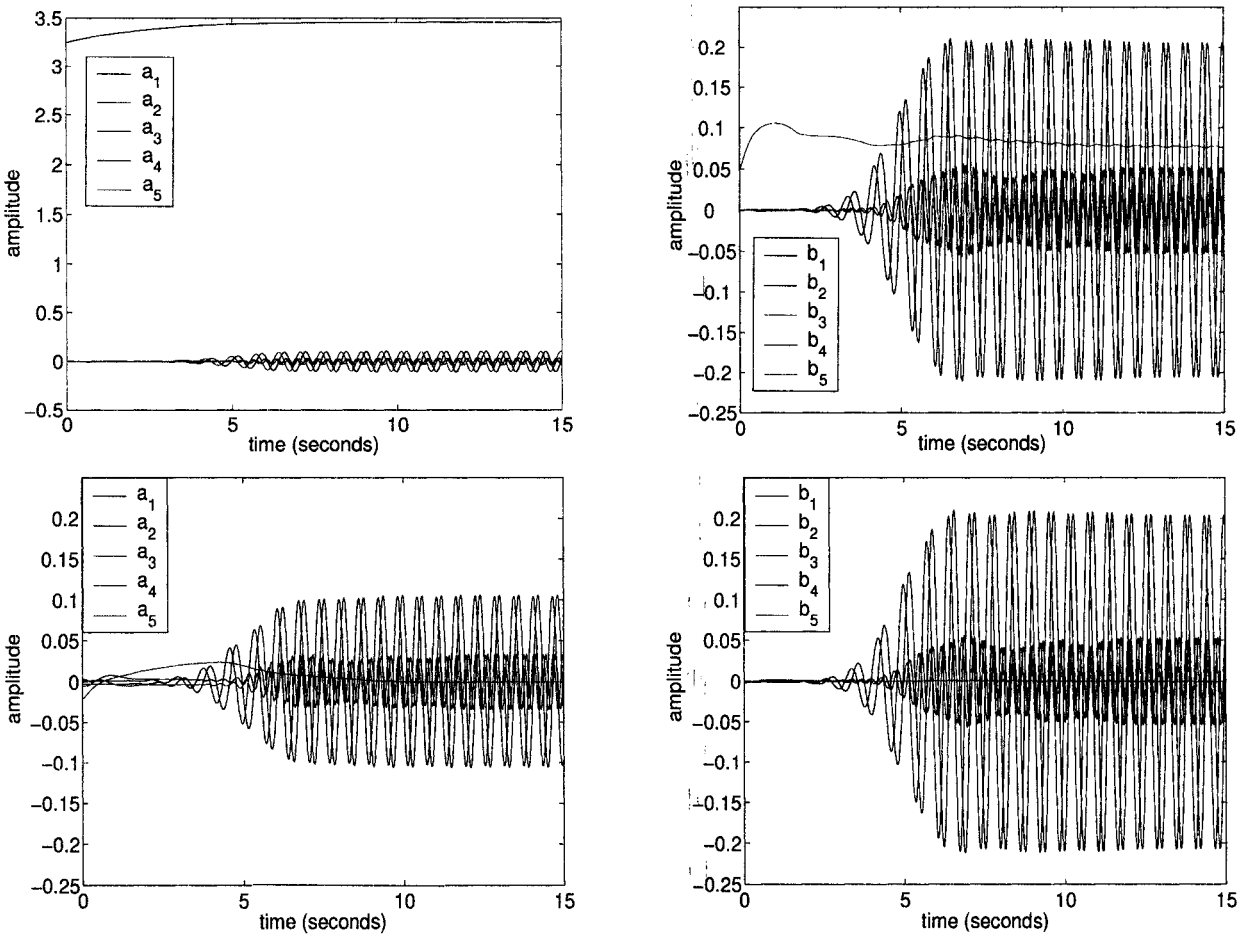

Figure 7.9: Modal amplitudes, integral inner product: Top Row, total velocity POD definition - Left: a_i, Right: b_i, Bottom Row, velocity fluctuations POD definition - Left: a_i, Right: b_i.

shown in the top row, a_1 is much larger than the other modal amplitudes. Besides a_1 and b_3 (the modal amplitudes that correspond to the modes, Φ^1 and Ψ^3, that resemble the average velocity profiles for each component), the modal amplitudes share the same relative relationships as before.

For the vector inner product, Equation 6.22, the modal amplitudes for both POD definitions are shown in Figure 7.10 The periodic oscillatory state of the modal am-

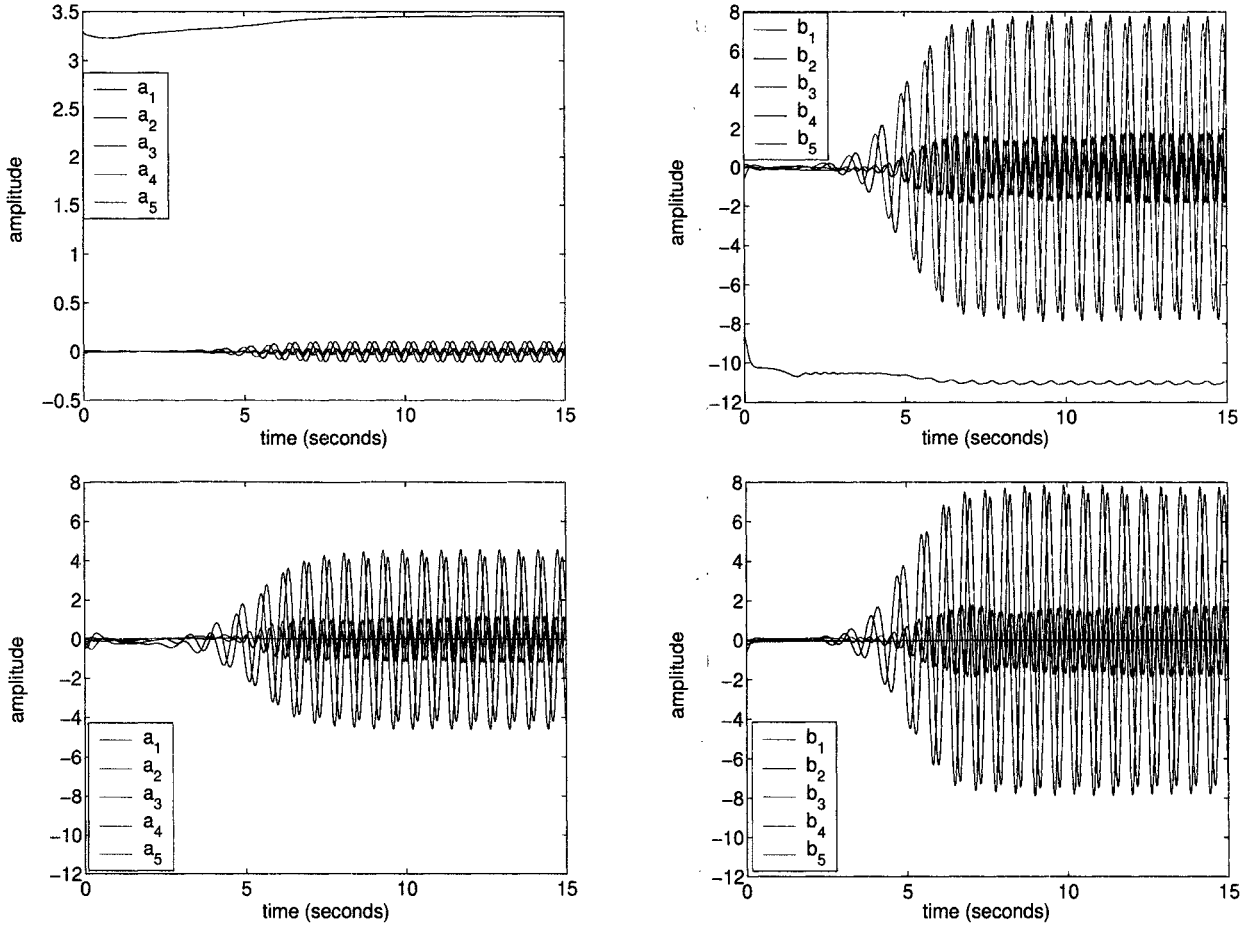

Figure 7.10: Modal amplitudes, vector inner product: Top Row, total velocity POD definition - Left: a_i, Right: b_i, Bottom Row, velocity fluctuations POD definition - Left: a_i, Right: b_i.

plitudes generated by the vector inner product closely resembles that generated by

the integral inner product with a few exceptions. For the total velocity POD definition, b_1 and b_3 are fundamentally different between the two inner product methods. The transient evolves differently for a_1 in the total velocity case, but this is of little consequence. It has already been acknowledged earlier that the transient is not well represented with these modes since the transient data is not in the data set that went into calculating the modes. As with the surface plots shown in Figure 7.7, the transient amplitudes do not represent the system well, either. As expected, the overall scale of the modal amplitudes from the vector inner product is very different from those generated by the integral inner product.

7.6 Control with the POD model

Siegel et al. [98] used a simple Proportional and Differential (PD) feedback control scheme which incorporated their POD model. That study used transverse oscillation, moving the cylinder normal to the direction of flow, to exert control on the wake. Throughout their study, Siegel et al. [98] used the POD definition in Equation 6.21 (velocity fluctuations) and 2 domains; one for computing the overall flow and a subset of this domain immediately surrounding the cylinder to compute their POD modes. Employing an unstructured computational grid, finite difference CFD package, Siegel et al. used a sensor grid of 35 points located behind the cylinder to collect u component velocity data during simulation. The sensor grid lay completely within the region from which the POD modes are calculated in a 5 x 7 rectangular arrangement. The sensor grid data is used to calculate the modal amplitudes of the first and fifth modes (a_1 and a_5). This data used in their controller by the following relationship:

$$y_{cl} = K_p\, a_1 + K_d \frac{da_1}{dt} \tag{7.1}$$

where y_{cl} is the y position of the cylinder (or displacement), K_p is the proportional gain, K_d is the derivative gain, and a_1 is the modal amplitude of Φ^1 obtained from the POD modes calculated from u component data collected from the sensor grid. K_p and K_d are given by the following:

$$\begin{aligned} K_p &= K cos\phi \\ K_d &= \frac{K sin\phi}{2\pi f} \end{aligned} \tag{7.2}$$

where K is the an overall gain, ϕ is a fixed phase advance, and f is the vortex shedding frequency. The study also used a variable phase advance for ϕ based on a_5 [98].

A similar approach is used in this study. A grid is set up to collect u component flow field data continuously. At certain intervals, this data is used to compute modal amplitudes based on POD modes constructed for the unforced flow field (using the procedure given above). From modal amplitude a_1, the magnitude of cylinder oscillation is determined. As the rotation of the cylinder affects the flow field, u data is continuously fed back, leading to a recalculation of the modal amplitudes and the repetition of the control algorithm.

Figure 7.11 shows the orientation of the sensor grid that is used. The blue points indicate nodes of the finite element mesh used to calculate the flow profile. Data is taken from the 35 (enlarged here) red nodes to use for feedback, which are also used for the flow field calculation. As can be seen in Figure 7.11, the grid is in a roughly rectangular configuration placed up to 7 diameters behind and 1 diameter above and below the cylinder. The constant phase advance, ϕ, used is 0° or 30°, and K ranged from -0.1 to 0.1. As rotational oscillation is applied, the wake should be controlled and a_1 should subsequently be reduced and stabilized.

The data is taken from the sensor grid. The POD modes are calculated previously as outlined above. The POD modes for the unforced (stationary) case are applied

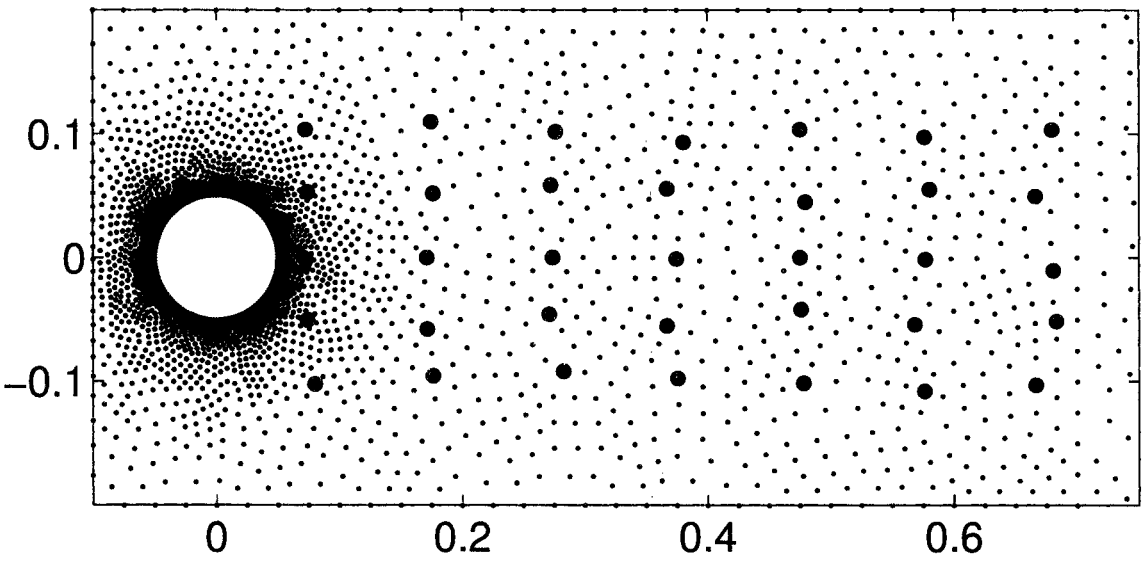

Figure 7.11: Sensor grid used for velocity feedback - blue: finite element mesh nodes used for flow computation, red: velocity sensor grid nodes.

to the forced case as in Siegel et al. [98]. As the u component data is collected from the sensors, a_1 is calculated using the vector inner product definition (Equation 6.22). Once the modal amplitude is calculated, the no-slip boundary conditions at the boundary of the cylinder are changed to the following:

$$\begin{aligned} u &= \dot{x} = yK\left(\cos\phi\,(a_1) + \frac{\sin\phi}{2\pi f}\frac{da_1}{dt}\right) \\ v &= \dot{y} = -xK\left(\cos\phi\,(a_1) + \frac{\sin\phi}{2\pi f}\frac{da_1}{dt}\right) \end{aligned} \tag{7.3}$$

These conditions can be compared to Equation 2.13, the open-loop rotational oscillation conditions. In this case, the frequency, f, is the inverse of one period of oscillation, or $f = \frac{1}{P} = 1.64$. This frequency corresponds to a non-dimensional frequency, called the Strouhal number, $St = \frac{f\,d}{U}$, of 0.16, which agrees well with the literature [91, 114].

Figure 7.12 shows the result of this feedback control algorithm as applied in this study.

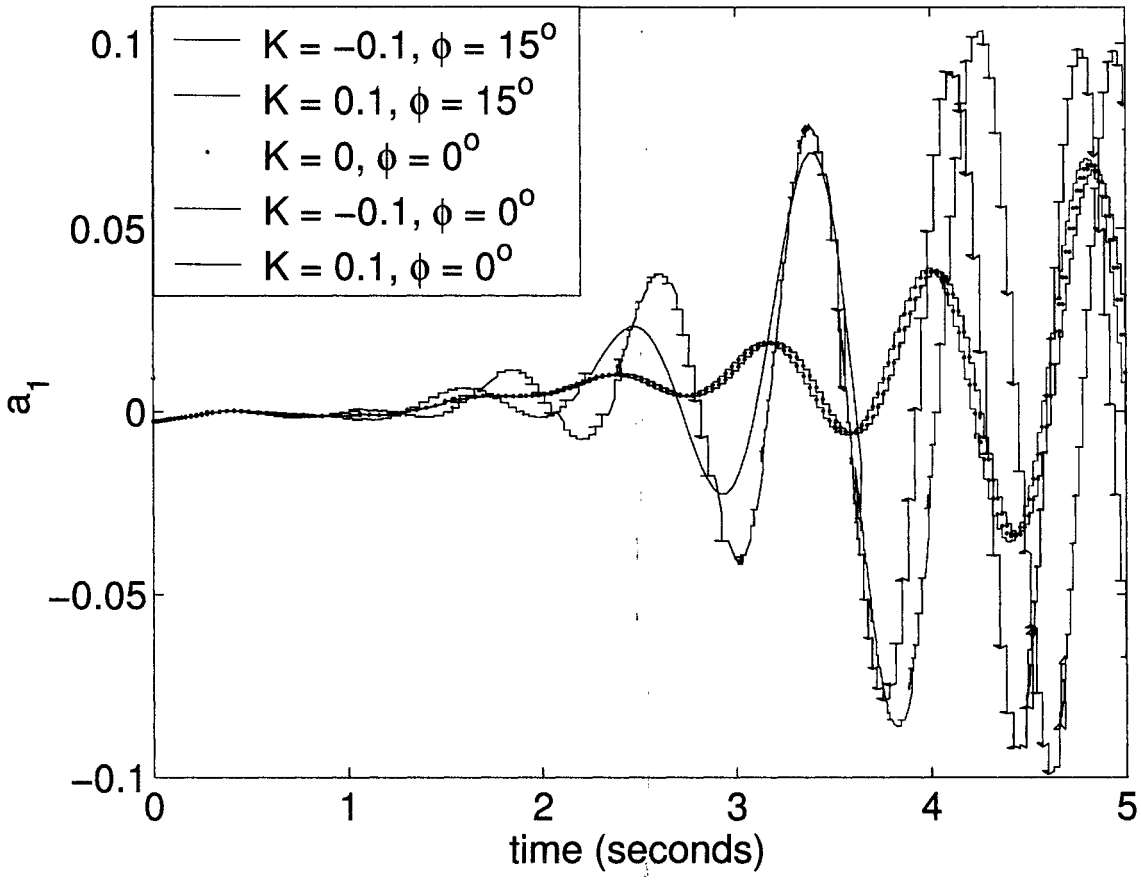

Figure 7.12: a_1 resulting from PD control algorithm.

Unlike the case in Siegel et al. [98], this control algorithm had the opposite of the desired effect. The black dotted line shows the effect of no control. The red and cyan lines show that very little difference is made by the control action if there is no phase advance. Also, the reversal of the sign of the gain makes little difference. This is to be expected since the control action applied is rotational harmonic oscillation, essentially eliciting the same response regardless of sign. The blue and green lines show that, with some phase advance and some gain, the systems actually becomes oscillatory sooner than without control or control with no phase advance. In this case, the sign of the gain does make some difference, but not a substantial one.

The difference in the result of applying the control algorithm from Siegel et al. [98] between this study and Siegel et al.'s highlights the variation between different types of actuation. Siegel et al. use transverse oscillation to exert control on the wake [98], while this study used rotational oscillation. Because these two types of actuation are fundamentally different, a control algorithm that works for one does not work for the other.

7.7 Conclusions

The modes computed by the various definitions were found to be very similar. Φ^2 through Φ^5 of the total velocity POD modes closely resembles Φ^1 through Φ^4 of the velocity fluctuations POD modes. Use of the vector inner product versus the integral inner product affects only the scale (magnitude) of the modes and modal amplitudes. The reconstruction of the flow field from the modes and modal amplitudes provides a very close duplication of the flow field from the full Navier-Stokes simulations. Two key differences between the reconstruction and the full simulation are that small-scale spatial structures are filtered out of the reconstruction and the transient state does

not appear in the reconstruction. Finally, a simple proportional derivative controller based on a previous study that successfully used transverse oscillation of the cylinder to stabilize the wake did not work in this study, where rotational oscillations are used.

Chapter 8

Reduced-Order Model Obtained with the Galerkin Projection of the Navier-Stokes Equations

8.1 Introduction

In this chapter, the output of the model obtained by the Galerkin Projection of the Navier-Stokes equations, described in Chapter 6, is examined. Three different cases of the model are evaluated using both the POD definitions given previously. For one of the cases, an alternate fifth mode is used for the velocity fluctuations POD definition. The modal amplitudes and the resulting surface plots of all of the cases for the model are examined. These are compared to the appropriate reconstructions. The effect of the pressure term on the model is examined. The model is simulated at multiple Reynolds numbers. Finally, a systematic way of implementing open-loop control with the reduced-order model is discussed.

8.2 Reduced-order model for flow around the cylinder

Following the procedure outlined in Chapter 6, a system of 10 nonlinear, coupled, ordinary differential equations (ODEs) is obtained for each POD definition. The Galerkin Projection of the Navier-Stokes equations using the POD definitions results in Equations 6.35 and 6.38. The pressure terms in Equations 6.35 and 6.38 are obtained by differentiating the pressure field data from the unforced simulation and taking the integral inner product with the appropriate modes.

Because the fifth mode for each component, Φ^5 and Ψ^5, for the set of modes defined by Equation 6.21 (velocity fluctuations) is not defined by the normalized eigenvectors of the autocorrelation matrix, but are instead defined as $\overline{u} - u_{inf}$, Φ^5 and Ψ^5 are neither orthonormal nor orthogonal. Because of this lack of orthogonality, when the inner product is taken with Equation 6.37 and Φ^k (or Ψ^k) to yield the final model equations, additional terms appear that are not shown in Equation 6.38. These additional terms are normally cancelled out when obtaining Equation 6.38 after taking the inner product because of the property of orthogonality demonstrated by Equation 6.28. In this study, these additional terms are ignored, and the model equations are written as shown in Equation 6.38, regardless of the fact that the fifth mode is not orthonormal to the other modes. These extra terms do not arise in the modes defined by Equation 6.20 because all modes are orthogonal and orthonormal with each other.

After the model is obtained, the ODEs are solved to see how the modal amplitudes evolve over time as predicted by the reduced-order model for the unforced simulation compared to the reconstruction of the modal amplitudes using Equations 6.29 and 6.30 and the flow field data obtained from solving the full Navier-Stokes equations.

For each model, a set of initial conditions are used. Each set of initial conditions is obtained from the start of each reconstruction, when the fluid is at rest. In other

words, for the total velocity POD definition (Equation 6.20), the initial conditions are taken from the start of the reconstruction with that POD definition, obtained via Equation 6.29, and so on. The integral inner product is used in each case. Three different cases are solved for the reduced-order models: 1) the total velocity POD definition, Equation 6.35, 2) the velocity fluctuations POD definition, Equation 6.38, using the fifth mode based on the average velocity, as used by Siegel et al. [98] and described in Section 7.2, and 3) the velocity fluctuations POD definition in Equation 6.38 and the alternate fifth mode described below in Section 8.3. In every case, the output of the model is shown with the corresponding reconstruction, plotted on the same scale to facilitate comparison.

The profiles of the modal amplitudes, a_i and b_i, for the total velocity POD definition (Equation 6.20) are shown in Figure 8.1. The top plots in Figure 8.1 are the modal amplitudes from the model (solution of the set of 10 ODEs shown in Equation 6.35), and the bottom plots are the modal amplitudes from the reconstruction of the data from Equation 6.29, which do not involve the solution of any ODEs. The reconstruction is the closest the model can possibly get to reproducing the output of the full Navier-Stokes equations. As shown in Figure 7.5, the reconstruction of the flow field from the modes and modal amplitudes closely resembles the output of the full simulation.

In the case of a_i shown in Figure 8.1, a_2 and a_3 from the model are very close to a_2 and a_3 from the reconstruction, both in behavior and magnitude. Qualitatively, a_4 and a_5 from the model resemble the corresponding amplitudes from the reconstruction, but the model a_4 and a_5 are significantly less than the reconstruction a_4 and a_5 in magnitude. The greatest amplitude, a_1, does not match very well between the model and the reconstruction. All the b_i, from the model qualitatively agree with the

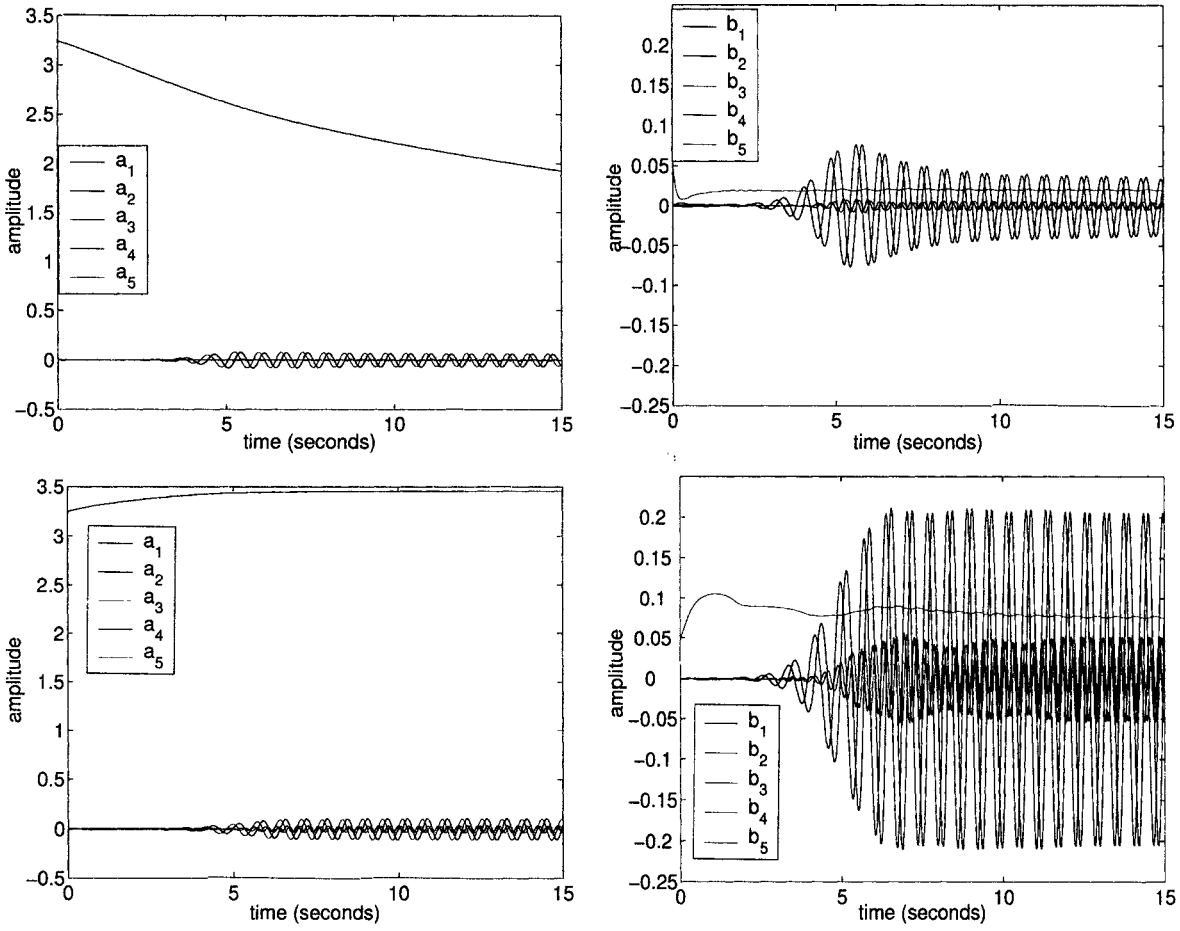

Figure 8.1: Modal amplitudes predicted by Equation 6.35 (total velocity POD definition) compared to modal amplitudes from reconstruction: Top Row, solution of model equations - Left: a_i, Right: b_i, Bottom Row, reconstruction from data - Left: a_i, Right: b_i.

reconstruction, but differ by a factor of (around) $\frac{1}{2}$ or less. It should be noted that a_1 and b_3 correspond to modes that resemble the average velocity profile for the u and v component, and, therefore, do not oscillate during the steady state as the other modal amplitudes do.

The profiles of the modal amplitudes, a_i and b_i, for the velocity fluctuations POD definition (Equation 6.21) are shown in Figure 8.2. The top plots in Figure 8.2 are the

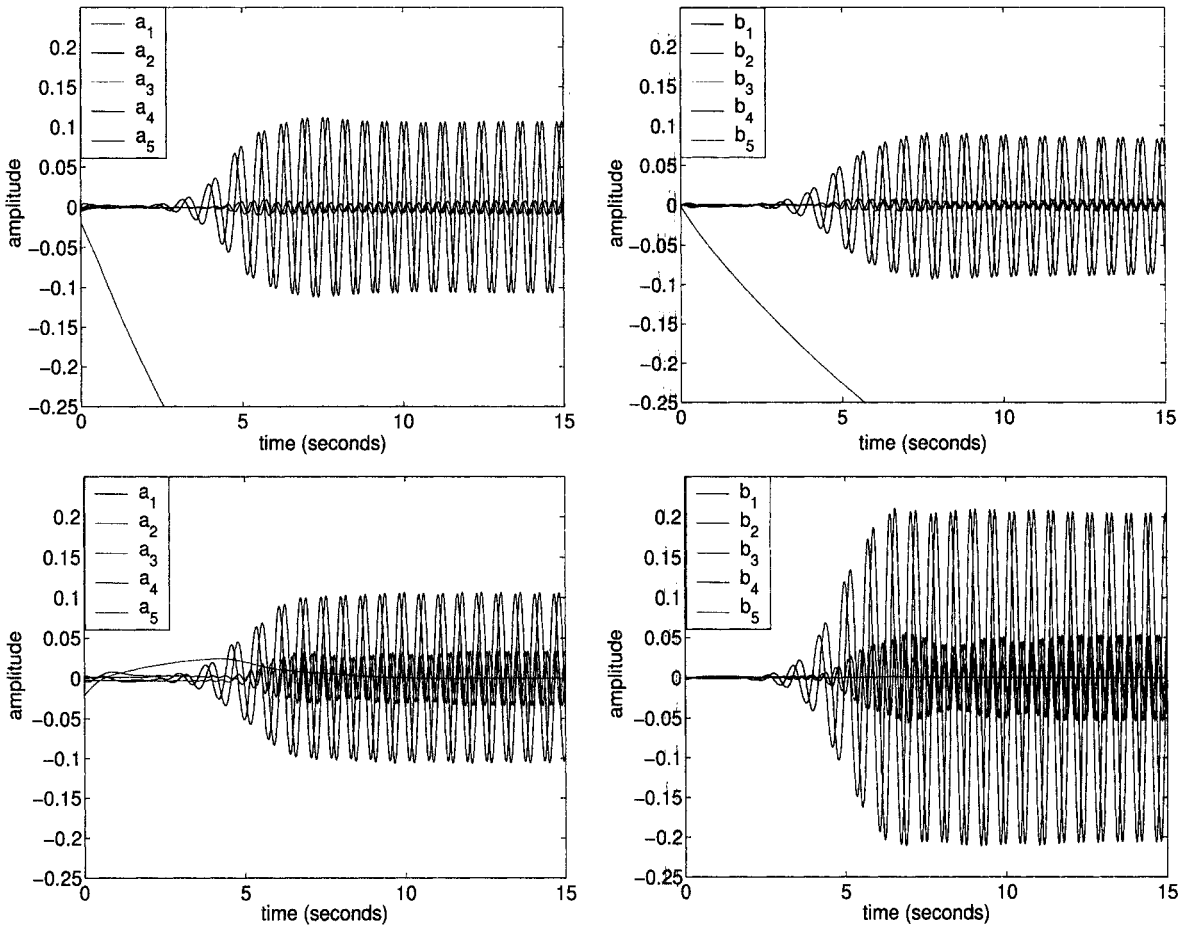

Figure 8.2: Modal amplitudes predicted by Equation 6.38 (velocity fluctuations POD definition) compared to modal amplitudes from reconstruction: Top Row, solution of model equations - Left: a_i, Right: b_i, Bottom Row, reconstruction from data - Left: a_i, Right: b_i.

modal amplitudes from the model (solution of the set of 10 ODEs shown in Equation 6.38), and the bottom plots are the modal amplitudes from the reconstruction of the

data from Equation 6.30, which do not involve the solution of any ODEs.

In the case of a_1 and a_2, the model and reconstruction are both qualitatively and quantitatively close to each other. a_3 and a_4 from the model oscillate as their counterparts in the reconstruction, but again are significantly smaller in magnitude. As in Figure 8.1, all the b_i qualitatively match the reconstruction, but are off on magnitude, except for b_5. In this case, since a_5 and b_5 correspond to modes based on $\overline{u}$ and $\overline{v}$, respectively, and are neither orthogonal nor orthonormal to the other modes, it is not surprising that the model and the reconstruction do not match here.

8.3 Alternate fifth mode for POD modes defined by velocity fluctuations

In the case of the POD definition based on velocity fluctuations (Equation 6.21), the reduced-order model may not be reproducing the flow field as accurately as possible because of the fifth mode. The fifth mode is the average velocity minus the incoming velocity. This mode does not come from the one of the eigenvectors of the autocorrelation matrix as the other four modes do. The reduced-order model, however, is based solely on the POD definition and the Galerkin projection of the Navier-Stokes equations. Since the fifth mode is not derived the same way as the other four modes, it is not appropriate for use in the reduced-order model, which is for modes defined with Equation 6.21. The extra terms that arise because of the lack of orthogonality of these modes are contributing to the error of the reduced-order model. To determine if this is the case, another set of modes are defined by using the velocity fluctuations definition of POD. In this case, Φ^5 and Ψ^5 are defined like the other four modes, instead of subtracting the incoming velocity from the average as was done before. The fifth mode comes from the fifth eigenvector, and, therefore, the fifth largest eigenvalue, of

the autocorrelation matrix.

The profiles of the modal amplitudes, a_i and b_i, for the velocity fluctuations POD definition (Equation 6.21) and the alternate fifth mode are shown in Figure 8.3. The top plots in Figure 8.3 are the modal amplitudes from the model (solution of the set

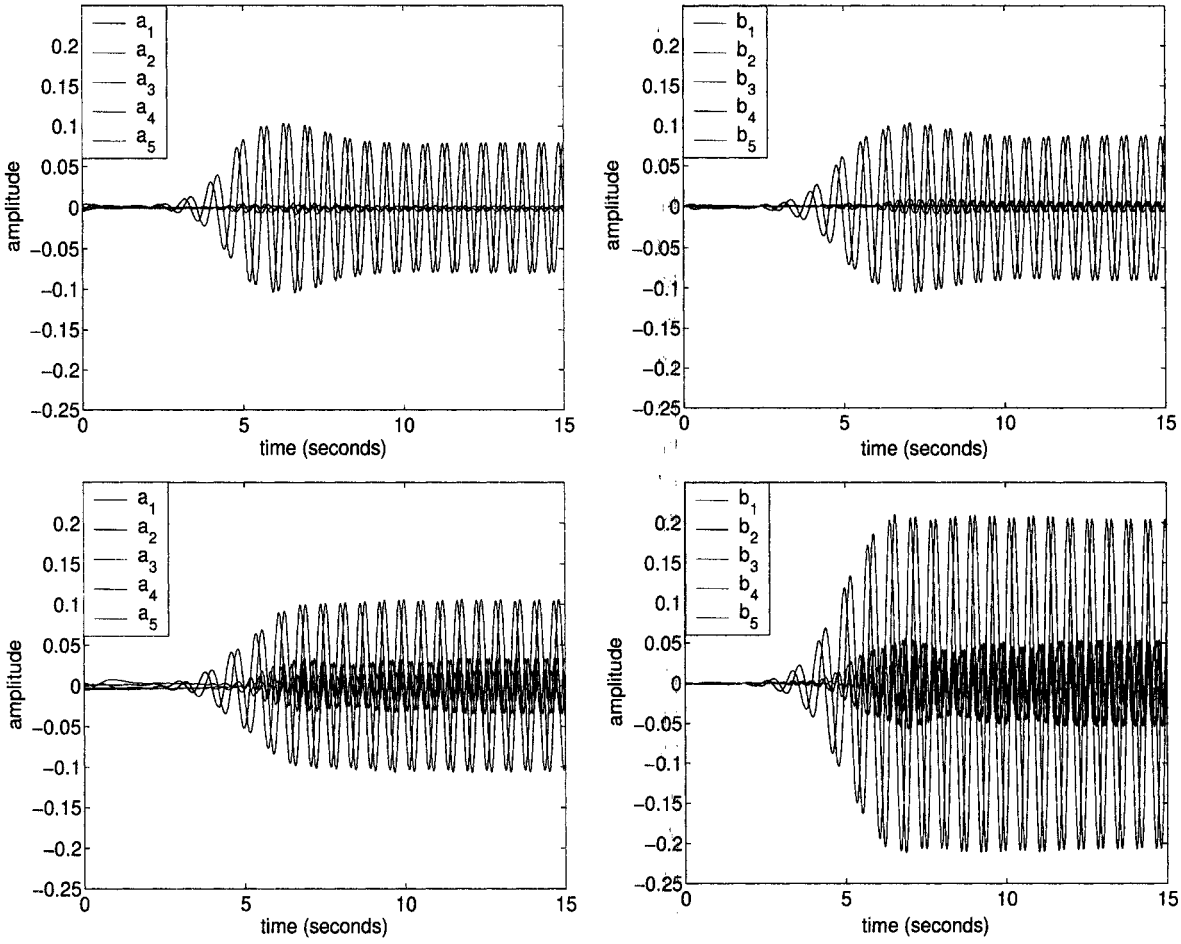

Figure 8.3: Modal amplitudes predicted by Equation 6.38 (velocity fluctuations POD definition) with alternate fifth mode compared to modal amplitudes from reconstruction: Top Row, solution of model equations - Left: a_i, Right: b_i, Bottom Row, reconstruction from data - Left: a_i, Right: b_i.

of 10 ODEs shown in Equation 6.38), and the bottom plots are the modal amplitudes from the reconstruction of the data from Equation 6.30, which do not involve the

solution of any ODEs.

In this case, a_i look very similar to b_i. Once again, a_1 and a_2 from the model look very similar, qualitatively and quantitatively, to the reconstruction. Now, a_3 through a_5 oscillate as they should, although they do not have the correct magnitude. Unlike in Figure 8.2, the fifth modal amplitude now reflects qualitatively the correct behavior as shown by the reconstruction. Similar to Figure 8.1, all b_i oscillate as they should, although not at the correct magnitude.

8.4 Reduced-order model surface plots of the velocity field

The surface plots of the flow profiles generated by the model for the three cases are shown in Figures 8.4, 8.5, and 8.6. These figures show a picture of the velocity field, for both the u component and the v components, during the steady state of the simulation for the total velocity POD definition (Equation 6.20), the velocity fluctuations POD definition (Equation 6.21) with the fifth mode defined by the average velocity as in Siegel et al. [98], and the velocity fluctuations POD definition with the fifth mode defined by the eigenvectors of the autocorrelation matrix, respectively. In each case, the surface plot of the flow field reconstructed by the appropriate POD definition is shown underneath the model surface plot. In each case, the color scale of the surface plot is determined by the appropriate reconstruction, so that each model surface plot for each component is plotted on the same color scale as the component reconstruction plot immediately below it.

The model equations do not reproduce the transient state of the flow field development. Because the system does evolve for a certain period of time before reaching the oscillatory steady state, and this evolution does not reflect the transient of the full Navier-Stokes simulation, the model is slightly out of phase with respect to the

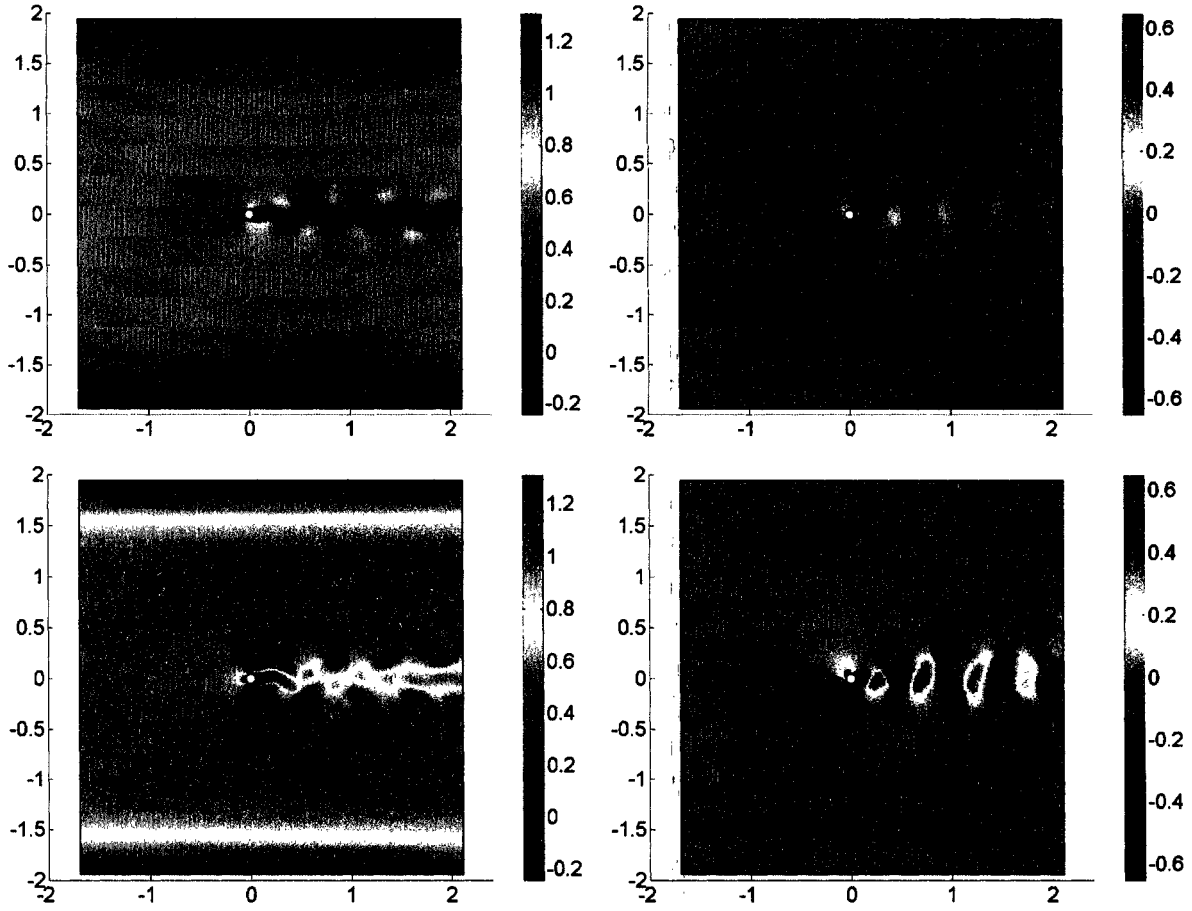

Figure 8.4: Comparing model and reconstruction, velocity component surface plots, total velocity POD definition: Top Row, model at 14.73 seconds - Left: u, Right: v, Bottom Row, reconstruction at 14.50 seconds - Left: u, Right: v.

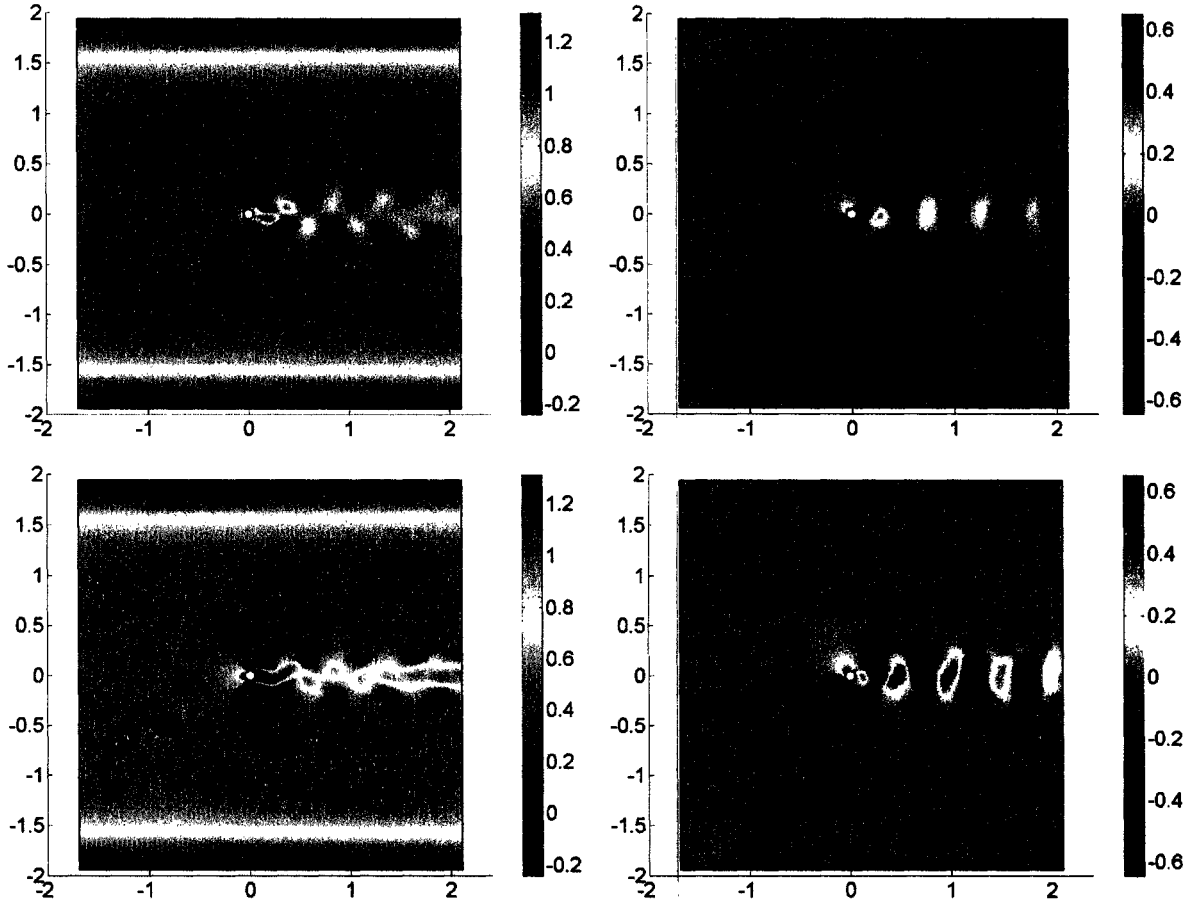

Figure 8.5: Comparing model and reconstruction, velocity component surface plots, velocity fluctuations POD definition: Top Row, model at 14.94 seconds - Left: u, Right: v, Bottom Row, reconstruction at 14.81 seconds - Left: u, Right: v.

reconstruction. Because of this difference in phase, the surface plots for the model shown in each case for Figures 8.4, 8.5, and 8.6 are not shown at the same time as the reconstruction. Instead of being shown at the same time, the surface plots are shown at the same flow state or relative point in time during the steady state period. Although the model and reconstruction are not in phase, they do have the same period, as shown by the amplitudes in Figures 8.1, 8.2, and 8.3.

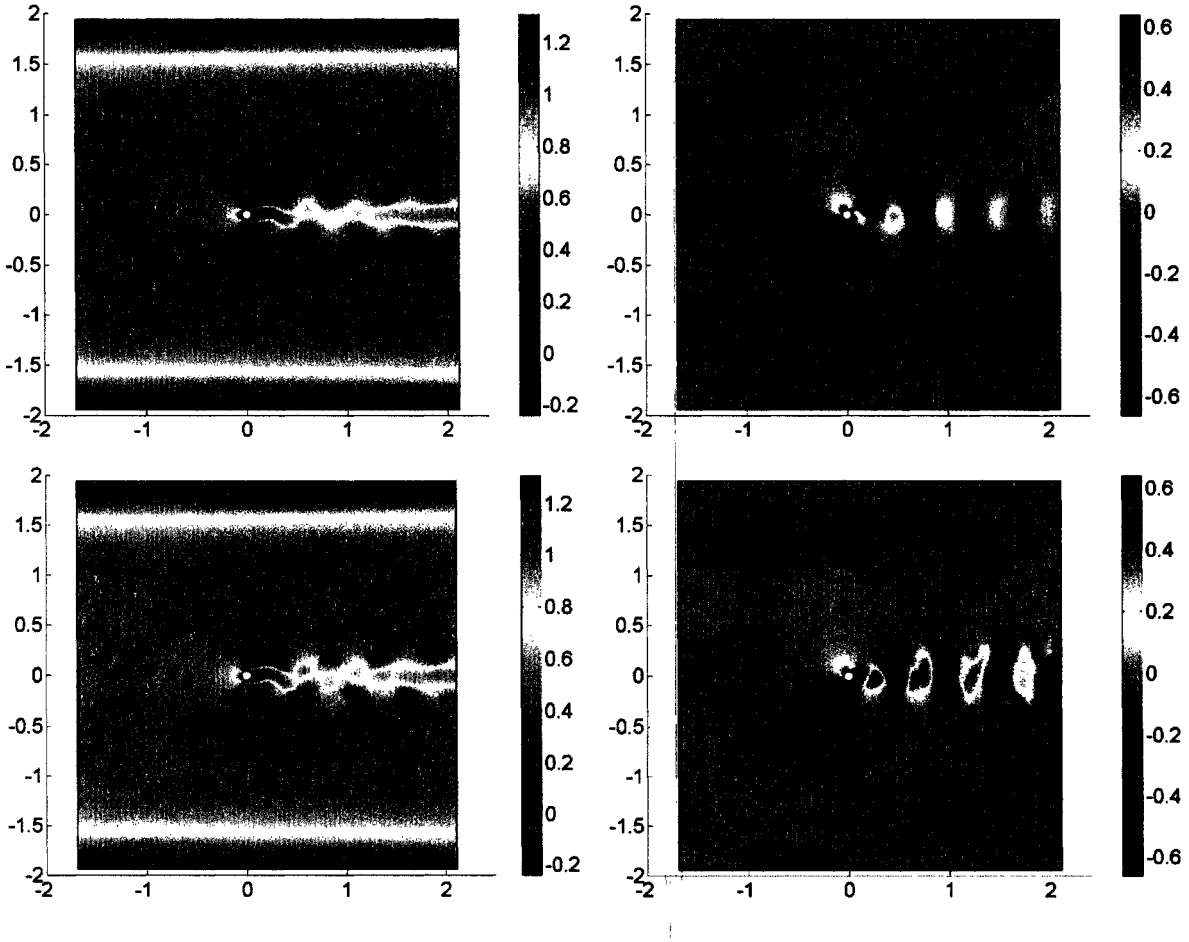

Figure 8.6: Comparing model and reconstruction, velocity component surface plots, velocity fluctuations POD definition, alternate fifth mode: Top Row, model at 14.71 seconds - Left: u, Right: v, Bottom Row, reconstruction at 14.50 seconds - Left: u, Right: v.

For the v component of velocity, the model surface plots look very much the same in each case. In the total velocity case in Figure 8.4, the overall values of v are

fairly small compared to the reconstruction. The model that most nearly matches its reconstruction is based on the velocity fluctuations POD definition with the alternate fifth mode, shown in Figure 8.6.

Overall, the model u components match their respective reconstructions more closely than the v components. In the total velocity POD definition case in Figure 8.4, the u velocity component closely matches the reconstruction u component qualitatively. In the model, the positions of the vortices along most of the von Karman vortex street, as well as the orientation of the recirculation region and the area where the first vortex is shed, correspond well to the reconstruction. However, the overall magnitude of the model velocities vary significantly from the reconstruction.

Out of the three models, the u component from the model from the velocity fluctuations POD definition, shown in Figure 8.5, is the farthest from its reconstruction. The shape of the von Karman vortex trail is incorrect and the velocity in the recirculation region is too high, relative to the rest of the flow field. The rest of the velocity field, however, is close to being quantitatively correct.

The velocity fluctuations POD definition combined with the alternate fifth mode made the best reproduction for the u component. As shown in Figure 8.6, both qualitatively and quantitatively, the model mimics the reconstruction well. The most precisely reproduced region is immediately around the cylinder, including the recirculation region and the region where the first vortex is shed.

Surface plot animations of the time-evolution of the u component of all the models show that all of the models reproduce the near-wake region (the region of the flow field immediately behind the cylinder) very well when compared to the full Navier-Stokes simulation. In all model simulations, the recirculation region (the region of low velocity behind the cylinder) moves in an oscillatory fashion just as it does in

the full simulation. Out of all the models, the best quantitative reconstruction of the near-wake region over all time for the u component is from the model based on the velocity fluctuations (Equation 6.38) using the alternate fifth mode (Figure 8.6) discussed in Section 8.3.

8.5 Comparison of simulation time

Besides providing a way of establishing a systematic way of devising a model-based control law for flow past the circular cylinder, the reduced-order model has another advantage. Computations with the reduced-order model are far faster than the full simulation. The calculation from the full simulation to produce the reduced-order model needs to be completed only one time. The reduced-order model may be used for all subsequent calculations.

The full Navier-Stokes equations require a very high-order discretization. The Navier-Stokes equations are a set of infinite-dimensional partial differential equations (PDEs), whereas the reduced-order model is only a set of 10 ordinary differential equations (ODEs). In this study, the original Navier-Stokes simulation from which data was taken contained 7360 elements. To simulate 15 seconds of the Navier-Stokes equations at Reynolds number 100, 1740 seconds of computation time are required. To simulate 15 seconds at Reynolds number 100 for the model takes only 10 seconds. This dramatic savings is a distinct advantage of the reduced-order model, where applicable, over the full simulation.

8.6 Pressure correction for the reduced-order model

The pressure term in the Galerkin projection of the Navier-Stokes equations may tend to be problematic. According to Rowley et al. [94], the pressure term in Equations 6.35 and 6.38 can be rewritten (using one of Green's identities) in the following way:

$$\langle \nabla p, \phi_k \rangle = \int_\Omega \phi_k \cdot \nabla p dV + \int_\Omega p \cdot \nabla \phi_k dV = \int_\Omega \nabla (p\phi_k) dV = \int_{\partial\Omega} p\phi_k \cdot \mathbf{n} dS \qquad (8.1)$$

where, in the second equality, the second term is zero because $\nabla\phi_k$ is zero due to the continuity equation, Equation 2.1. The pressure term, therefore, depends only the pressure and velocity at the boundaries. Rowley et al. [94] go on to point out that, if velocity is zero along any boundaries, as is the case at the top and bottom walls of the flow channel, ϕ_k is zero on those boundaries, and, therefore, the final term in Equation 8.1 is zero. If pressure is zero along a boundary, as is the case in the far field of an open flow, then the final term in Equation 8.1 is zero. If the boundary is an 'artificial' boundary, as is the case with the outlet boundary in this study, p is specified as zero [94]. Graham et al. make the same observation [55].

Holmes et al. [59], who deal with three-dimensional flow, break down the pressure term in the following way:

$$\langle \nabla p, \phi \rangle = \int_0^{X_2} \int_0^{L_3} p\phi_1 dx_3 dx_2 |_0^{L_1} + \int_0^{L_1} \int_0^{L_3} p\phi_2 dx_3 dx_1 |_0^{X_2} + \int_0^{L_1} \int_0^{X_2} p\phi_3 dx_2 dx_1 |_0^{L_3} \qquad (8.2)$$

where X_1 is the streamwise direction, X_2 is the height, X_3 is the spanwise direction, and ϕ_i denotes the mode in the i direction. In the case of the study by Holmes et al. [59], the first and third terms on the right hand side cancel because of the periodic conditions employed in the X_1 and X_3 directions. The middle term on the right hand side evaluated at zero also goes to zero because of no-slip conditions at the wall. According to Holmes et al., the middle term evaluated at X_2 remains because the

empirical eigenfunctions used in that study do not vanish at the upper edge of the wall region. This remaining term represents the relationship between the modeled wall layer and the outer region of the flow. In the case of Holmes et al., calculating with and without the $\langle \nabla p, \phi \rangle$ term distinguishes between the inner and outer influences on the dynamics in the wall layer [59].

In this study, the simulations are also conducted without the pressure terms. Figure 8.7 shows the effect of removing the pressure term on both POD definition models on a_i. It can clearly be seen that, in this case, that omitting the pressure

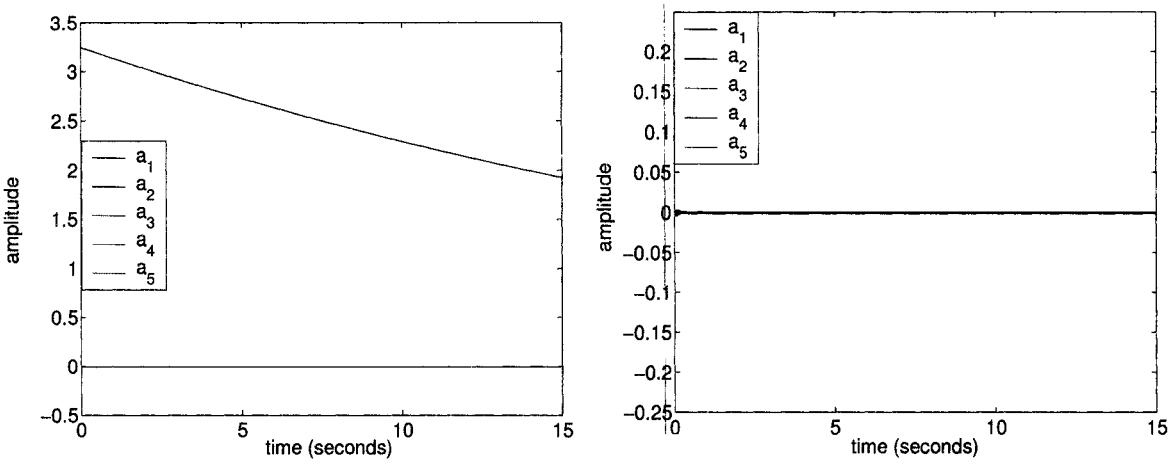

Figure 8.7: Effect of removing pressure term on modal amplitudes, a_i, from models - Left: total velocity POD definition, Right: velocity fluctuations POD definition with alternate fifth mode.

term removes almost all oscillation from the system.

8.7 Reduced-order model predictions at variable Reynolds numbers

Using the POD modes defined by Equation 6.21 (velocity fluctuations) and the alternate fifth mode described in Section 8.3, the model is simulated at several different

Reynolds numbers. The Reynolds number appears in the model equations (Equation 6.38) in two places as $\frac{1}{Re}$. In the full Navier-Stokes simulations, the vortex shedding increases as the Reynolds number increases. In the POD model, one would expect to see this manifestation of increasing Reynolds number as increasing oscillation in the modal amplitudes, a_i and b_i. In Figure 8.8, the modal amplitudes, a_i, are shown for

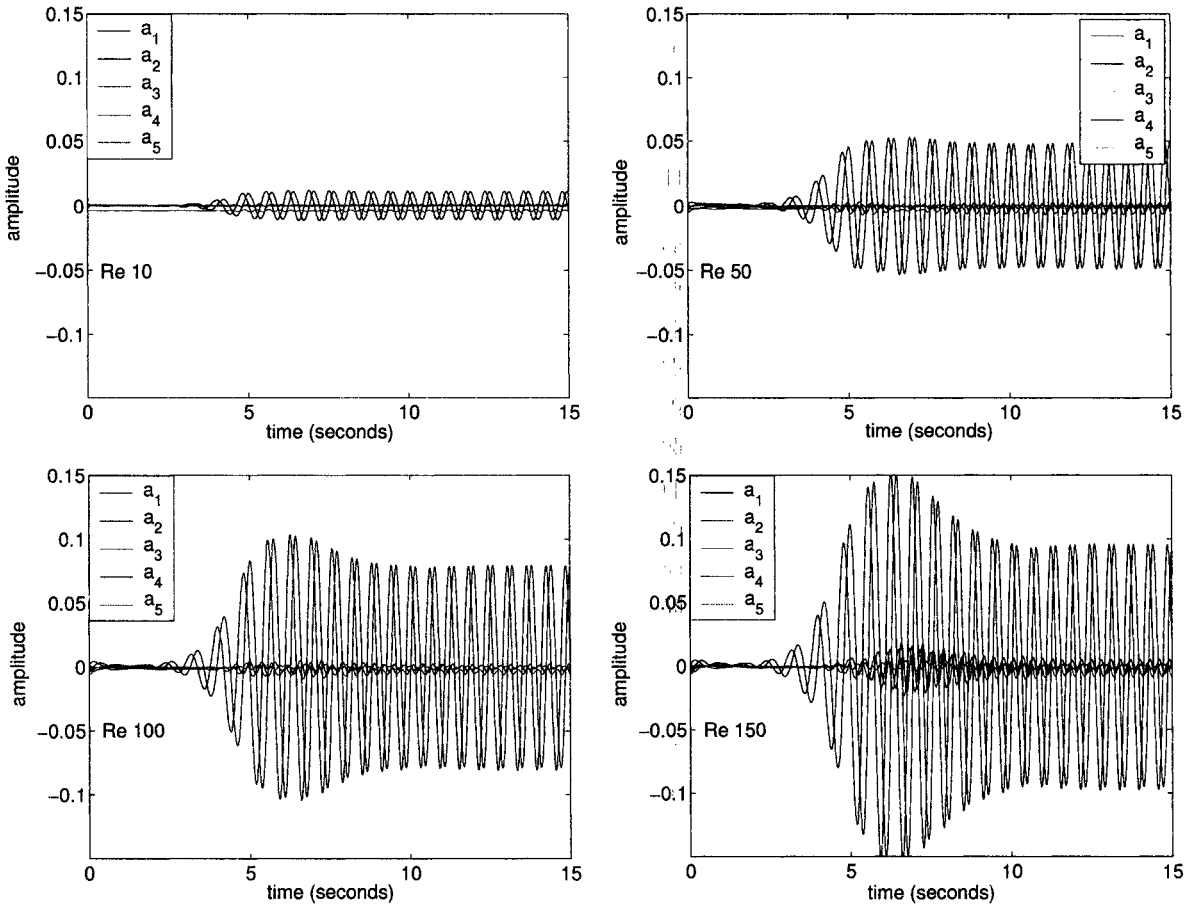

Figure 8.8: Modal amplitudes, a_i, of velocity fluctuations POD definition model with alternate fifth mode at various Reynolds number: Top Row - Left: Re = 10, Right: Re = 50, Bottom Row - Left: Re = 100, Right: Re = 150.

solutions of the model at Reynolds number 10, 50, 100, and 150. All 4 plots in Figure 8.8 are shown on the same scale. As shown in Figure 8.8, as the Reynolds number is increased, the oscillation in the modal amplitudes steadily increases, as expected.

Since vortex shedding starts at Reynolds number 47, a completely accurate model of the Navier-Stokes equations would also not exhibit shedding below Reynolds number 47. This means that modal amplitudes of the model would not oscillate below Reynolds number 47. However, as Figure 8.8 shows, at Reynolds number 10, this model still exhibits some, albeit diminished, oscillations. These oscillations come from the pressure term in Equation 6.38, $\left\langle p_x, \Phi^k \right\rangle$ and $\left\langle p_y, \Psi^k \right\rangle$. Because the pressure data is taken from the flow field at Reynolds number 100, oscillations are inherently present in this term. These oscillations are not scaled by the Reynolds number in the model since this term is not multiplied by $\frac{1}{Re}$, and, therefore, the oscillations from this term are still present at Reynolds number 10.

Surface plot animations of the time evolution of the u component of the model at Reynolds numbers 10, 50, 100, and 150 show that the vortex shedding in the near-wake region (the most accurately reproduced region in the model) occurs increasingly faster as the Reynolds increases, as expected.

8.8 Implementing open-loop control with the reduced-order model

With a modification of the cylinder boundary conditions, open-loop control can be employed, as demonstrated in Chapter 4. Using the reduced-order model, control can be employed through altering the boundary conditions also. This can be done because of the following one of Green's identities:

$$\int_\Omega w\nabla^2 u dv(\mathbf{x}) = -\int_\Omega \nabla w \cdot \nabla u dv(\mathbf{x}) + \int_{\partial\Omega} w\nabla u \cdot \mathbf{n} dA(\mathbf{x}) \tag{8.3}$$

where w and u are vectors, Ω is the domain, $\mathbf{n}$ is the unit outward normal to the boundary $\partial\Omega$, and A is the area. In this case, the second order terms in Equations

6.35 and 6.38 can be manipulated in the same way. Using the integral inner product definition, the identity from Equation 8.3 can be used to obtain the following:

$$\begin{aligned}
\langle \Phi^i_{xx}, \Phi^k \rangle &= \int_\Omega \Phi^i_{xx} \cdot \Phi^k dA &&= -\int_\Omega \Phi^i_x \cdot \Phi^k_x dA + \int_{\partial\Omega} \Phi^i_x \cdot \Phi^k \cdot n_x dx \\
&= -\langle \Phi^i_x, \Phi^k_x \rangle &&+ \langle \Phi^i_x, \Phi^k \rangle|_{\partial\Omega(1-8)} \\
\langle \Phi^i_{yy}, \Phi^k \rangle &= \int_\Omega \Phi^i_{yy} \cdot \Phi^k dA &&= -\int_\Omega \Phi^i_y \cdot \Phi^k_y dA + \int_{\partial\Omega} \Phi^i_y \cdot \Phi^k \cdot n_y dy \\
&= -\langle \Phi^i_y, \Phi^k_y \rangle &&+ \langle \Phi^i_y, \Phi^k \rangle|_{\partial\Omega(1-8)} \\
\langle \Psi^i_{xx}, \Psi^k \rangle &= -\langle \Psi^i_x, \Psi^k_x \rangle &&+ \langle \Psi^i_x, \Psi^k \rangle|_{\partial\Omega(1-8)} \\
\langle \Psi^i_{yy}, \Psi^k \rangle &= -\langle \Psi^i_y, \Psi^k_y \rangle &&+ \langle \Psi^i_y, \Psi^k \rangle|_{\partial\Omega(1-8)}
\end{aligned} \tag{8.4}$$

where $|_{\partial\Omega(1-8)}$ represents values on the boundaries, and there are 8 boundaries. Boundaries 1-4 are the flow field boundaries, and 5-8 are the cylinder boundaries. Equation 6.38 then becomes the following:

$$\begin{aligned}
\dot{a}_k = &\sum_{i=1}^{N} \left\langle \left(-\overline{u}\Phi^i_x - \overline{u}_x\Phi^i - \overline{v}\Phi^i_y \right), \Phi^k \right\rangle a_i + \sum_{i=1}^{N} \frac{1}{Re} \left(-\langle \Phi^i_x, \Phi^k_x \rangle + \langle \Phi^i_x, \Phi^k \rangle|_{\partial\Omega(1-8)} \right) a_i \\
&+ \sum_{i=1}^{N} \frac{1}{Re} \left(-\langle \Phi^i_y, \Phi^k_y \rangle + \langle \Phi^i_y, \Phi^k \rangle|_{\partial\Omega(1-8)} \right) a_i - \sum_{i=1}^{N} \left\langle \overline{u}_y \Psi^i, \Phi^k \right\rangle b_i \\
&- \sum_{i=1}^{N}\sum_{j=1}^{N} \left\langle \Phi^i \Phi^j_x, \Phi^k \right\rangle a_i a_j - \sum_{i=1}^{N}\sum_{j=1}^{N} \left\langle \Psi^i \Phi^j_y, \Phi^k \right\rangle b_i a_j \\
&+ \left\langle \left(\frac{1}{Re} \left(\overline{u}_{xx} + \overline{u}_{yy} \right) - \overline{u}\overline{u}_x - \overline{v}\overline{u}_y \right), \Phi^k \right\rangle - \left\langle p_x, \Phi^k \right\rangle \\
\dot{b}_k = &\sum_{i=1}^{N} \left\langle \left(-\overline{u}\Psi^i_x - \overline{v}_y\Psi^i - \overline{v}\Psi^i_y \right), \Psi^k \right\rangle b_i + \sum_{i=1}^{N} \frac{1}{Re} \left(-\langle \Psi^i_x, \Psi^k_x \rangle + \langle \Psi^i_x, \Psi^k \rangle|_{\partial\Omega(1-8)} \right) b_i \\
&+ \sum_{i=1}^{N} \frac{1}{Re} \left(-\langle \Psi^i_y, \Psi^k_y \rangle + \langle \Psi^i_y, \Psi^k \rangle|_{\partial\Omega(1-8)} \right) b_i - \sum_{i=1}^{N} \left\langle \overline{v}_x \Phi^i, \Psi^k \right\rangle a_i \\
&- \sum_{i=1}^{N}\sum_{j=1}^{N} \left\langle \Psi^i \Psi^j_y, \Psi^k \right\rangle b_i b_j - \sum_{i=1}^{N}\sum_{j=1}^{N} \left\langle \Phi^i \Psi^j_x, \Psi^k \right\rangle a_i b_j \\
&+ \left\langle \left(\frac{1}{Re} \left(\overline{v}_{xx} + \overline{v}_{yy} \right) - \overline{u}\overline{v}_x - \overline{v}\overline{v}_y \right), \Psi^k \right\rangle - \left\langle p_y, \Psi^k \right\rangle
\end{aligned} \tag{8.5}$$

In the same manner as shown in Chapter 4, open-loop control of the flow past the cylinder can by implemented be specifying an oscillating velocity on the cylinder

boundaries. Previously, open-loop control was implemented by setting the cylinder boundary conditions to the following:

$$\begin{aligned} u|_{\partial\Omega(5-8)} &= yA\sin(2\pi ft) \\ v|_{\partial\Omega(5-8)} &= -xA\sin(2\pi ft) \end{aligned} \tag{8.6}$$

The cylinder boundary velocities are also equal to the following:

$$\begin{aligned} u|_{\partial\Omega(5-8)} &= \sum_{i=1}^{N} a_i \Phi^i|_{\partial\Omega(5-8)} \\ v|_{\partial\Omega(5-8)} &= \sum_{i=1}^{N} b_i \Psi^i|_{\partial\Omega(5-8)} \end{aligned} \tag{8.7}$$

In the data set that was used to generate the empirical eigenfunction bases, Φ^i and Ψ^i, the cylinder had stationary (no-slip) boundaries. Therefore, $u|_{\partial\Omega(5-8)}$ and $v|_{\partial\Omega(5-8)}$ were zero. A data set with the time-varying boundary conditions specified in Equation 8.6 would not be within the span of the original empirical eigenfunction bases obtained in Section 7.2. In order to implement open-loop control, the procedure described in Section 6.5 must be repeated to obtain new empirical eigenfunction bases with data from a simulation that has the boundary conditions specified in Equation 8.6. The model equations obtained from the Galerkin Projection of the Navier-Stokes Equation (Equations 6.35 and 6.38) will be the same; only the new POD modes must be used, and, therefore, the values of the coefficients of the model equations will change.

The forcing term in Equation 8.7 will have different modal amplitudes, a_i and b_i, than the rest of the system. If the forcing amplitudes of the cylinder boundary are a_i^f and b_i^f, than the model equations with the open-loop forcing term will take the

following form:

$$\begin{aligned}
\dot{a}_k = &\sum_{i=1}^{N}\left\langle\left(-\overline{u}\Phi_x^i - \overline{u}_x\Phi^i - \overline{v}\Phi_y^i\right),\Phi^k\right\rangle a_i + \sum_{i=1}^{N}\frac{1}{Re}\left(-\langle\Phi_x^i,\Phi_x^k\rangle + \langle\Phi_x^i,\Phi^k\rangle|_{\partial\Omega(1-8)}\right)a_i \\
&+\sum_{i=1}^{N}\frac{1}{Re}\left(-\langle\Phi_y^i,\Phi_y^k\rangle + \langle\Phi_y^i,\Phi^k\rangle|_{\partial\Omega(1-8)}\right)a_i - \sum_{i=1}^{N}\left\langle\overline{u}_y\Psi^i,\Phi^k\right\rangle b_i \\
&-\sum_{i=1}^{N}\sum_{j=1}^{N}\left\langle\Phi^i\Phi_x^j,\Phi^k\right\rangle a_i a_j - \sum_{i=1}^{N}\sum_{j=1}^{N}\left\langle\Psi^i\Phi_y^j,\Phi^k\right\rangle b_i a_j \\
&+\left\langle\left(\frac{1}{Re}\left(\overline{u}_{xx}+\overline{u}_{yy}\right) - \overline{u}\overline{u}_x - \overline{v}\overline{u}_y\right),\Phi^k\right\rangle - \left\langle p_x,\Phi^k\right\rangle + \sum_{i=1}^{N}\left\langle\Phi^i,\Phi^k\right\rangle|_{\partial\Omega(5-8)}a_i^f \\
\dot{b}_k = &\sum_{i=1}^{N}\left\langle\left(-\overline{u}\Psi_x^i - \overline{v}_y\Psi^i - \overline{v}\Psi_y^i\right),\Psi^k\right\rangle b_i + \sum_{i=1}^{N}\frac{1}{Re}\left(-\langle\Psi_x^i,\Psi_x^k\rangle + \langle\Psi_x^i,\Psi^k\rangle|_{\partial\Omega(1-8)}\right)b_i \\
&+\sum_{i=1}^{N}\frac{1}{Re}\left(-\langle\Psi_y^i,\Psi_y^k\rangle + \langle\Psi_y^i,\Psi^k\rangle|_{\partial\Omega(1-8)}\right)b_i - \sum_{i=1}^{N}\left\langle\overline{v}_x\Phi^i,\Psi^k\right\rangle a_i \\
&-\sum_{i=1}^{N}\sum_{j=1}^{N}\left\langle\Psi^i\Psi_y^j,\Psi^k\right\rangle b_i b_j - \sum_{i=1}^{N}\sum_{j=1}^{N}\left\langle\Phi^i\Psi_x^j,\Psi^k\right\rangle a_i b_j \\
&+\left\langle\left(\frac{1}{Re}\left(\overline{v}_{xx}+\overline{v}_{yy}\right) - \overline{u}\overline{v}_x - \overline{v}\overline{v}_y\right),\Psi^k\right\rangle - \left\langle p_y,\Psi^k\right\rangle + \sum_{i=1}^{N}\left\langle\Psi^i,\Psi^k\right\rangle|_{\partial\Omega(5-8)}b_i^f
\end{aligned} \tag{8.8}$$

Open-loop control may be implemented with Equation 8.8, where the open-loop forcing is represented in Equation 8.8 by $\sum_{i=1}^{N}\left\langle\Phi^i,\Phi^k\right\rangle|_{\partial\Omega(5-8)}a_i^f$ for u and $\sum_{i=1}^{N}\left\langle\Psi^i,\Psi^k\right\rangle|_{\partial\Omega(5-8)}b_i^f$ for v. Equation 8.8 has the general form $\dot{x}(t) = f(x(t)) + g(x(t))u(t) \quad y = h(x)$, where the forcing term $g(x(t))$ is the forcing term shown above. The forcing term may also be a function of the state, and a closed-loop control can replace $g(x(t))$. In this manner, closed-loop control can be implemented through the reduced order model.

8.9 Conclusions

Three different cases of a reduced-order model for flow past the circular cylinder were examined. The models were obtained by the Galerkin Projection of the Navier-Stokes equations. Both POD definitions (total velocity and velocity fluctuations) were used.

For the velocity fluctuations POD definition, where the fifth mode had been defined by the average velocity, an alternate fifth mode was used in one case. This alternate fifth mode was computed from the fifth eigenvector of the autocorrelation matrix, defined just as the other four modes were defined. For the three cases, the modal amplitudes predicted by the three model equations were examined, together with the surface velocity plots from a point in time when the model is in the periodic steady state. It was found that, both for the modal amplitudes and the surface velocity plots, the velocity fluctuations POD definition with the alternate fifth mode reproduce the full simulation quite closely, especially in terms of the surface velocity plot for the u component. It was demonstrated that the pressure term is necessary for the model equations. The reduced-order model was run for a range of Reynolds numbers. It was found that the oscillations of the modal amplitudes grow steadily as the Reynolds number is increased, as expected. It was also noted that the model exhibits oscillations at Reynolds number 10, where there should be no oscillation, because of the fluctuation inherent in the pressure term. Finally, it was shown that rotational oscillation of the cylinder can be achieved in the reduced-order model, allowing both open-loop and closed-loop control of the cylinder.

Chapter 9

Control of Flow Over a Flat Plate

9.1 Introduction

In this chapter, two-dimensional incompressible Newtonian fluid flow over a flat plate is considered and the problem of reducing the frictional drag exerted on the plate using active feedback control is examined. Refer to Figure 9.1 for a schematic of the problem. Several alternative control configurations, including both pointwise and

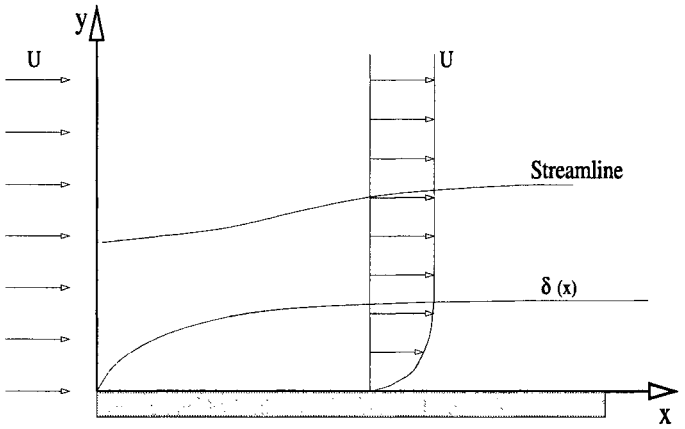

Figure 9.1: Flow over a flat plate.

spatially uniform control actuation and sensing, are developed and tested through computer simulations. All control configurations use control actuation in the form

of blowing/suction on the plate and measurements of shear stresses along the plate. The simulation results indicate that the use of active feedback control, which employs reasonable control effort, can significantly reduce the frictional drag exerted on the plate compared to the open-loop values.

9.2 Geometry, equations, boundary conditions

Two-dimensional incompressible Newtonian fluid flow with uniform velocity, which is equal to a constant U_0, over a flat plate of length L is considered. The exact dimensions of the rectangular domain used for this fluid dynamic system and the (x, y) axes specification used in all of our calculations are shown in Figure 9.2. Because of sym-

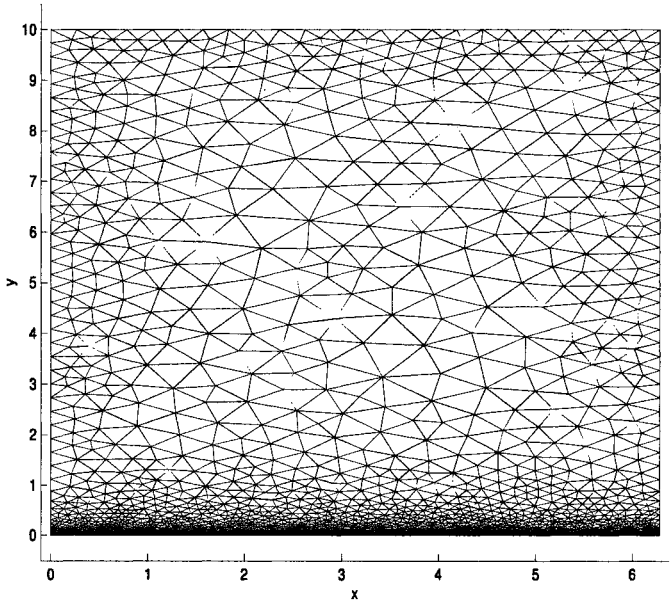

Figure 9.2: Spatial domain and finite-element mesh for flow over a flat plate.

metry, only one half (the upper half) of the geometry is generated. The dimensional

Navier-Stokes equations that describe the flow field take the following form:

$$\begin{aligned} \frac{\partial u}{\partial x} + \frac{\partial v}{\partial y} &= 0 \\ \frac{\partial u}{\partial t} + u\frac{\partial u}{\partial x} + v\frac{\partial u}{\partial y} &= -\frac{1}{\rho}\frac{\partial P}{\partial x} + \nu\frac{\partial^2 u}{\partial x^2} + \nu\frac{\partial^2 u}{\partial y^2} \\ \frac{\partial v}{\partial t} + u\frac{\partial v}{\partial x} + v\frac{\partial v}{\partial y} &= -\frac{1}{\rho}\frac{\partial P}{\partial y} + \nu\frac{\partial^2 v}{\partial x^2} + \nu\frac{\partial^2 v}{\partial y^2} \end{aligned} \tag{9.1}$$

where, as before, u and v are the components of the velocity along the x and y axes, respectively, P is the pressure, ρ is the fluid density, and ν is the kinematic viscosity. The above equations are considered subject to the following set of boundary conditions:

$$\begin{aligned} u(0,y,t) = U_0, \quad v(0,y,t) = 0 \\ u(x,0,t) = 0, \quad v(x,0,t) = C(x,t) \\ n_x u(x,10,t) + n_y v(x,10,t) = 0 \end{aligned} \tag{9.2}$$

where $C(x,t)$ is the control input that will be determined in the next section and (n_x, n_y) are the components of the vector normal to the boundary (i.e., $\mathbf{n} = n_x\mathbf{i} + n_y\mathbf{j}$). Note that $v(x,0,t) = C(x,t)$ is motivated by our desire to control the flow using vertical blowing/suction. For the open-loop system (i.e., $C(x,t) = 0$), the first two boundary conditions imply that the flow towards the plate is uniform, the next two boundary conditions correspond to no-slip on the plate, and the last boundary condition accounts for the fact that far from the plate the flow should be uniform. In addition, since the profile of the flow in the outlet of the plate is unknown, following [86, 92] a free boundary condition as before in Chapter 2 is employed in the outlet and the outlet pressure $P(6.3, y)$ is set equal to one.

Using the FEMLAB simulation environment again, a very fine mesh to compute the solution of the flow field as described by the dynamic Navier-Stokes of Equations 9.6-9.8 is constructed; further increase in the number of discretization elements and decrease of the step of the temporal integration did not influence the results. The exact form of the spatial discretization mesh used in our calculations for both the

open-loop and the closed-loop system is shown in Figure 9.2. It is important to note that the finer structure of the mesh towards the plate is motivated by the presence of the plate which leads to significant velocity gradients close to the plate and of our closed-loop calculations (to be presented in the next section) that require a finer mesh close to the area where feedback control is applied to the system to maintain a mesh-independent solution. The last requirement is a result of the modification of the value of $C(x,t)$ from 0 for the open-loop system to an expression that is a function of the state of the system in the case of the closed-loop system. To be able to make meaningful comparisons for the frictional drag profiles along the plate, the same mesh structure is used for the open-loop and closed-loop simulations. Moreover, the height of the computational domain is taken to be about 30 times the thickness of the boundary layer (see Figure 9.3) to remove boundary effects to and ensure quick convergence and accuracy of the solution. Figures 9.3 and 9.4 show the steady-state

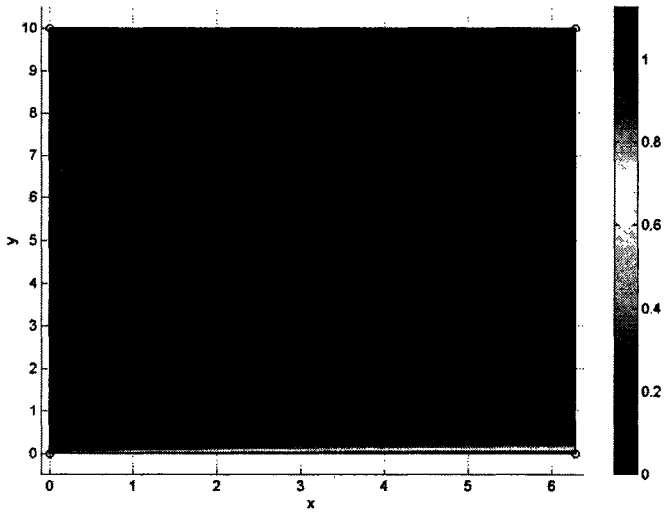

Figure 9.3: Steady state open-loop velocity profile for flow over flat plate for the entire domain.

open-loop velocity (each point in the plot represents the value of $\sqrt{u^2+v^2}$) profiles for the entire domain and close to the plate, respectively, for $Re = 50,000$; one can

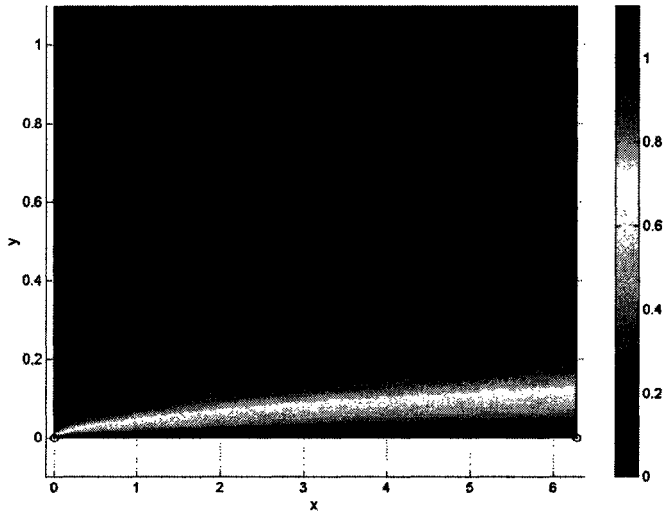

Figure 9.4: Steady state open-loop velocity profile for flow over flat plate close to the plate.

see the development of a laminar boundary layer over the plate. This is expected since for $Re = 50,000$ the boundary layer over the plate is stable [12, page 313]. The reason for which the time axis starts from 30 time units is that it takes 30 time units for the flow to stabilize at the laminar boundary layer configuration; this time axis specification will facilitate the comparisons between the open-loop and closed-loop system drag profiles. The computation of the pressure gradients $\frac{\partial P}{\partial x}$ and $\frac{\partial P}{\partial y}$ gave very small values for these two quantities everywhere in the flow field; this is expected in the case of uniform external flow. Furthermore, because of the very fine mesh used in our calculations, the velocity close to the inlet is found to be uniform and equal to U_0 (except from the plate where it is zero), thereby eliminating the need to expand the computational domain to some small distance before the leading edge of the plate to achieve uniform flow in the inlet of the computational domain.

Since the objective of this work is to investigate the effect of feedback control (i.e., different choices for $C(x,t)$) on the frictional drag exerted on the plate (i.e., integral along x of the tangential force per unit area exerted on the plate by the

fluid), the results are presented in terms of the quantity $\partial u/\partial y$ at $y = 0$ which is directly proportional to the frictional drag; the drag exerted on the two sides of unit width of a plate of length L is:

$$D = 2\int_0^L \mu \left(\frac{\partial u}{\partial y}\right)_{y=0} dx \tag{9.3}$$

Figure 9.5 shows the spatio-temporal profile of $\partial u/\partial y$ at $y = 0$, over a flat plate for the open-loop (i.e., $C(x,t) = 0$) steady-state flow field. As expected for steady-state

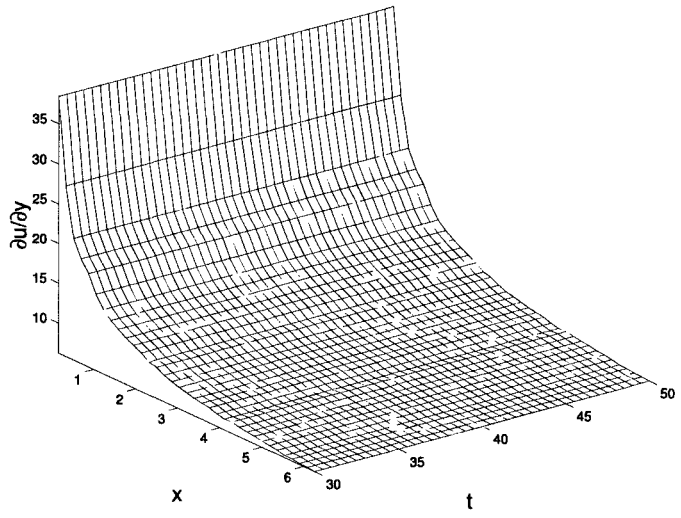

Figure 9.5: Spatio-temporal profile of $\left(\frac{\partial u}{\partial y}\right)_{y=0}$ for $C(x,t) = 0$.

laminar boundary layer, $\left(\frac{\partial u}{\partial y}\right)_{y=0}$ exhibits its maximum close to the edge of the plate.

Because of the consideration of an external flow field with $U = U_0 = constant$, the possibility of separation of the flow from the plate at a certain position downstream does not exist. Flow separation can occur when the external flow accelerates/decelerates; active feedback control of flow separation is a subject currently studied by our group but it is outside of the scope of the present paper. Because of the lack of flow separation, $\left(\frac{\partial u}{\partial y}\right)_{y=0}$ is always positive for both the open-loop and closed-loop systems.

The validity of the boundary condition $u(x, 10, t) = U_0, \quad v(x, 10, t) = 0$ on the top side of the computational domain is established. The boundary condition leads to identical results to the ones of the slip boundary condition, $n_x u(x, 10, t) + n_y v(x, 10, t) = 0$ used in the calculations reported in this chapter. This is a consequence of the fact that the height of the computational domain is much larger than the thickness of the boundary layer.

The approximate steady-state boundary layer equations for laminar flow over flat plate are reviewed and the resulting analytic expression of the frictional drag per unit area of the plate at distance x from the leading edge is provided (the reader may refer to [12] for more discussion on this subject). To proceed with this task, the pressure gradient $\frac{\partial P}{\partial x}$ is evaluated outside of the boundary layer. At the edge of the boundary layer using Euler's equation for the incident irrotational flow and using a no-penetration condition, the following is true:

$$-\frac{1}{\rho}\frac{\partial P}{\partial x} = \frac{\partial U}{\partial t} + U\frac{\partial U}{\partial x} \tag{9.4}$$

where U represents the known tangential component of the velocity of the outer flow. For uniform flow outside of the boundary layer, it follows directly from Equation 9.4 that $U = U_0$ implies $\frac{\partial P}{\partial x} = 0$.

To proceed with the derivation of the approximate steady-state boundary layer equations, a more natural coordinate system in which lateral distances are measured and velocities are measured with the (representative) boundary layer thickness as the unit length is needed; this will allow to state clearly the main assumptions involved in this approximation. To this end, the following dimensionless quantities are defined:

$$\begin{gathered} \bar{x} = \frac{x}{L}, \quad \bar{y} = Re^{0.5}\frac{y}{L}, \quad \bar{t} = \frac{tU_0}{L}, \\ \bar{u} = \frac{u}{U_0}, \quad \bar{v} = Re^{0.5}\frac{v}{U_0}, \quad \bar{P} = \frac{P - P_0}{\rho U_0^2} \end{gathered} \tag{9.5}$$

where L represents a distance in the x-direction over which u changes appreciably and P_0 is the value of P at some convenient reference point in the fluid. Using these new variables, the Navier-Stokes equations of Equation 9.1 with $\frac{\partial \bar{P}}{\partial \bar{x}} = 0$ that describe the flow field take the form:

$$\begin{aligned} \frac{\partial \bar{u}}{\partial \bar{x}} + \frac{\partial \bar{v}}{\partial \bar{y}} &= 0 \\ \frac{\partial \bar{u}}{\partial \bar{t}} + \bar{u}\frac{\partial \bar{u}}{\partial \bar{x}} + \bar{v}\frac{\partial \bar{u}}{\partial \bar{y}} &= \frac{1}{Re}\frac{\partial^2 \bar{u}}{\partial \bar{x}^2} + \frac{\partial^2 \bar{u}}{\partial \bar{y}^2} \\ \frac{1}{Re}\left(\frac{\partial \bar{v}}{\partial \bar{t}} + \bar{u}\frac{\partial \bar{v}}{\partial x} + \bar{v}\frac{\partial \bar{v}}{\partial \bar{y}}\right) &= -\frac{\partial \bar{P}}{\partial \bar{y}} + \frac{1}{Re^2}\frac{\partial^2 \bar{v}}{\partial \bar{x}^2} + \frac{1}{Re}\frac{\partial^2 \bar{v}}{\partial \bar{y}^2} \end{aligned} \tag{9.6}$$

The approximate steady-state laminar boundary layer equations can be obtained under the assumptions that $Re \rightarrow \infty$ and the magnitude of $\frac{\partial u}{\partial x}$ is small compared with that of $\frac{\partial u}{\partial y}$ and have the form:

$$\begin{aligned} \frac{\partial \bar{u}}{\partial \bar{x}} + \frac{\partial \bar{v}}{\partial \bar{y}} &= 0 \\ \bar{u}\frac{\partial \bar{u}}{\partial \bar{x}} + \bar{v}\frac{\partial \bar{v}}{\partial \bar{y}} &= \frac{\partial^2 \bar{u}}{\partial \bar{y}^2}, \quad 0 = -\frac{\partial \bar{P}}{\partial \bar{y}} \end{aligned} \tag{9.7}$$

The above equations are subjected to the following set of boundary conditions:

$$\begin{aligned} \bar{u}(\bar{x}, 0, \bar{t}) = 0, \quad \bar{v}(\bar{x}, 0, \bar{t}) = \bar{C}(\bar{x}, \bar{t}) \\ \bar{u}(\bar{x}, 0, \bar{t}) \rightarrow 1 \; as \; \frac{\bar{y}}{\delta_0} \rightarrow \infty \end{aligned} \tag{9.8}$$

where δ_0 is a small length representative of the boundary layer thickness. The solution of Eqs.9.7-9.8 can be obtained with appropriate similarity transformations and leads to the following expression for the frictional force per unit area of the plate (expressed in terms of the original coordinates) at distance x from the leading edge [12]:

$$\mu\left(\frac{\partial u}{\partial y}\right)_{y=0} = 0.33\rho U_0^2 Re^{-0.5}\left(\frac{x}{L}\right)^{-0.5} \tag{9.9}$$

which clearly implies that $\left(\frac{\partial u}{\partial y}\right)_{y=0}$ attains its maximum at the leading edge of the plate and decreases to zero as x increases. Note that the calculation of the frictional

drag of Equation 9.9 is not valid if the flow in the boundary layer is not laminar (unstable flow occurs for Re greater than 1.2×10^5 [12, page 313] which is significantly above the value of $Re = 5 \times 10^4$ considered in our simulations) over the whole surface of the flat plate. In the case of unstable flow, disturbances in the boundary layer grow and a transition to a different type of flow occurs at some distance downstream. The frictional force at the wall in such a turbulent boundary layer is considerably larger than that in a laminar boundary layer with the same external stream speed, because the random cross-currents in the boundary layer carry the fast moving fluid in the outer layers into the neighborhood of the wall and are more effective in promoting lateral transport than molecular diffusion.

9.3 Control laws - closed-loop simulations

Several alternative control configurations (i.e., different actuation/measurement structures) which use wall shear stress measurements and apply blowing/suction type of control actuation to reduce the frictional drag exerted on the plate are developed. All control configurations utilize linear proportional control laws to compute the control action. More specifically, in the case of pointwise measurement/actuation, the control law is of the type $C(x_i,t) = K\left(\frac{\partial u}{\partial y}\right)(x_i,0,t)$, where K is the controller gain and x_i is the location of actuation, while in the case of spatially-uniform control actuation, the control law is of the type $C(t) = K\int_0^L s(x)\left(\frac{\partial u}{\partial y}\right)(x,0,t)\,dx$, where $s(x)$ is a function which depends on the type of measurements (pointwise, distributed) that are available for feedback. The simple structure of the above feedback laws is motivated by the following three reasons: a) the objective of this study is to see whether it is possible to reduce frictional drag with any type (in particular the simplest) of active feedback control, b) the design of Navier-Stokes-based feedback controls is not

an easy task because of the complexity of the flow field under consideration, while the on-line implementation of such controls would require significant computational power which may not always be available, and c) the practical implementation of the above linear control laws requires relatively less computational and hardware resources. The value of the controller gain K is chosen, through trial and error, to achieve a reasonable reduction in frictional drag and to avoid perturbing the laminar nature of the flow field in the domain of definition of the flow. In all the simulation runs discussed below, $Re = 50,000$.

Initially, fully localized control configuration which uses the value of the wall shear stress at any given point along the plate to determine the amount of blowing/suction (i.e., value of the vertical component of the velocity) at the corresponding point on the plate is tested. Mathematically, the control law for this case can be expressed as:

$$v(x_i, 0, t) = C(x_i, t) = K \left(\frac{\partial u}{\partial y} \right) (x_i, 0, t), \quad i = 1, \ldots, N \tag{9.10}$$

where $K = 0.005$ and $N = 350$ is the number of discretization points used on the plate.

Figure 9.6 shows the spatio-temporal profile of $\left(\frac{\partial u}{\partial y} \right)_{y=0}$ starting from initial conditions of the steady state open-loop simulation. Again as in the open-loop simulations, the time axis starts from 30 time units; this is the time needed for the flow to reach the steady-state solution of the open-loop system and $t = 30$ is the time in which the control system is activated. As can be seen in Figure 9.6, this control configuration does a very good job in reducing the frictional drag compared to the open-loop operation (compare the profile of Figure 9.6 with the corresponding open-loop profile of Figure 9.5). Figure 9.7 shows the spatio-temporal profile of the wall-normal velocity, $v(x, 0, t)$, which is the manipulated input. Clearly, the value of $v(x, 0, t)$ is small and positive for all times which means that blowing is applied to the

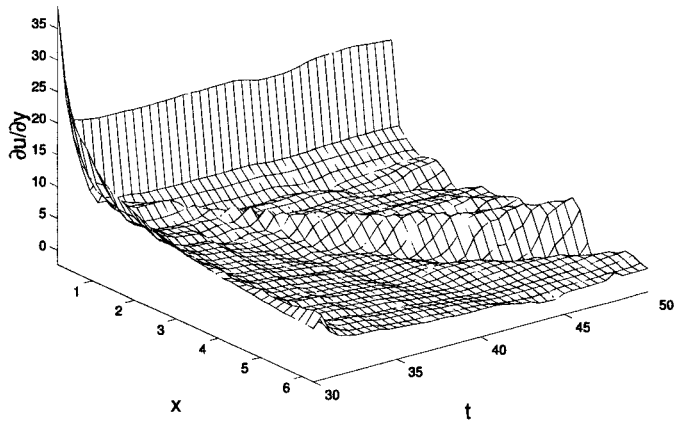

Figure 9.6: Spatio-temporal profile of $\left(\frac{\partial u}{\partial y}\right)_{y=0}$ for the case of collocated actuator/sensor control configuration.

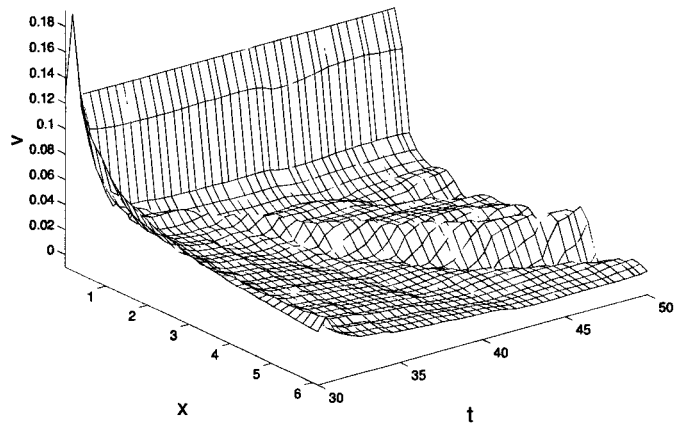

Figure 9.7: Spatio-temporal profile of the wall-normal velocity, $v(x, 0, t)$, for the case of collocated actuator/sensor control configuration.

flow. Note also that, as expected in the case of collocated actuation/sensing (control input at each point depends only on the measurement at the same point), the profile of $v(x,0,t)$ is not uniform along x.

Several alternative control configurations are also tested. Specifically, a control configuration which uses the average of five equally spaced point measurements of $\left(\frac{\partial u}{\partial y}\right)_{y=0}$ on the flat plate to apply spatially uniform control actuation is applied, that is:

$$v(x,0,t) = C(t) = \frac{K}{5}\sum_{i=1}^{5}\left(\frac{\partial u}{\partial y}\right)(x_i,0,t) \tag{9.11}$$

where $K = 0.005$. The above control law can be derived from the general integral feedback control structure presented in the beginning of this section by setting $s(x) = \frac{1}{5}\sum_{i=1}^{5}\delta(x-x_i)$, where $\delta(\cdot)$ is the standard Dirac function. Figure 9.8 shows the spatio-

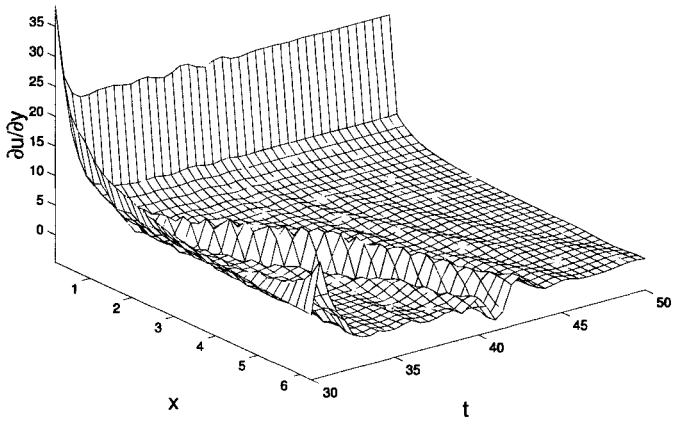

Figure 9.8: Spatio-temporal profile of $\left(\frac{\partial u}{\partial y}\right)_{y=0}$ for the case of spatially uniform control actuation with five equally spaced point measurements.

temporal profile of $\left(\frac{\partial u}{\partial y}\right)_{y=0}$ starting from initial conditions of the steady state open-loop simulation. This control configuration does a very good job in reducing the frictional drag compared to the open-loop operation. Figure 9.9 shows the spatio-

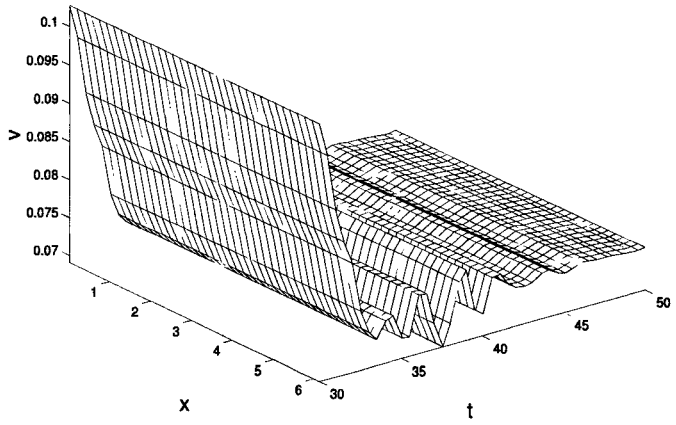

Figure 9.9: Spatio-temporal profile of the wall-normal velocity, $v(x, 0, t)$, for the case of spatially uniform control actuation with five equally spaced point measurements (the first measurement is taken at the leading edge of the plate).

temporal profile of the wall-normal velocity, $v(x, 0, t)$, which is the manipulated input. Clearly the value of $v(x, 0, t)$ is small and positive for all times which means that blowing is applied to the flow. Note also that, as expected in the case of spatially uniform control actuation, the profile of $v(x, 0, t)$ is uniform along x.

Figure 9.10 shows the corresponding velocity profile for the entire domain respectively; the use of blowing on the plate slows down the flow very close to the plate, thereby reducing the frictional drag on the plate and increasing the value of the velocity field close to the edge of the boundary layer compared to the open-loop velocity of Figure 9.3 (see also Figure 9.4). The robustness of the control scheme of Equation 9.11 is tested with respect to a sinusoidal profile of amplitude 0.1 which is superimposed on the calculated average of the five measurements to simulate a time-varying disturbance in the measurements. Figure 9.11 shows the spatio-temporal profile of $\left(\frac{\partial u}{\partial y}\right)_{y=0}$ starting from initial conditions of the steady state open-loop simulation

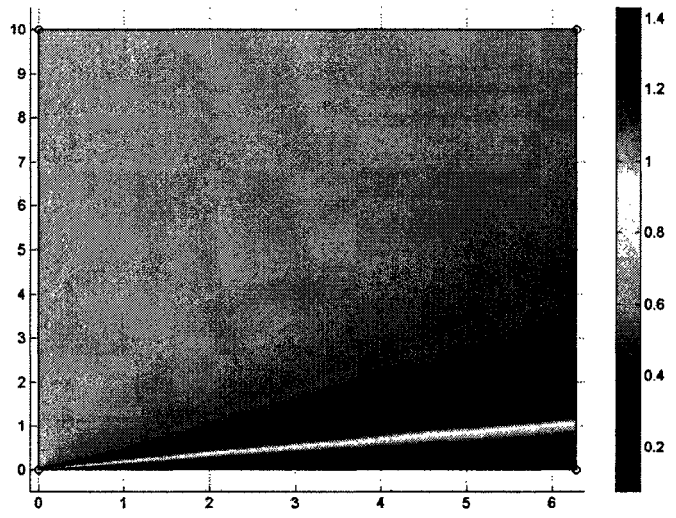

Figure 9.10: Steady state closed-loop velocity profile for flow over flat plate for the entire domain, for the case of spatially uniform control actuation with five equally spaced point measurements.

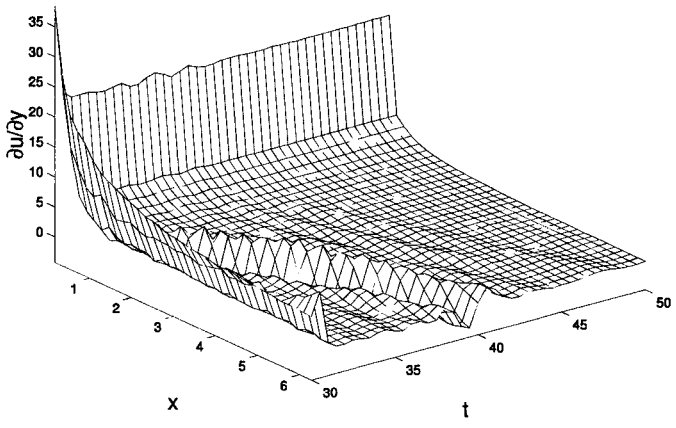

Figure 9.11: Spatio-temporal profile of $\left(\frac{\partial u}{\partial y}\right)_{y=0}$ for the case of spatially uniform control actuation with five equally spaced point measurements; robustness with respect to measurement disturbances.

and Figure 9.12 shows the spatio-temporal profile of $v(x, 0, t)$ for this simulation run.

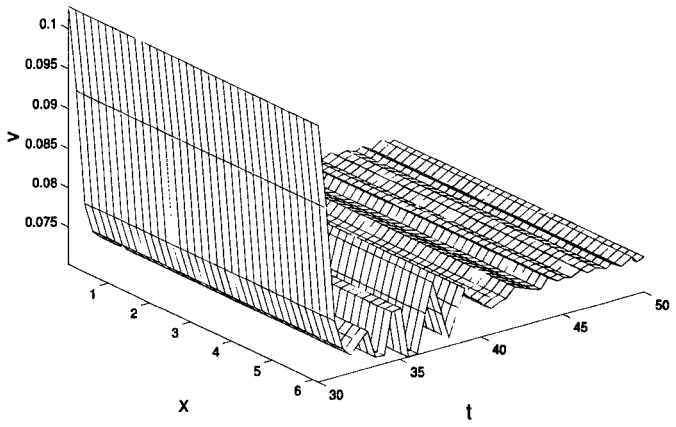

Figure 9.12: Spatio-temporal profile of the wall-normal velocity, $v(x, 0, t)$, for the case of spatially uniform control actuation with five equally spaced point measurements; robustness with respect to measurement disturbances.

While the disturbance influences the flow, the controller is capable of reducing the value of $\left(\frac{\partial u}{\partial y}\right)_{y=0}$ below the open-loop level using blowing. Note also that, because of the persistent nature of the disturbance, the profile of $v(x, 0, t)$ exhibits a slight variation with respect to time for large times (this is not the case in the profile of $v(x, 0, t)$ in the previous simulation run, Figure 9.9, where disturbances have not been included).

Finally, a control configuration which uses the average of many point measurements of $\partial u/\partial y$ on the flat plate to calculate the spatially-uniform control actuation applied to the flow field along the plate is developed and tested; this is done to evaluate the effect of the number and location of measurements on controller performance (amount of control action) and closed-loop performance (frictional drag reduction).

In this case, the control law has the following form:

$$v(x,0,t) = C(t) = \frac{K}{N}\sum_{i=1}^{N}\left(\frac{\partial u}{\partial y}\right)(x_i,0,t) \tag{9.12}$$

where $K = 0.005$ and $N = 350$. The above control law can be also derived from the general integral feedback control structure presented in the beginning of this section by setting $s(x) = \frac{1}{N}\sum_{i=1}^{N}\delta(x - x_i)$.

Figure 9.13 shows the spatio-temporal profile of $\left(\frac{\partial u}{\partial y}\right)_{y=0}$ starting from initial

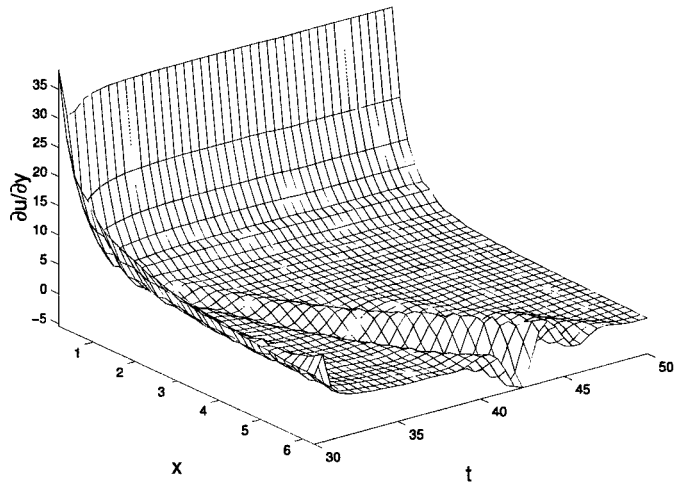

Figure 9.13: Spatio-temporal profile of $\left(\frac{\partial u}{\partial y}\right)_{y=0}$ for the case of spatially uniform control actuation with 350 equally spaced point measurements.

conditions of the steady state open-loop simulation and Figure 9.14 shows the spatio-temporal profile of $v(x,0,t)$ for this simulation run. While this control configuration reduces the frictional drag compared to the open-loop system using blowing, it does not provide a significant improvement (in terms of reduction of the frictional drag) compared to the closed-loop performance achieved with the control configuration of Equation 9.11 which uses only five measurements of $\left(\frac{\partial u}{\partial y}\right)_{y=0}$. However, the advantage of using a large number of measurements can be seen by studying the input profile of Figure 9.14 and comparing it with the input profile of Figure 9.9. Clearly,

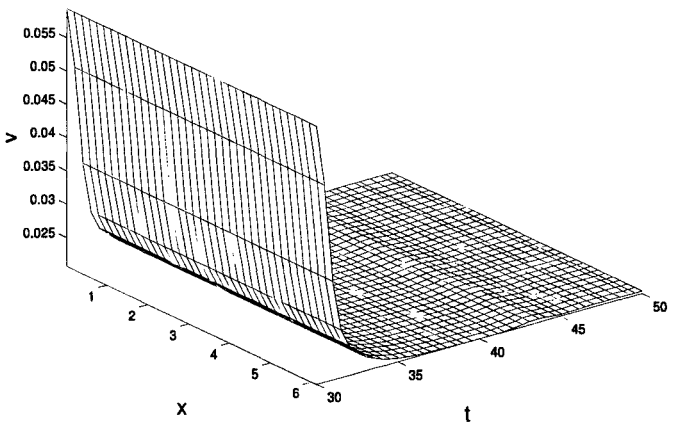

Figure 9.14: Spatio-temporal profile of the wall-normal velocity, $v(x, 0, t)$, for the case of spatially uniform control actuation with 350 equally spaced point measurements.

the use of a large number of measurements taken at spatial locations that are not close to the edge of the plate (where $\left(\frac{\partial u}{\partial y}\right)_{y=0}$ attains its maximum value for both the open- and closed-loop systems) leads to a substantially smaller control action and a smoother control input profile; thereby improving the robustness of the laminar closed-loop flow field with respect to disturbances and transition to turbulence.

9.4 Conclusions

The main conclusion is that the use of active feedback control, which employs reasonable control effort, can significantly reduce the frictional drag exerted on the plate compared to the open-loop values. Furthermore, our results suggest that: a) a small number of measurement sensors may be sufficient to achieve drag reduction, and b) the measurement sensor and control actuator locations can significantly influence flow dynamics and controller performance and should be carefully chosen to avoid using unnecessarily large control action. Further work will be needed to check the

robustness of these results with respect to variations of the Reynolds number and examine the derivation of flow models suitable for model-based controller design and implementation.

Chapter 10

Conclusions

10.1 Conclusions

We have examined the effect of active control on two separate two-dimensional, incompressible viscous flow systems: flow past a circular cylinder and flow past a flat plate. A description of each of the simulations has been provided. The governing equations for both the flow field and the drag measurement have been explained. For each problem, the solution of the flow field for the unactuated system has been given.

Initially, for the circular cylinder, we examined the benchmark case of flow past a cylinder in a small, specified channel and in an essentially unbounded (infinite) fluid. Both the benchmark and infinite cases were validated by other studies for simulations with a stationary cylinder. In the case of the infinite fluid, the stationary cylinder results were validated by both numerical and experimental data in terms of the drag and natural vortex shedding frequency (Strouhal number). A linear relationship was shown between the natural vortex shedding frequency and the Reynolds number.

The effect of oscillatory rotation of the cylinder, as applied in an open-loop control scheme, on the drag has been evaluated for the benchmark and infinite cases.

Amplitude and frequency of rotation were varied. Where available, drag data from the rotating cylinder in the infinite fluid case has been compared to other numerical studies. The phenomena of wake stabilization by rotation and phase lock-on were demonstrated. Open-loop control results have been obtained over a wide range of oscillation parameters.

Several closed-loop strategies were devised for the benchmark cylinder case. Both P and PI controller, using drag measurements and adjusting the amplitude of rotation were investigated. Another active control strategy, that adjusts the frequency of rotation based on measurements of the incoming flow speed, was successfully implemented. This control scheme results in a consistent drag reduction between Reynolds numbers 50 and 500.

Empirical eigenfunctions for the circular cylinder flow system were calculated using the Proper Orthogonal Decomposition (POD) technique. Two different definitions of the POD modes were used: one that used the total velocity and one that incorporated velocity fluctuations (from the mean velocity). Two definitions of the inner product, vector and integral, were used. These POD modes were calculated for two different flow domains (for both POD definitions, both inner product definitions, and both velocity components). After the POD modes were shown, the modal amplitudes of the data set were reconstructed. A control scheme involving the modal amplitude of the first mode of the u component was simulated in an attempt to reduce drag.

A Galerkin Projection of the Navier-Stokes equations was performed using the previously calculated POD modes. The projection was manipulated to yield a model, a set of 10 ordinary differential equations (ODEs) to approximate the infinite dimensional partial differential equations (the Navier-Stokes equations). This reduced-order model was solved and then visualized to compare to the original PDE. It was found

that the model reproduced the PDE satisfactorily around the cylinder itself, including the near-wake region where the first vortex is shed behind the cylinder. In at least one case, the model reproduced the results of the full simulation fairly closely for the whole domain. The effect of the pressure term on the model was discussed. The model was simulated at several Reynolds numbers, and the modal amplitudes scaled as expected. A methodology was discussed to implement forcing through rotational oscillation with this model.

The focus of this study of flow over the circular cylinder was principally to understand the dynamics of this complex system. In modeling the fluid dynamics of this system, it is hoped that insight obtained from the model will aid in the development of effective closed-loop control laws. A good understanding of the stationary cylinder system and the cylinder with open-loop actuation is also a prerequisite for closed-loop control, and this prerequisite has been studied here thoroughly as well. While an effective suggestion for active control of the system and further study of closed-loop control through reduced-order modeling has been given here, much more can be done to further the understanding of the closed-loop dynamics of this system.

Drag reduction of flow past a flat plate was examined. A controller was developed that could reduce drag on the flat plate at Reynolds number 50,000 by blowing/suction actuation. Both open and closed-loop simulations were executed. Several different control configurations were examined. It was found that, with reasonable control effort, the frictional drag past the flat plate could be significantly reduced compared to open-loop (no actuation) cases.

10.2 Future Work

Much of the recent literature on incompressible fluid flows of this type focuses on the computational demands of solving problems at higher Reynolds numbers ([26, 57, 78, 96] as well as many others). Because great computational challenges occur at high Reynolds numbers, relatively few studies have been done on the drag force on these systems with and without actuation. In the case of the circular cylinder, the von Karman vortex street is present at Reynolds numbers much greater than 500 [109], and most applications deal with flows at Reynolds numbers much greater than those studied here. The effects of drag on the cylinder and its subsequent control at high Reynolds numbers is, therefore, a very important area for future study. In the case of the flat plate, the flows studied here are in the laminar regime. Once again, many applications for this system are at higher Reynolds numbers, specifically in the transitional and turbulent regimes. Modeling turbulent flow is significantly more challenging than modeling laminar flow. Specific mathematical turbulence models have been developed to help compute this type of flow. Propoer Orthogonal Decomposition has been applied to the analysis of and identification of coherent structures in turbulent flow [79]. Studies of control of drag on a flat plate due to turbulent flow is also an important area for future investigation.

Because flow over a circular cylinder is such a complex system, studying the open-loop dynamics and using reduced-order models, as has been done here, is a more productive and efficient approach to developing closed-loop control of this system than attempting to derive systematic control directly from the system itself.

Flow past multiple cylinders is an important engineering challenge, occurring in heat exchanger tube banks, chimney stacks, offshore structures, electrical transmission lines, and in other situations. Significant work has been done in the past on flow

past multiple cylinders. Mittal et al. [83] used a stabilized finite element formulation to examine three sets of cylinder arrangements. The cylinders were separated by up to 5.5 diameters. Mittal et al. also measured the forces applied to the downstream cylinder as a result of the upstream cylinder wake at Re = 100 and Re = 1000. Li et al. [73], whose study attempted to emulate fluid dynamic effects in a heat exchanger, also used the finite element method to study the laminar wake behind one and two cylinders at Reynolds number 100. Farrant et al. [41] used a hybrid boundary element / finite element method and the cell boundary element method to study the laminar vortex shedding pattern of multiple cylinders at Re = 100 and Re = 200. They found in-phase and anti-phase shedding modes in their simulations. Itoh et al. [65] studied numerical simulations of three-dimensional flow around two cylinders arranged in-line for the purpose of ensuring the safety of the structures exposed to the flow.

Flow phenomena of multiple cylinders are significantly different than flow past a single circular cylinder. When cylinders are arranged in tandem (or in-line) as shown in the left side of Figure 10.1, the formation of the vortex street varies from that of a

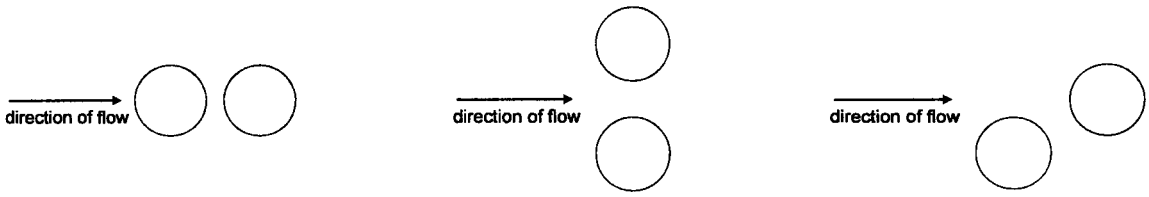

Figure 10.1: Multiple cylinder configurations: Left - Tandem; Center - Transverse; Right - Staggered

transverse (side-by-side, shown in the center of Figure 10.1) arrangement, staggered (right side of Figure 10.1) arrangement, or a single cylinder. Cylinders interfere with each other's vortex formation, shedding, and wake patterns. An arrangement of multiple cylinders drastically effects the coefficient of drag, C_D, when compared to the single cylinder arrangement [83]. Drag measurements made by Mittal et al.

[83] in numerical simulations matched well with experimental results. In a tandem arrangement, vortex shedding occurs for the upstream (or first) cylinder only when the interval between the two cylinders exceeds a certain spacing ($L/D > 3$) [73,83]. The lift and drag coefficients, the vortex shedding frequencies, and the critical Reynolds number found by Li et al. were generally lower than those found in experiments, but this was attributed to the coarse grids used in the calculations [73]. When both cylinders shed vortices, it is found that they generally do so at the same frequency or Strouhal number, although they may vary with respect to phase [41]. Particle streak line simulations were compared to smoke visualization photographs taken in experimental studies [41].

This work leaves open the possibility of applying the same open-loop control strategy studied here to multiple cylinder configurations, as shown in Figure 10.1. These results could be compared to data from stationary multiple cylinder simulations available in the literature and presented here. The active feedback control strategy used in Chapter 5 can also be applied and analyzed for multiple cylinder configurations. Also, a reduced-order model, as shown for the single cylinder case in Chapter 8, can be computed for the multiple cylinder case.

Appendix A

Ancillary Plots

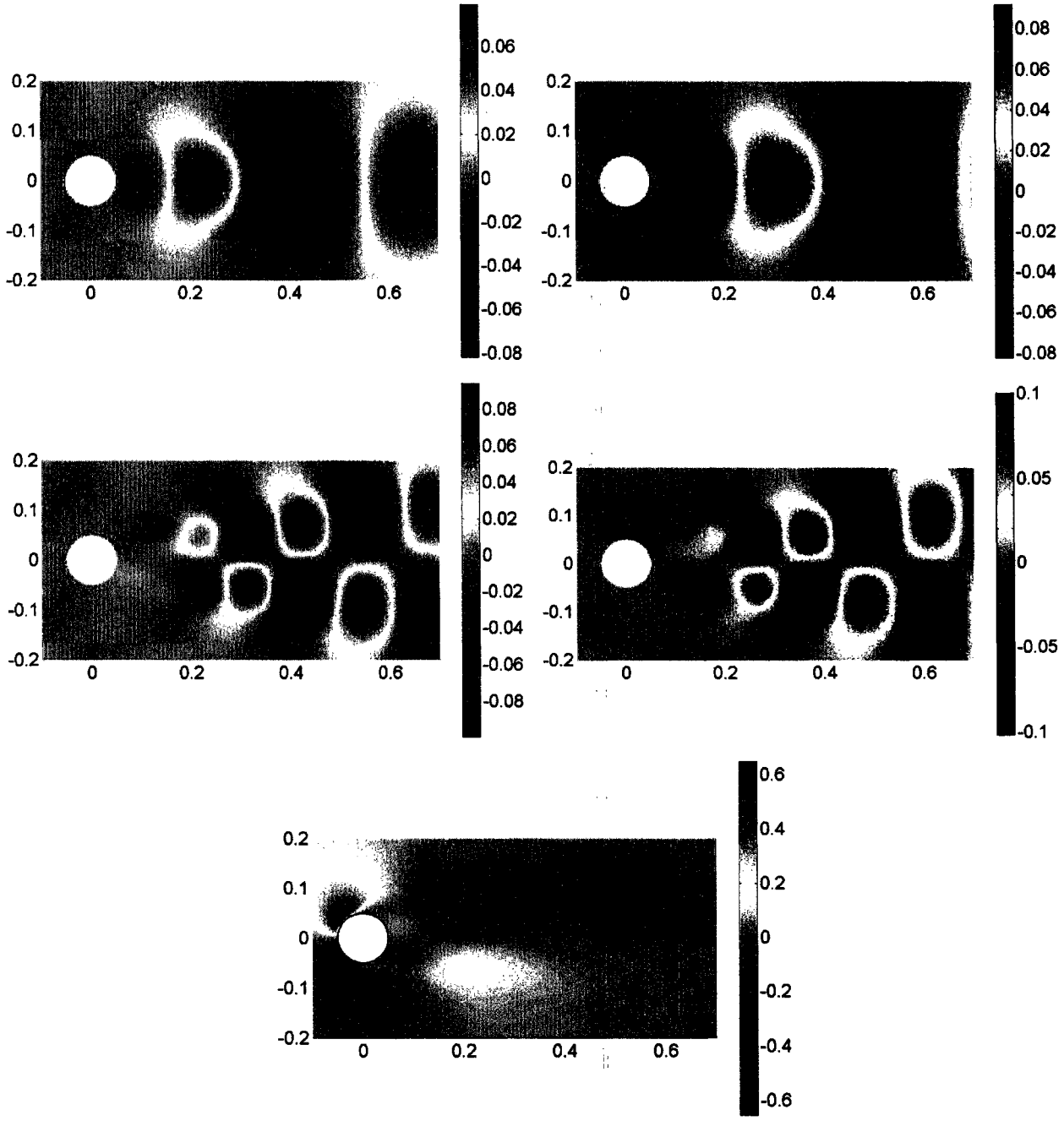

Figure A.1: Ψ, subset of flow field used to calculate POD modes: Top Row - Left: Ψ^1, Right: Ψ^2, Middle Row - Left: Ψ^3, Right: Ψ^4, Bottom Row - Ψ^5.

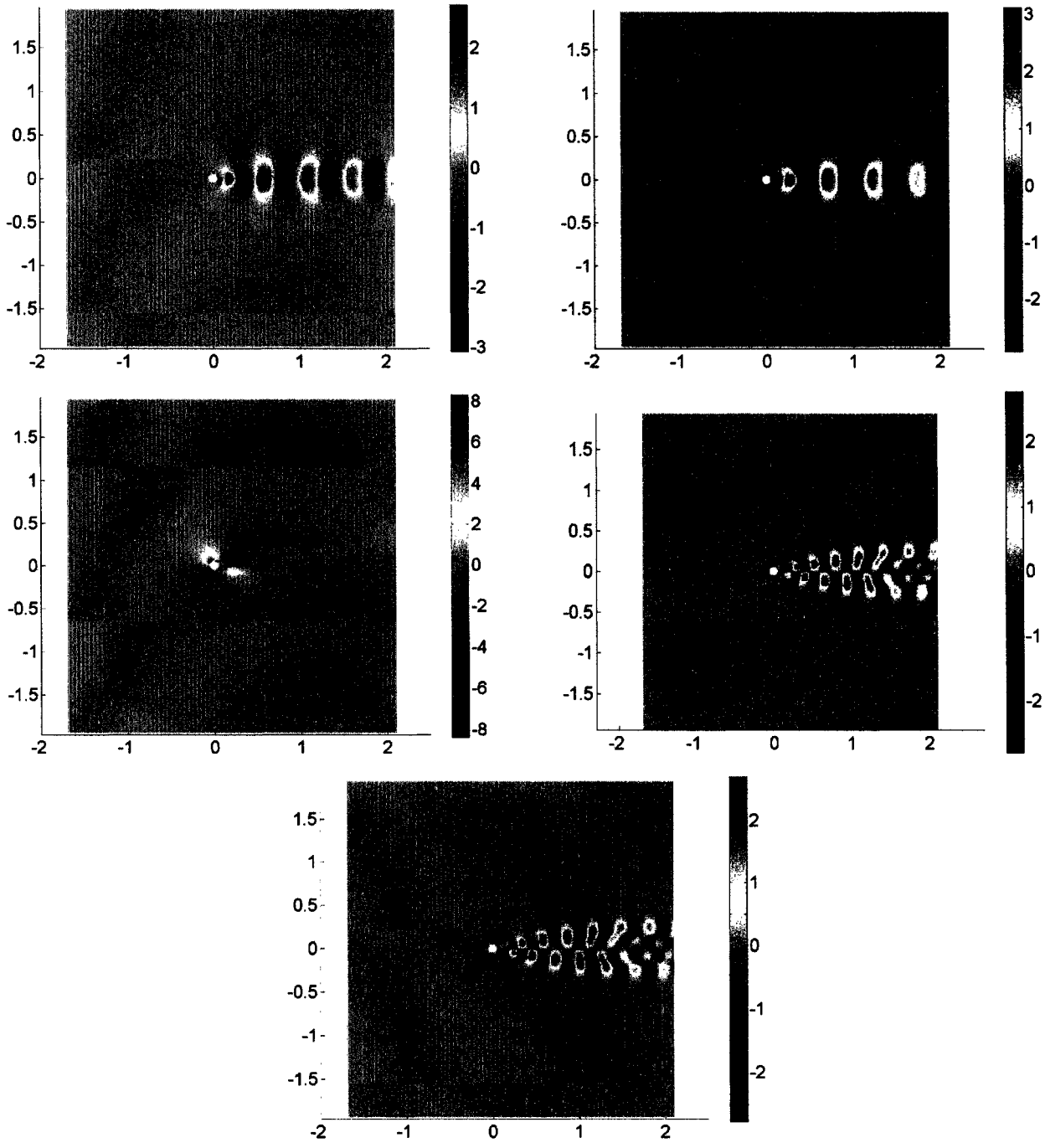

Figure A.2: Ψ, total velocity POD definition: Top Row - Left: Ψ^1, Right: Ψ^2, Middle Row - Left: Ψ^3, Right: Ψ^4, Bottom Row - Ψ^5.

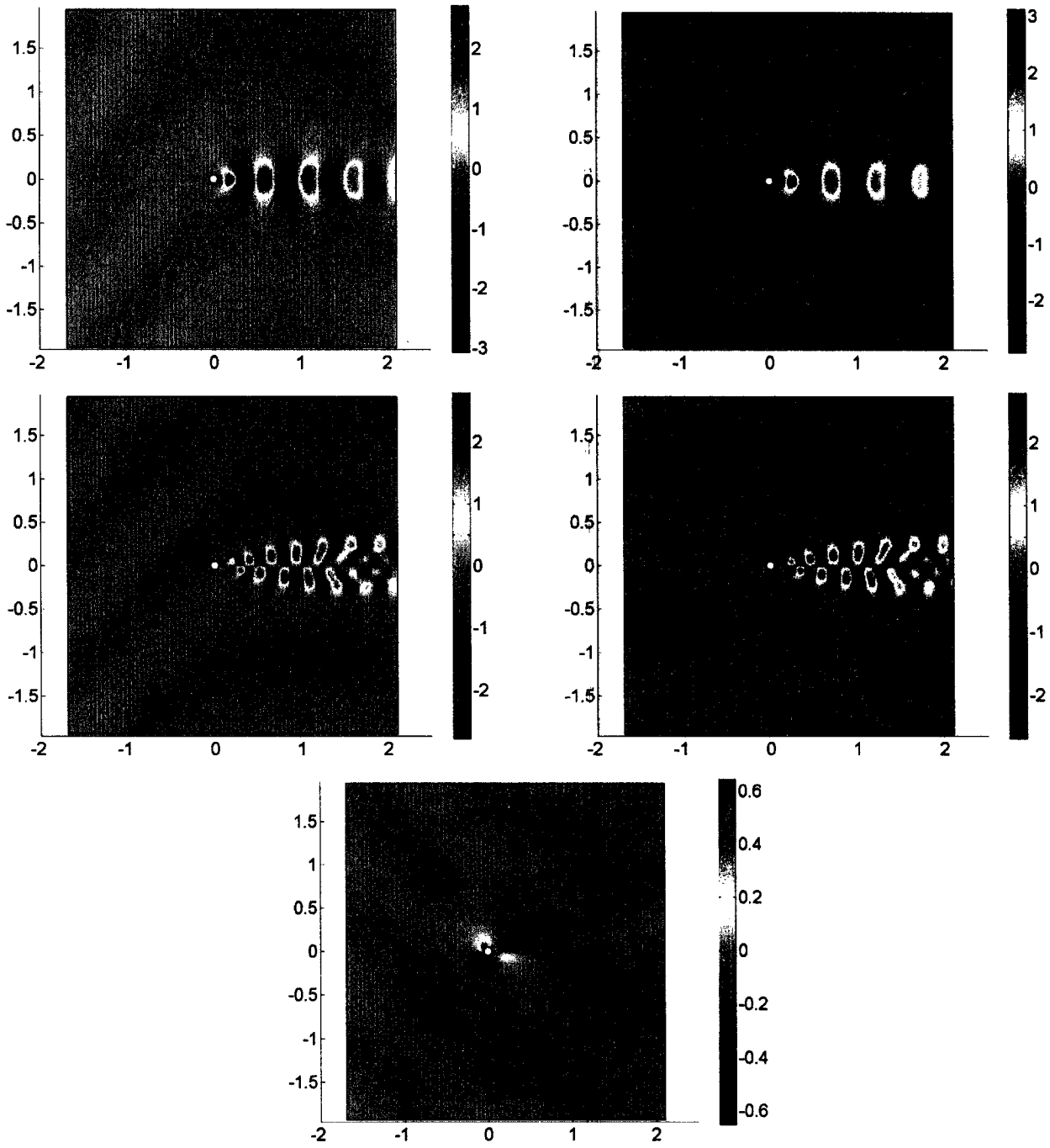

Figure A.3: Ψ, velocity fluctuations POD definition: Top Row - Left: Ψ^1, Right: Ψ^2, Middle Row - Left: Ψ^3, Right: Ψ^4, Bottom Row - Ψ^5

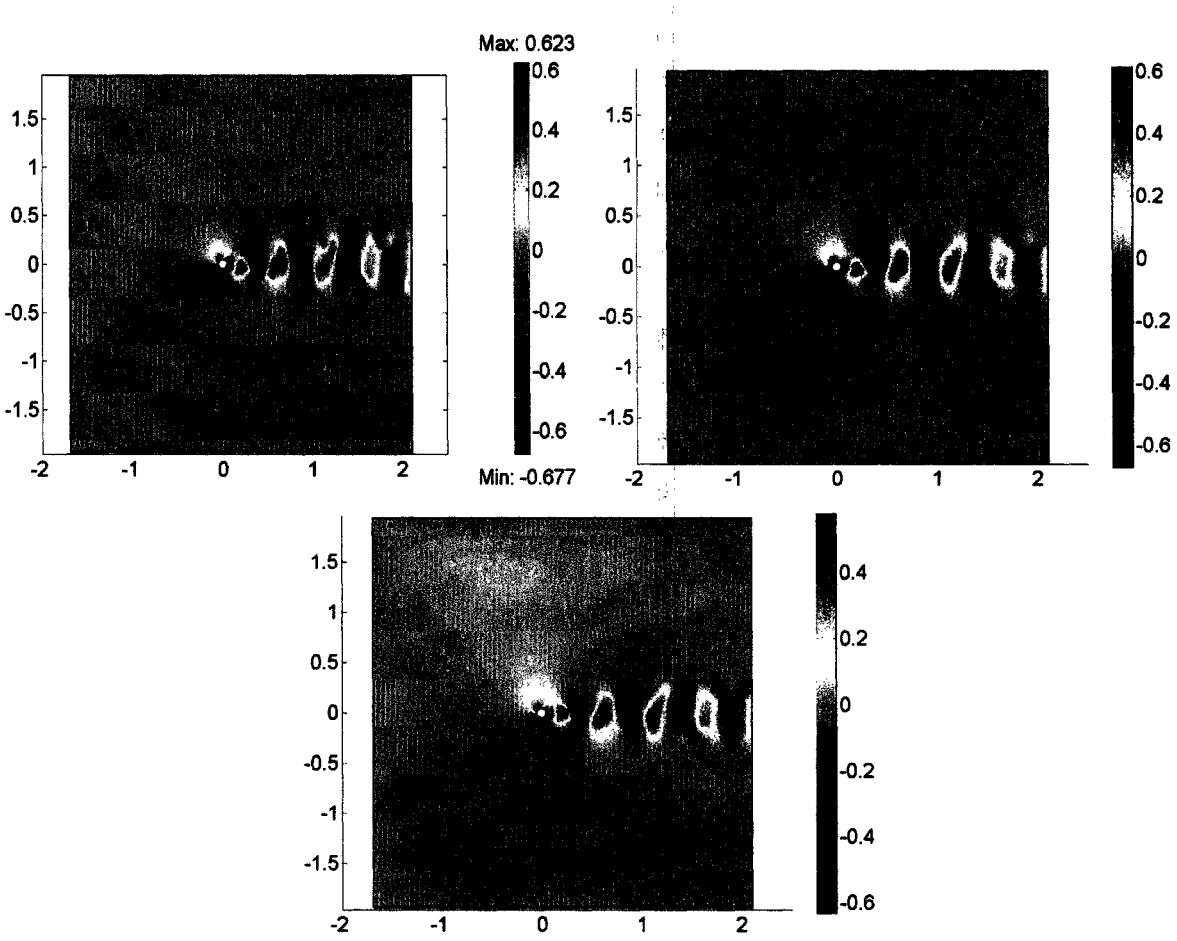

Figure A.4: Comparison between simulation and POD reconstruction after 15 seconds, v surface plots: Top Row, total velocity POD definition - Left: simulation, Right: POD reconstruction, Bottom Row - reconstruction from velocity fluctuations POD definition.

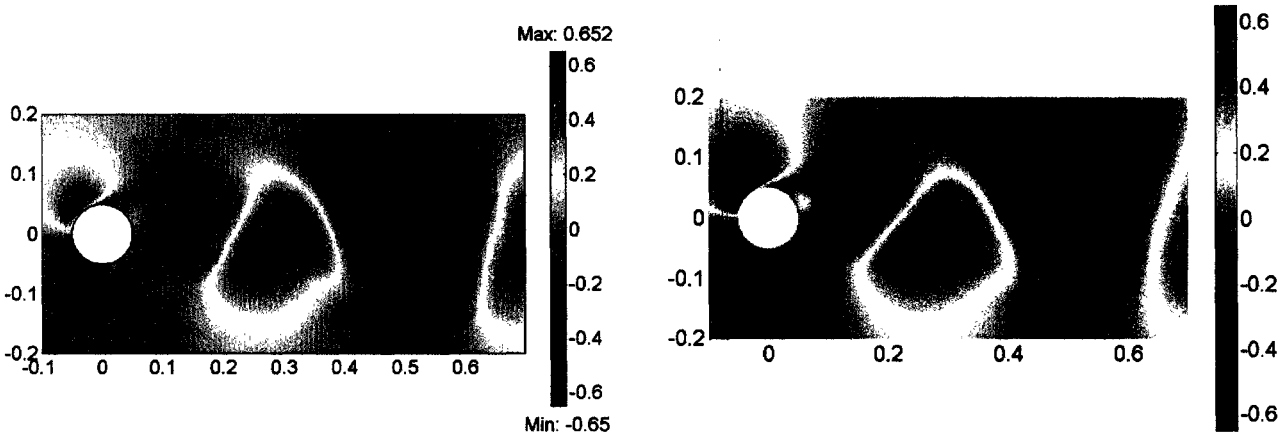

Figure A.5: Comparison between simulation and POD reconstruction after 15 seconds, subset of total flow field used to calculate POD modes, v surface plots - Left: simulation, Right: POD reconstruction.

Bibliography

[1] O. M. Aamo and M. Krstić. *Flow Control by Feedback.* Springer, London, U. K., 2003.

[2] A. Armaou and P. D. Christofides. Feedback control of the Kuramoto-Sivashinsky equation. *Physica D.*, 137:49–61, 2000.

[3] A. Armaou and P. D. Christofides. Wave suppression by nonlinear finite-dimensional control. *Chem. Eng. Sci.*, 55:2627–2640, 2000.

[4] J. Baker, A. Armaou, and P. D. Christofides. Nonlinear control of incompressible fluid flow: Application to Burgers' equation and 2D channel flow. *J. Math. Anal. Appl.*, 252:230–255, 2000.

[5] J. Baker and P. D. Christofides. Drag reduction in transitional channel flow using distributed control. *Int. J. Contr.*, 75:1213–1218, 2002.

[6] J. Baker, J. Myatt, and P. D. Christofides. Drag reduction in flow over a flat plate using active feedback control. *Comp. & Chem. Eng.*, 26:1095–1102, 2002.

[7] P. Bakewell and J. L. Lumley. Viscous sublayer and adjacent wall region in turbulent pipe flow. *Phys. Fluids*, 10:1880–1889, 1967.

[8] A. Balogh, W.-J. Liu, and M. Krstić. Stability enhancement by boundary control in 2D channel flow. *IEEE Trans. Autom. Contr.*, 46:1696–1711, 2001.

[9] B. Bamieh and M. Dahleh. Disturbance energy amplification in three-dimensional channel flows. In *Proceedings of American Control Conference*, pages 4532–4537, San Diego, CA, 1999.

[10] B. Bamieh and M. Dahleh. Energy amplification in channel flows with stochastic excitation. *Phys. Fluids*, 13:3258–3269, 2001.

[11] A. K. Bangia, P. F. Batcho, I. G. Kevrekidis, and G. E. Karniadakis. Unsteady 2-D flows in complex geometries: Comparative bifurcation studies with global eigenfunction expansion. *SIAM J. Sci. Comp.*, 18:775–805, 1997.

[12] G. K. Batchelor. *An Introduction to Fluid Dynamics.* Cambridge University Press, Cambridge, U. K., 1967.

[13] F. J. Bayley. *An Introduction to Fluid Dynamics.* Interscience Publishers, New York, 1958.

[14] S. Beringen. Active control of transition by periodic suction and blowing. *Phys. Fluids*, 27:1345–1348, 1984.

[15] G. Berkooz, P. J. Holmes, and J. L. Lumley. The Proper Orthogonal Decomposition in the analysis of turbulent flows. *Ann. Rev. Fluid Mech.*, 193:445–473, 1993.

[16] T. R. Bewley. Flow control: New challenges for a new renaissance. *Progress in Aerospace Sciences*, 37:21–58, 2001.

[17] R. B. Bird, W. E. Stewart, and E. N. Lightfoot. *Transport Phenomena.* John Wiley and Sons, Inc., New York, 2002.

[18] M. Braza, P. Chassaing, and H. H. Minh. Numerical study and physical analysis of the pressure and velocity fields in the near wake of a circular cylinder. *J. Fluid Mech.*, 165:79–130, 1986.

[19] J. A. Burns and B. B. King. Optimal sensor location for robust control of distributed parameter systems. In *Proceedings of 33rd IEEE Conference on Decision and Control*, pages 3965–3970, Orlando, FL, 1994.

[20] J. A. Burns, B. B. King, and D. Rubio. Feedback control of a thermal fluid using state estimation. *Int. J. Comput. Fluid D.*, 11:93–112, 1998.

[21] J. A. Burns and Y. R. Ou. Feedback control of the driven cavity problem using LQR designs. In *Proceedings of 33rd IEEE Conference on Decision and Control*, pages 289–294, Orlando, FL, 1994.

[22] D. M. Bushnell and C. B. McGinley. Turbulence control in wall flows. *Ann. Rev. Fluid Mech.*, 21:1–20, 1989.

[23] B. J. Cantwell. Organized motion in turbulent flow. *Ann. Rev. Fluid Mech.*, 13:457–515, 1981.

[24] E. Caraballo, M. Samimy, and J. DeBonis. Low dimensional modeling of flow for closed-loop flow control. *AIAA paper*, 2003-0059, 2003.

[25] H. A. Carlson and J. L. Lumley. Active control in the turbulent wall layer of a minimal flow unit. *J. Fluid Mech.*, 329:341–371, 1996.

[26] M. Cheng, Y. T. Chew, and S. C. Luo. Numerical investigation of a rotationally oscillating cylinder in mean flow. *J. Fluids and Struct.*, 15:981–1007, 2001.

[27] H. Choi, P. Moin, and J. Kim. Active turbulence control for drag reduction in wall-bounded flows. *J. Fluid Mech.*, 262:75–110, 1994.

[28] H. Choi, R. Temam, P. Moin, and J. Kim. Feedback control for unsteady flow and its application to the stochastic burger's equation. *J. Fluid Mech.*, 253:509–543, 1993.

[29] P. D. Christofides. *Nonlinear and Robust Control of PDE Systems: Methods and Applications to Transport-Reaction Processes.* Birkhäuser, Boston, 2001.

[30] P. D. Christofides and A. Armaou. Global stabilization of the Kuramoto-Sivashinsky equation via distributed output feedback control. *Syst. & Contr. Lett.*, 39:283–294, 2000.

[31] P. D. Christofides and P. Daoutidis. Finite-dimensional control of parabolic PDE systems using approximate inertial manifolds. *J. Math. Anal. Appl.*, 216:398–420, 1997.

[32] D. C. Chu and G. E. Karniadakis. A direct numerical simulation of laminar and turbulent flow over riblet-mounted surfaces. *J. Fluid Mech.*, 250:1–42, 1993.

[33] K. Cohen, S. Siegel, and T. McLaughlin. Sensor placement based on Proper Orthogonal Decomposition modeling of a cylinder wake. *AIAA paper*, 2003-4259, 2003.

[34] L. Cortelezzi, K. H. Lee, J. Kim, and J. L. Speyer. Skin-friction drag reduction via reduced-order linear feedback control. *Int. J. Comp. Fluid Dynam.*, 11:79–92, 1998.

[35] L. Cortelezzi and J. L. Speyer. Robust reduced-order controller of laminar boundary layer transition. *Rhys. Rev. E.*, 58:1906–1910, 1998.

[36] C. H. Crawford and G. E. Karniadakis. Reynolds stress analysis of EMHD-controlled wall turbulence. part I. streamwise forcing. *Phys. Fluids*, 9:788–806, 1997.

[37] D. D'Alessandro, M. Dahleh, and I. Mezic. Control of mixing in fluid flow: A maximum entropy approach. *IEEE Trans. Automat. Contr.*, 44:1852–1863, 1999.

[38] R. D'Andrea, R. L. Behnken, and R. M. Murray. Rotating stall control of an axial flow compressor using pulsed air injection. *J. Turbomachinery*, 119:742–752, 1997.

[39] A. E. Deane, I. G. Kevrekidis, G. E. Karniadakis, and S. A. Orszag. Low-dimensional models for complex geometry flows: Application to grooved channels and circular cylinders. *Phys. Fluids A*, 3:2337–2354, 1991.

[40] M. Desai and K. Ito. Optimal controls of Navier-Stokes equations. *SIAM J. Contr. & Optim.*, 32:1428–1446, 1994.

[41] T. Farrant, M. Tan, and W. G. Price. A cell boundary element method applied to laminar vortex shedding from circular cylinders. *Computers and Fluids*, 30:211 – 236, 2001.

[42] C. Foias, M. S. Jolly, I. G. Kevrekidis, G. R. Sell, and E. S. Titi. On the computation of inertial manifolds. *Phys. Lett. A*, 131:433–437, 1989.

[43] C. Foias, O. Manley, R. Rosa, and R. Temam. *Navier-Stokes Equations and Turbulence.* Cambridge University Press, Cambridge, 2001.

[44] C. Foias, G. R. Sell, and E. S. Titi. Exponential tracking and approximation of inertial manifolds for dissipative equations. *J. Dynamics and Differential Equations*, 1:199–244, 1989.

[45] C. Foias and R. Témam. Algebraic approximation of attractors: The finite dimensional case. *Physica D*, 32:163–182, 1988.

[46] N. Fujisawa, K. Ikemoto, and K. Nagaya. Vortex shedding resonance from a rotationally oscillating cylinder. *J. Fluids and Struct.*, 12:1041–1053, 1998.

[47] K. Fukunaga. *Introduction to statistical pattern recognition.* Academic Press, New York, 1990.

[48] M. Gad-el-Hak. Flow control. *Appl. Mech. Rev.*, 42:261–293, 1989.

[49] M. Gad-el-Hak. Interactive control of turbulent boundary layers: A futuristic overview. *AIAA J.*, 32:1753–1765, 1994.

[50] M. Gad-el-Hak and D. M. Bushnell. Separation control. *J. Fluids Eng.*, 113:5–30, 1991.

[51] E. A. Gillies. *Low-Dimensional Characterization and Control of Non-Linear Wake Flows.* University of Glasgow - Doctoral Dissertation, Glasgow, Scotland, 1995.

[52] E. A. Gillies. Low-dimensional control of the circular cylinder wake. *J. Fluid Mech.*, 371:157–158, 1998.

[53] E. A. Gillies. Multiple sensor control of vortex shedding. *AIAA J.*, 39:748–750, 2001.

[54] M. D. Graham and I. G. Kevrekidis. Alternative approaches to the Karhunen-Loève decomposition for model reduction and data analysis. *Comp. & Chem. Eng.*, 20:495–506, 1996.

[55] W. R. Graham, J. Peraire, and K. Y. Tang. Optimal control of vortex shedding using low order models - Part I: Open-loop model development. *Int. J. for Num. Methods in Eng.*, 44(7):973–990, 1999.

[56] J. Guckenheimer. Strange attractors in fluids: Another view. *Ann. Rev. Fluid Mech.*, 18:15–32, 1986.

[57] J. W. He, R. Glowinski, R. Metcalfe, A. Nordlander, and J. Periaux. Active control and drag optimization for flow past a circular cylinder: I. oscillatory cylinder rotation. *J. Comp. Phys.*, 163:83–117, 2000.

[58] R. D. Henderson. Nonlinear dynamics and patterns in turbulent wake transition. *J. Fluid Mech.*, 352:65–112, 1997.

[59] P. J. Holmes, J. L. Lumley, and G. Berkooz. *Turbulence, Coherent Structures, Dynamical Systems, and Symmetry.* Cambridge University Press, Cambridge, U. K., 1996.

[60] P. J. Holmes, J. L. Lumley, G. Berkooz, J. C. Mattingly, and R. W. Wittenberg. Low-dimensional models of coherent structures in turbulence. *Phys. Reports*, 287:337–384, 1997.

[61] L. S. Hou and Y. Yan. Dynamics for controlled Navier-Stokes systems with distributed controls. *SIAM J. Contr. & Optim.*, 35:654–677, 1997.

[62] COMSOL Incorporated. *FEMLAB: Model Library.* COMSOL, Stockholm, Sweden, 2001.

[63] K. Ito and S. S. Ravindran. A reduced order method for control of fluid flows. In *Proceedings of 35th IEEE Conference on Decision and Control*, pages 3705–3710, Kobe, Japan, 1996.

[64] K. Ito and S. S. Ravindran. Reduced order methods for nonlinear infinite dimensional control systems. In *Proceedings of 36th IEEE Conference on Decision and Control*, pages 2213–2218, San Diego, California, 1997.

[65] Y. Itoh and R. Himeno. Numerical simulation of three-dimensional flow around two cylinders in tandem arrangement. *RIKEN Review*, 48:1 = 4, 2002.

[66] S. S. Joshi, J. L. Speyer, and J. Kim. Modeling and control of two dimensional poiseuille flow. In *Proceedings of 34th IEEE Conference on Decision and Control*, pages 921–927, New Orleans, LA, 1995.

[67] S. S. Joshi, J. L. Speyer, and J. Kim. A system theory approach to the feedback stabilization of infinitesimal and finite-amplitude disturbances in plane poiseuille flows. *J. Fluid Mech.*, 332:157–184, 1997.

[68] S. S. Joshi, J. L. Speyer, and J. Kim. Finite dimensional optimal control of poiseuille flow. *J. Guid. Control Dynam.*, 22:340–348, 1999.

[69] H. Juárez, R. Scott, R. Metcalfe, and B. Bagheri. Direct simulation of freely rotating cylinders in viscous flows by high-order finite element methods. *Computers and Fluids*, 29:547–582, 2000.

[70] S. Kang and K. Ito. A feedback control law for systems arising in fluid dynamics. In *Proceedings of 30th IEEE Conference on Decision and Control*, pages 384–385, Tampe, AZ, 1992.

[71] B. B. King and Y. Qu. Nonlinear dynamic compensator design for flow control in a driven cavity. In *Proceedings of 34th IEEE Conference on Decision and Control*, pages 3741–3746, New Orleans, LA, 1995.

[72] K. H. Lee, L. Cortelezzi, J. Kim, and J. L. Speyer. Application of reduced-order controller to turbulent flows for drag reduction. *Phys. Fluids*, 13:1321–1330, 2001.

[73] J. Li, A. Chambarel, M. Donneaud, and R. Martin. Numerical study of laminar flow past one and two circular cylinders. *Computers and Fluids*, 19:155–170, 1991.

[74] L. Li, S. J. Sherwin, and P. W. Bearman. A moving frame of reference algorithm for fluid/structure interaction of rotating and translating bodies. *Int. J. Numer. Meth. Fluids*, 38:187–206, 2002.

[75] Y. C. Liang, H. P. Lee, S. P. Lim, W. Z. Lin, and K. H. Lee. Proper Orthogonal Decomposition and its applications - Part I: Theory. *J. of Sound and Vib.*, 252(3):527–544, 2002.

[76] W. J. Liu and M. Krstić. Stability enhancement by boundary control in the Kuramoto-Sivashinsky equation. *Nonlinear Analysis - Theory, Methods & Applications*, 43:485–507, 2001.

[77] W. J. Liu and M. Krstić. Global boundary stabilization of the Korteweg-de Vries-Burgers equation. *Computational and Applied Mathematics*, 21:315–354, 2002.

[78] X. Y. Lu and J. Sato. A numerical study of flow past a rotationally oscillating circular cylinder. *J. Fluids and Struct.*, 10:829–849, 1996.

[79] J. L. Lumley. The structure of inhomogeneous turbulent flows. *Atm. Turb. and Radio Wave Prop.*, pages 166–178, 1967.

[80] J. L. Lumley. Drag reduction in turbulent flow by polymer additives. *J. Polymer Sci. D: Macromol. Rev.*, 7:263–290, 1973.

[81] J. L. Lumley. Coherent structures in turbulence. In *Transition and Turbulence*, pages 215–242, Academic Press, New York, 1981.

[82] I. Mezic and S. Narayanan. Overview of some theoretical and experimental results on modeling and control of shear flows. In *Proceedings of 39th IEEE Conference on Decision and Control*, pages 1709–1715, Piscataway, NJ, 2000.

[83] S. Mittal, V. Kumar, and A. Raghuvanshi. Unsteady incompressible flows past two cylinders in tandem and staggered arrangements. *Int. J. Numer. Meth. Fluids*, 25:1315 – 1344, 1997.

[84] A. C. Or, L. Cortelezzi, and J. L. Speyer. Robust feedback control of rayleigh-benard convection. *J. Fluid Mech.*, 437:175–202, 2001.

[85] A. C. Or, R. E. Kelley, L. Cortelezzi, and J. L. Speyer. Control of long-wavelength marangoni-benard convection. *J. Fluid Mech.*, 387:321–341, 1999.

[86] T. C. Papanastasiou, N. Malamataris, and K. Ellwood. A new outflow boundary condition. *Int. J. Numer. Meth. Fluids*, 14:587–608, 1992.

[87] D. S. Park, D. M. Ladd, and E. W. Hendricks. Feedback control of a global mode in spatially developing flows. *Phys. Lett. A*, 182:244–248, 1993.

[88] F. R. Payne and J. L. Lumley. Large eddy structure of the turbulent wake behind a circular cylinder. *Phys. Fluids*, 10:194–196, 1967.

[89] B. Protas and J. E. Wesfreid. Drag force in the open - loop control of the cylinder wake in the laminar regime. *Phys. Fluids*, 14:810–826, 2002.

[90] M. Rajaee, S. K. F. Karlsson, and L. Sirovich. Low-dimensional description of free shear flow coherent structures and their dynamical behavior. *J. Fluid Mech.*, 258:1–20, 1994.

[91] P. Ray. *A Study of Drag Force on a Rotationally Oscillating Cylinder.* Master's Thesis, University of California, Los Angeles, 2003.

[92] M. Renardy. Imposing 'no' boundary condition at outflow: Why does it work? *Int. J. Numer. Meth. Fluids*, 24:413–417, 1997.

[93] K. Roussopoulos. Feedback control of vortex shedding at low reynolds numbers. *J. Fluid Mech.*, 248:267–296, 1993.

[94] C. W. Rowley, T. Colonius, and R. M. Murray. Model reduction for compressible flows using POD and Galerkin projection. *Physica D.*, 189:115–129, 2004.

[95] M. Schäfer and S. Turek. Benchmark computations of laminar flow around a cylinder. *Notes on Numerical Fluid Mechanics: Flow Simulation with High Performance Computers II*, 52:547–566, 1996.

[96] D. Shiels and A. Leonard. Investigation of a drag reduction on a circular cylinder in rotationally oscillation. *J. Fluid Mech.*, 431:297–322, 2001.

[97] S. Y. Shvartsman and I. G. Kevrekidis. Nonlinear model reduction for control of distributed parameter systems: A computer assisted study. *AIChE J.*, 44:1579–1595, 1998.

[98] S. Siegel, K. Cohen, and T. McLaughlin. Feedback control of a circular cylinder wake in experiment and simulation (invited). *AIAA paper*, 2003-3569, 2003.

[99] S. N. Singh, J. H. Myatt, G. A. Addington, S. Banda, and J. K. Hall. Optimal feedback control of vortex shedding using proper orthogonal decomposition models. *J. Fluids Eng. – Trans. ASME*, 123:612–618, 2001.

[100] L. Sirovich. Turbulence and the dynamics of coherent structures: Part I: Coherent structures. *Quart. Appl. Math.*, XLV:561–571, 1987.

[101] L. Sirovich. Turbulence and the dynamics of coherent structures: Part II: Symmetries and transformations. *Quart. Appl. Math.*, XLV:573–582, 1987.

[102] L. Sirovich. Turbulence and the dynamics of coherent structures: Part III: Dynamics and scaling. *Quart. Appl. Math.*, XLV:583–590, 1987.

[103] T. Smith and D. Boning. Artificial neural network exponentially weighted moving average control for semiconductor processes. *J. Vac. Sci. Tech. A*, 15:1377–1384, 1997.

[104] K. Srinivas. Computation of active control of flow past a circular cylinder. In *Proceedings of the 1st International Conference on Computational Fluid Dynamics*, pages 607–612, Kyoto, Japan, 2000.

[105] S. Taneda. Visual study of separated flows around bodies. *Prog. Aerospace Sci.*, 17:287–348, 1977.

[106] J. Taylor and M. N. Glauser. Towards practical flow sensing and control via POD and LSE based low-dimensional tools. *Proceedings of the FEDSM'02: 2002 ASME Fluids Engineering Division Summer Meeting*, FEDSM2002-31416, 2002.

[107] R. Temam. *Infinite-Dimensional Dynamical Systems in Mechanics and Physics.* Springer-Verlag, New York, 1988.

[108] E. S. Titi. On approximate inertial manifolds to the Navier-Stokes equations. *J. Math. Anal. Appl.*, 149:540–557, 1990.

[109] D. T. Tokumaru and P. E. Dimotakis. Rotary oscillation control of a cylinder wake. *J. Fluid Mech.*, 224:77–90, 1991.

[110] P. S. Virk. Drag reduction fundamentals. *AIChE J.*, 21:625–656, 1975.

[111] M. J. Walsh. Drag characteristics of v-groove and transverse curvature riblets. In Viscous Flow Drag Reduction (edited by G. R. Hough). *AIAA J.*, pages 168–184, 1980.

[112] S. Whitaker. *Introduction to Fluid Mechanics.* Prentice-Hall, Inc., New Jersey, 1968.

[113] C. H. K. Williamson. Defining a universal and continuous Strouhal-Reynolds number relationship for the laminar vortex shedding of a circular cylinder. *Phys. Fluids*, 31:2742–2744, 1988.

[114] C. H. K. Williamson. Vortex dynamics in the cylinder wake. *Ann. Rev. Fluid Mech.*, 28:477–539, 1996.